

Crimp-Imbalanced Protective (CRIMP) Fabrics

Paul V. Cavallaro
NUWC Division Newport

Ali M. Sadegh
The City College of New York



**Naval Undersea Warfare Center Division
Newport, Rhode Island**

PREFACE

This report was funded under NUWC Division Newport Assignment Number TD0207, principal investigator Paul V. Cavallaro (Code 70T). The research was sponsored by the Army Research Laboratory's Weapons & Materials Directorate (ARL-WMD), Aberdeen Proving Grounds, MD, through Military Interagency Purchase Request Number 8HDAVBW332. The sponsoring officer was Bryan A. Cheeseman.

The authors gratefully acknowledge Bryan A. Cheeseman and Robert B. Dooley of ARL-WMD for their support and guidance in ballistic impact behaviors. Special thanks are given to Charles Howland of Warwick Mills, New Ipswich, NH, for sharing his technical expertise in yarn materials, ballistic fabric constructions, and textile manufacturing.

The technical reviewer was Andrew J. Hull (Code 8212).

Reviewed and Approved: 31 March 2010

Harriet L. Coleman

**Harriet L. Coleman
Head, Ranges, Engineering, and Analysis Department**



REPORT DOCUMENTATION PAGE				Form Approved OMB No. 0704-0188	
The public reporting burden for this collection of information is estimated to average 1 hour per response, including the time for reviewing instructions, searching existing data sources, gathering and maintaining the data needed, and completing and reviewing the collection of information. Send comments regarding this burden estimate or any other aspect of this collection of information, including suggestions for reducing this burden, to Department of Defense, Washington Headquarters Services, Directorate for Information Operations and Reports (0704-0188), 1215 Jefferson Davis Highway, Suite 1204, Arlington, VA 22202-4302. Respondents should be aware that notwithstanding any other provision of law, no person shall be subject to any penalty for failing to comply with a collection of information if it does not display a currently valid OPM control number. PLEASE DO NOT RETURN YOUR FORM TO THE ABOVE ADDRESS.					
1. REPORT DATE (DD-MM-YY) 31-03-2010		2. REPORT TYPE Technical Report		3. DATES COVERED (From - To)	
4. TITLE AND SUBTITLE Crimp-Imbalanced Protective (CRIMP) Fabrics				5a. CONTRACT NUMBER MIPR 8HDAVBW332	
				5b. GRANT NUMBER	
				5c. PROGRAM ELEMENT NUMBER	
6. AUTHOR(S) Paul V. Cavallaro Ali M. Sadegh				5.d PROJECT NUMBER	
				5e. TASK NUMBER	
				5f. WORK UNIT NUMBER	
7. PERFORMING ORGANIZATION NAME(S) AND ADDRESS(ES) Naval Undersea Warfare Center Division 1176 Howell Street Newport, RI 02841-1708				8. PERFORMING ORGANIZATION REPORT NUMBER TR 11, 957	
9. SPONSORING/MONITORING AGENCY NAME(S) AND ADDRESS(ES) Army Research Laboratory's Weapons & Materials Directorate Aberdeen Proving Grounds, MD 21005-5069				10. SPONSORING/MONITOR'S ACRONYM ARLWMD	
				11. SPONSORING/MONITORING REPORT NUMBER	
12. DISTRIBUTION/AVAILABILITY STATEMENT Approved for public release; distribution is unlimited.					
13. SUPPLEMENTARY NOTES					
14. ABSTRACT This report documents the research that was conducted to explore the unique concept of using crimp imbalance, which is a simple architectural modification achieved during the weaving process, as a potential mechanism to enhance fragmentation and ballistic protection levels of single-ply woven fabrics. It is shown in this report that crimp imbalance (1) can substantially influence the energy-absorption levels of single-ply fabrics for select fragment simulating projectile velocities, friction coefficients, and impact angles; (2) can be tailored to controllably delay stress-wave propagations among yarn directions; and (3) can minimize reflections at the yarn crossover regions. This research, through single-ply numerical models, demonstrated that deviations in crimp contents can have significant effects on energy absorptions and projectile residual velocities; in short, optimal levels of crimp imbalance may exist for a specific ballistic threat type.					
15. SUBJECT TERMS <div style="display: flex; justify-content: space-between; font-size: small;"> Armor Crimp Ballistic Impact Textiles Woven Fabrics Explicit Methods Finite Element Analysis Energy Absorption Fragment Protection </div>					
16. SECURITY CLASSIFICATION OF:			17. LIMITATION OF ABSTRACT SAR	18. NUMBER OF PAGES 86	19a. NAME OF RESPONSIBLE PERSON Paul V. Cavallaro
a. REPORT Unclassified	b. ABSTRACT Unclassified	c. THIS PAGE Unclassified			19b. TELEPHONE NUMBER (Include area code) 401-832-5082

TABLE OF CONTENTS

	Page
LIST OF ILLUSTRATIONS.....	ii
LIST OF TABLES.....	iv
LIST OF ABBREVIATIONS, ACRONYMS, AND SYMBOLS	iv
INTRODUCTION	1
THREAT TYPES AND PROTECTION LEVELS	2
HISTORICAL DEVELOPMENTS IN BODY ARMOR MATERIALS AND BALLISTIC PERFORMANCE LEVELS	3
COMPARISON OF WAVE PROPAGATIONS IN WOVEN AND UD FABRIC ARMORS.....	8
CURRENT RESEARCH AND APPROACH.....	13
SINGLE-PLY MODEL	14
Normal Impact Results	19
Stress-Wave Results.....	31
Primary Yarn Migration, Slip Velocity, and Mobility.....	33
45°/45° Oblique Impact Results	36
CONCLUSIONS.....	47
REFERENCES	50
APPENDIX A – YARN TENSIONS FOR NORMAL IMPACTS.....	A-1
APPENDIX B – TIME-HISTORY PLOTS OF FSP AND FABRIC ENERGIES FOR NORMAL IMPACTS	B-1
APPENDIX C – YARN FAILURE PLOTS FOR OBLIQUE IMPACTS.....	C-1
APPENDIX D – TIME-HISTORY PLOTS OF FABRIC ENERGIES FOR OBLIQUE IMPACTS	D-1

LIST OF ILLUSTRATIONS

Figure	Page
1 Effects of Crimp on the Transverse Waves	9
2 Transverse Wave Time-Histories at Crossover Regions	11
3 Energy Time-History Results as Functions of δ	12
4 Views of Crimped Fabric Model Cases	16
5 Areal Weight Densities for Model Cases.....	16
6 FSP Degrees of Freedom	17
7 FSP Center Projection on Woven Fabric Target Subject to Normal Impact	18
8 FSP Orientation for 45°/45° Oblique Impact.....	19
9 Impact Deformations As Functions of FSP Initial Velocity: Iso-Crimp Case.....	20
10 Impact Deformations As Functions of FSP Initial Velocity: Crimp Case C	21
11 Impact Deformations As Functions of FSP Initial Velocity: Crimp Case B	22
12 Impact Deformations As Functions of FSP Initial Velocity: Crimp Case A.....	23
13 Residual Velocities for Fully Perforated Normal Impacts, $\mu = 0.1$	24
14 Residual Velocities for Fully Perforated Normal Impacts, $\mu = 0.5$	24
15 Percentage of FSP Kinetic Energy Absorbed by Fabric for Fully Perforated Normal Impacts, $\mu = 0.1$	24
16 Percentage of FSP Kinetic Energy Absorbed by Fabric for Fully Perforated Normal Impacts, $\mu = 0.5$	25
17 E_{rf} As Percentage of FSP Kinetic Energy for Non-Fully Perforated Normal Impacts, $\mu = 0.1$	25
18 E_{rf} As Percentage of FSP Kinetic Energy for Non-Fully Perforated Normal Impacts, $\mu = 0.5$	25
19 Ballistic Limit Curves for Normal Impacts, $\mu = 0.1$	27
20 Ballistic Limit Curves for Normal Impacts, $\mu = 0.5$	27
21 Percentage of FSP Initial Kinetic Energy Absorbed by Fabric for Normal Impacts, $\mu = 0.1$	28
22 Percentage of FSP Initial Kinetic Energy Absorbed by Fabric for Normal Impacts, $\mu = 0.5$	28
23 Von Mises Stress Plots Shown at Stress-Wave Arrival Times Along HCC Yarn Boundaries ($V_o = 1200$ ft/sec).....	32
24 Primary Yarn Displacement Contours Shown for Normal Impacts with $V_o = 1200$ ft/sec at $10 \mu\text{sec}$	33
25 Relative Slip Velocity Computations of Primary Yarns.....	34
26 Time-History Plots: X- and Y-Velocity Components for Primary Yarn Tracked Nodes with $V_o = 1200$ ft/sec	35
27 Oblique Impact Deformations for $\mu = 0.1$	37
28 Oblique Impact Deformations for $\mu = 0.5$	38
29 Shear and Extensional Jamming Regions with $V_o = 1200$ ft/sec and $\mu = 0.5$	39
30 Von Mises Stress Plots Demonstrating Progressive Yarn Fractures (Iso-Crimp Case with $V_o = 1200$ ft/sec and $\mu = 0.5$)	40

LIST OF ILLUSTRATIONS (Cont'd)

Figure	Page
31 Von Mises Stress Plots for Case A with $V_o = 1200$ ft/sec and $\mu = 0.5$	40
32 Peak Magnitudes of FSP Resultant Rotational Velocities for $45^\circ/45^\circ$ Oblique Impacts ..	41
33 E_{rf} As a Percentage of FSP Kinetic Energy for Non-Through Penetrating $45^\circ/45^\circ$ Oblique Impacts ($\mu = 0.1$).....	42
34 E_{rf} As a Percentage of FSP Kinetic Energy for Non-Through Penetrating $45^\circ/45^\circ$ Oblique Impacts ($\mu = 0.5$).....	43
35 Ballistic Limit Curves for $45^\circ/45^\circ$ Oblique Impact Event with $\mu = 0.1$	45
36 Ballistic Limit Curves for $45^\circ/45^\circ$ Oblique Impact Event with $\mu = 0.5$	45
A-1 Tension Monitoring Locations for the Central-Most HCC (Warp) and LCC (Weft) Yarns.....	A-3
A-2 Yarn Tension History Plots for Normal Impacts: Iso-Crimp Case.....	A-4
A-3 Yarn Tension History Plots for Normal Impacts: Case C.....	A-5
A-4 Yarn Tension History Plots for Normal Impacts: Case B.....	A-6
A-5 Yarn Tension History Plots for Normal Impacts: Case A	A-7
B-1 Time-History Plots of FSP Kinetic Energies for Normal Impacts	B-3
B-2 Time-History Plots of Fabric Energies, Normal Impact with $V_o = 600$ ft/sec	B-4
B-3 Time-History Plots of Fabric Energies, Normal Impact with $V_o = 750$ ft/sec	B-5
B-4 Time-History Plots of Fabric Energies, Normal Impact with $V_o = 1200$ ft/sec	B-6
B-5 Time-History Plots of Fabric Energies, Normal Impact with $V_o = 1800$ ft/sec	B-7
B-6 Time-History Plots of Fabric Energies, Normal Impact with $V_o = 2400$ ft/sec	B-8
B-7 Time-History Plots of Fabric Energies, Normal Impact with $V_o = 3000$ ft/sec	B-9
C-1 Yarn Failure Plots for Oblique Impacts with $V_o = 600$ ft/sec	C-3
C-2 Yarn Failure Plots for Oblique Impacts with $V_o = 750$ ft/sec	C-4
C-3 Yarn Failure Plots for Oblique Impacts with $V_o = 1200$ ft/sec	C-5
C-4 Yarn Failure Plots for Oblique Impacts with $V_o = 1800$ ft/sec	C-6
C-5 Yarn Failure Plots for Oblique Impacts with $V_o = 2400$ ft/sec	C-7
C-6 Yarn Failure Plots for Oblique Impacts with $V_o = 3000$ ft/sec	C-8
D-1 Time-History Plots of FSP Kinetic Energies for Oblique Impacts.....	D-3
D-2 Time-History Plots of Fabric Energies, Oblique Impact with $V_o = 1200$ ft/sec	D-4
D-3 Time-History Plots of Fabric Energies, Oblique Impact with $V_o = 3000$ ft/sec	D-5

LIST OF TABLES

Table		Page
1	Mechanical and Geometric Properties of the Strings	10
2	Transverse Wave Arrival Times at String Boundaries (μsec)	11
3	String Model: Stress-Wave Arrival Times (μsec)	11
4	String Model: Stress-Wave Amplitudes at String Boundaries	12
5	Geometric Properties of Vectran Yarns	14
6	Mechanical Properties of Vectran Yarns	15
7	Crimp Contents for Model Cases.....	16
8	FSP Geometry and Mass Properties	17
9	Velocity and Primary Yarn Fracture Results for Normal Impacts	26
10	Peak Yarn Normal Displacements at $t = 10 \mu\text{sec}$	34
11	Velocity Components Corresponding to $45^\circ/45^\circ$ Oblique Impacts.....	36
12	Fabric Absorbed Energies for $45^\circ/45^\circ$ Oblique Impacts with Fixed LCC (Weft) Yarn Crimp Content of 1.2%	42
13	Fractured Yarn Counts for $45^\circ/45^\circ$ Oblique Impacts with Fixed LCC (Weft) Yarn Crimp Content of 1.2%	44

LIST OF ABBREVIATIONS, ACRONYMS, AND SYMBOLS

ARL-WMD	Army Research Laboratory's Weapons & Materials Directorate
α_{string}	Mass per unit length of strings
δ	Offset distance between crossing strings
CRIMP	Crimp-imbalanced protective
d_{fil}	Filament diameter
D_{string}	Diameter of strings
D_{FSP}	Diameter of FSP
DSM	(company name)
E	Elastic modulus of yarns
E_{damping}	Viscous damping energy
E_{friction}	Frictional energy
$E_{\text{dissipative}}$	Dissipative energy
E_{elastic}	Elastic strain energy
E_{irf}	Irrecoverable fabric energy
E_{kinetic}	Kinetic energy
E_{plastic}	Plastic strain energy
E_{rf}	Recoverable fabric energy
E_{string}	Elastic modulus of strings
E_{trans}	Sum of the absorbed and dissipated fabric energies
F_{cover}	Geometric cover factor
FEA	Finite element analysis
FSP	Fragment simulating projectile

LIST OF ABBREVIATIONS, ACRONYMS, AND SYMBOLS (Cont'd)

$F_{tension}$	Initial tension of strings
g	Gram
gpd	Grams per denier
HCC	High crimp content
I	Mass moment of inertia
KE initial	Initial kinetic energy of FSP
LCC	Low crimp content
L_{FSP}	Length of FSP
m	Mass
M_{FSP}	Mass of FSP
NIJ	National Institute of Justice
NUWC	Naval Undersea Warfare Center
μ	Coefficient of friction
μsec	Microsecond
ν	Poisson's ratio
N_{fils}	Number of filaments
N_{fpy}	Number of fractured primary yarns
N_{fytot}	Total number of failed primary and secondary yarns
N_{py}	Number of primary yarns
ω	Resultant rotational velocity
ω_{pitch}	Rotational velocity about pitch axis
ω_{roll}	Rotational velocity about roll axis
ω_{yaw}	Rotational velocity about yaw axis
ρ_{string}	Mass density of strings
ρ	Mass density of yarns
RCC	Right circular cylinder
σ_{tu}	Ultimate tensile stress of yarns
σ_{ty}	Tensile yield stress of yarns
STANAG	Standardization Agreement
t_{HCC}	Stress-wave arrival time at HCC yarn boundary
t_{perf}	Time to perforate the fabric
UD	Unidirectional
UHMWPE	Ultrahigh molecular weight polyethelene
V_o	Initial velocity of FSP
V_{50}	Ballistic limit
V_b	Ballistic limit velocity
V_f	Final velocity
$V_{rebound}$	Rebound velocity of FSP
$V_{residual}$	Residual velocity of FSP
V_{xslip}	x-component of slip velocity
V_{yslip}	y-component of slip velocity
3-D	Three-dimensional

CRIMP-IMBALANCED PROTECTIVE (CRIMP) FABRICS

INTRODUCTION

Lightweight, soft-armor systems have historically been constructed of plain-woven fabrics. Although weaving processes and associated textile manufacturing methods have matured, the lag in the development of next-generation, higher performing fibers suggests that the traditional protective-textile manufacturing process has plateaued* and may be threatened by a competing and growing emphasis on laminated unidirectional fabric armors—a paradigm shift for soft-armor design. Yet many potential methods to improve ballistic and fragment protection of woven armors, which could be initially evaluated through cost-effective, high-end numerical models, remain unexplored. For example, these models could assess potential performance improvements resulting from modifications to the woven architectures, hybrid fiber materials, multimodal yarns, mixed-denier fiber systems, and functionally graded layered systems before validation testing of fabric samples often produced in costly experimental mill runs.

This report documents the research that was conducted to explore the unique concept of using crimp imbalance, which is a simple architectural modification achieved during the weaving process, as a potential mechanism to enhance fragmentation and ballistic protection levels of single-ply woven fabrics. It is shown in this report that crimp imbalance (1) can substantially influence the energy-absorption levels of single-ply fabrics for select fragment simulating projectile (FSP) velocities, friction coefficients, and impact angles; (2) can be tailored to controllably delay stress-wave propagations among yarn directions; and (3) can minimize reflections at the yarn crossover regions. This research, which used numerical models of single-ply, plain-woven fabric, demonstrated that deviations in crimp contents can have significant effects on energy absorptions and projectile residual velocities; in short, optimal levels of crimp imbalance may exist for a specific ballistic threat type.

This report summarizes threat types and protection levels, highlights the historical developments in body armor materials and ballistic performance levels, and provides convincing modeling data (supported by detailed plots in appendixes A – D) that demonstrate why crimp imbalance is a significant factor in the design of protective fabrics. The overwhelming success of this investigation supports the need to extend this research to multi-ply fabrics. Coupled system effects associated with layer-to-layer interactions must be characterized for their influence on primary yarn migrations, stress-wave propagations, and blunt trauma deformations. The groundwork developed herein provides modeling efficiencies for next-generation, single- and multi-ply models—models subjected to impact by various-shaped projectiles, etc. Additionally, this research reinforces the contention that crimp contents should be specified as design parameters for soft-woven armors. Furthermore, crimp contents should be monitored and controlled during manufacturing to ensure that crimp contents of the finished product are within prescribed tolerances.

* The protective-textile market continues to wait for the production startup of Magellan-DuPont's new ultrahigh performance fiber known as M5, which was originally scheduled for a 2007 – 2008 commercial production start.

THREAT TYPES AND PROTECTION LEVELS

Woven textile materials are commonly employed in personnel, aircraft, and vehicle protection systems to guard against ballistic, fragment, and stab threats because of their lightweight and flexible performance attributes. Threat types and the protection levels required to defeat them dictate the necessary armor system designs. For example, ballistic threat protection levels are established based upon projectile types (such as deformable, steel-jacketed, high-hardness core, armor-piercing, etc.) and their kinetic energy levels in accordance with standards such as the National Institute of Justice (NIJ) Standard 0101.06¹ and Standardization Agreement (STANAG)-2920.²

For protection against deformable rounds fired from handguns, a layered woven fabric of up to 30 plies or more may be used. It has been shown that ballistic limit velocity V_b is proportional to the areal weight density of the fabric. (Alternatively, the V_{50} ballistic limit velocity is defined as the velocity at which complete penetration and partial penetration are both probable occurrences.) During impact, layers near the strike surface cause the projectile to deform while the majority of the projectile's kinetic energy is transferred to the fabric by stress waves propagating radially outward along each yarn direction and out-of-plane to successive layers. The velocity at which a stress wave travels in a yarn is dependent on the density and stiffness of the yarn. Stress-wave velocities in yarns increase with increasing yarn stiffness; therefore, yarns used in woven ballistic armors preferably contain little or no twist. Twist, which is generally used to increase the handling characteristics of the yarns, can produce higher strengths—but at the expense of reducing stiffness. The stress waves dissipate the projectile's kinetic energy through various mechanisms depending on friction, yarn material, and the fabric architecture chosen. The ability of an individual woven layer to transmit stress waves is significantly influenced by kinematic interactions (that is, crimp interchange, yarn slip, and rotation) occurring between crossing yarns.

Higher kinetic energy rounds associated with assault rifles, for example, and the use of high-hardness cores (that is, tungsten carbide, etc.) can easily lead to penetration of textile armors. For protection against these threats, woven fabrics may simply be one component of an integrated rigid armor system that may include a ceramic strike plate (for example, alumina oxide, silicon carbide, boron carbide, etc.) supported by a laminated fabric-reinforced polymer composite back plate. The hard ceramic strike face forces the projectile to fracture (that is, fragment) while the composite backing plate, which prevents tensile fractures of the brittle ceramic, and woven fabric layers arrest the ensuing fragments.

Armor design requirements for multiple threat types are not always mutually consistent; in fact, they can be antagonistic. For example, optimizing a multilayered woven fabric for ballistic threats will often reduce its stab resistance. Highly dense, tightly woven fabrics are required to defeat punctures from stab impacts. This type of construction, however, necessitates a high geometric cover factor (F_{cover}), which performs poorly during ballistic impact because of the severely restricted yarn motions. Past experience has demonstrated that multitreat armors, also referred to as “in-conjunction armors,” designed for combined ballistic and stab protections were essentially produced with two component armors: one for ballistic protection and one for

puncture resistance.³ Only minimal synergistic benefits were achieved in terms of total performance and weight savings. Care must be taken to provide the optimal fabric architectures and material systems designed to defeat multiple threats. Accordingly, the crimp-imbalanced protective (CRIMP) fabric architectures of the current research have the capacity to increase both stab and ballistic resistance simultaneously. This increased multithreat resistance will be demonstrated by using weaves constructed with an F_{cover} value that is considered appropriate for stab protection but considered excessively high for ballistic protection.

HISTORICAL DEVELOPMENTS IN BODY ARMOR MATERIALS AND BALLISTIC PERFORMANCE LEVELS

Today's woven fabric armors generally consist of yarns constructed from high-performance, multifilament, continuous, polymer fibers. The literature reserves the category of "high performance yarns" for those yarns providing tenacity levels of 23 gpd or greater. Examples of high-performance production fibers include the para-aramids such as Kevlar, Technora, and Twaron; the liquid crystal polymers such as Vectran and PBO; and the ultrahigh molecular weight polyethylenes (UHMWPE) such as Spectra and Dyneema. New ultrahigh performance fibers recently developed and near production-ready include the previously mentioned Magellan-DuPont M5 fiber, which is projected to have more than double the specific strength of Kevlar fibers.⁴ Current industry trends for woven-fabric armor products continue to shift toward the use of smaller yarn deniers, such as 500 to 200 and even below; however, the cost of finished fabrics for yarn deniers below 500⁵ becomes increasingly expensive.

Chen and Chaudhry⁶ discussed the historical developments and materials used that enabled body armors to serve as protective shields from ancient times to modern day systems. A detailed review of today's high-performance fibers commonly used in soft-body armor systems, ballistic impact mechanics, and ballistic threat classifications were summarized.

Tabiei and Nilakantan,⁷ whose paper referenced 176 relevant publications, provided an elaborate review summarizing prior research works on ballistic fabric modeling, experimental ballistic tests, mechanical properties and constitutive representations of yarns, fabric architectures, effects of projectile characteristics, and failure modes.

A recent paper by David, Gao, and Zheng⁸ provided a comparison of various body armor types, materials, and ballistic performance levels as well as identification of the energy-absorption mechanisms present in each.

The design of woven fabrics for structural and armor applications is complex because it requires an understanding of the related dynamics and the capability to optimize a system of systems. Numerous hierarchies are present—with the simplest one arguably being that of a single fiber. Multiple fibers (or filaments) are bundled to form a yarn, yarns are woven to form a fabric layer, and fabric layers are stacked and joined to form a panel. Mechanical properties,

however, do not efficiently translate across these hierarchies; that is, fiber properties do not directly translate to yarn properties, yarn properties do not directly translate to fabric properties and, likewise, single-ply behavior does not directly translate to multi-ply behavior for stacked layers. Details of the fiber, yarn, and fabric mechanical behaviors and their associated effects across these hierarchies are described by Hearle, Grosberg, and Backer⁹ and Freeston, Platt, and Schoppee.¹⁰

Parga-Landa and Hernandez-Olivares,¹¹ Chocron-Benloulou, Rodriguez, and Sanchez-Galvez,¹² and Gu¹³ developed analytical methods based on penetration mechanics to simulate the ballistic impact behavior of woven fabric armors.

Cunniff¹⁴ empirically addressed the system performance effects and their influences on woven ballistic fabrics for single-ply, stacked multi-ply, and spaced multi-ply fabric arrangements. Cunniff concluded that, for stacked multi-ply fabrics, the transverse shear and normal stresses, which increased with increasing ply count, degraded the ballistic performance of plies near the strike face. Alternatively, he observed that, for spaced multi-ply fabrics with no contact between layers, the ballistic protection levels were simply the sum of the protection levels from the individual plies. His work demonstrated the importance of establishing system behaviors of stacked multi-ply fabrics because such behaviors are not simply the cumulative sum of each single-ply performance.

Roylance, Chammas, Chi, and Scott¹⁵ developed finite difference-based numerical simulations using a network of pinned-joint elements. Initially, this method enabled effective formulation of multi-ply models by increasing the mass of yarns at the crossover nodes to capture the desired areal density and by scaling the stress-wave speeds accordingly. Subsequent enhancements of their code included yarn slippage and direct representation of multiple layers.

Zeng, Tan, and Shim¹⁶ developed numerical models of single-ply, plain-woven fabrics subjected to normal impacts using a network of pin-jointed, linear viscoelastic elements. The models were used to evaluate the energy-absorption capacities over a range of friction coefficients and projectile velocities. Their results showed that low inter-yarn friction permits migration of primary yarns away from the impact site and that excessive inter-yarn friction produces high stress concentrations at the impact site leading to premature yarn failures. Their work also concluded that the selection of boundary conditions became less influential with increasing projectile velocity as the time required to perforate the fabric was less than the time required for the transverse wave to reach the boundaries.

Lim, Shim and Ng¹⁷ conducted finite element modeling of a Twaron fabric subject to ballistic impact using a membrane representation. Their model accounted for material viscoelastic effects and employed a strain-rate-sensitive failure criterion. Excellent agreement was achieved between the residual velocity predictions and the experimental results.

Billon and Robinson¹⁸ performed analytical and numerical modeling of multi-ply homogeneous and hybrid woven fabrics subjected to ballistic impact and compared their modeling results to those obtained through experimental tests. Their numerical models were similarly constructed to those of Roylance and others¹⁵ (that is, the fabric layers were treated as a

collection of pinned joints; additional layers were effectively represented by increasing the areal weights assigned to nodes representing the crossover regions; and interactions between layers were neglected). Both homogeneous and hybrid multi-ply fabric cases were considered. Fabric layers were constructed from ballistic nylon, high molecular weight polyethylene and aramid materials. Their modeling results exhibited good comparisons to experimental tests for the hybrid (heterogeneous) multi-ply fabrics.

Figucia¹⁹ conducted ballistic impact testing of Kevlar fabrics. His results demonstrated that energy absorption was proportional to the target areal density and, for a multilayered fabric system of a given areal density, energy absorption increased as the areal density of the individual layers was reduced.

Hearle, Leech, Cork, and Adeyefa²⁰ compared the ballistic protection levels of several triaxial woven fabrics to biaxial woven fabrics through limited testing and analysis. Lim, Tan, and Cheong²¹ conducted ballistic tests on two-ply woven Twaron CT 716 fabrics using various projectile nose shapes such as hemispherical, flat, ogival, and conical. Their results demonstrated that energy-absorption levels for the two-ply systems were strongly influenced by the projectile nose geometry as the dominant energy-absorption mechanisms differed (that is, yarn sliding, yarn cutting, etc.). In comparison with single-ply performance, ballistic limits for the two-ply fabrics generally increased by 210%, with the noted exception arising from the flat-nosed projectile, which exhibited only a 150% increase.

The transition from woven to nonwoven armors remains actively engaged with the success of laminated unidirectional-fabric armor products, such as Honeywell's Spectra Shield and Gold Flex and DSM's Dyneema, etc. In contrast to woven armors, unidirectional (UD), layered armors fall within the class of nonwoven textiles in which no interlacing among yarn families exists and the crimp-interchange mechanism is not present. UD armors are constructed of multiple UD plies containing UHMWPE fibers often laminated with layers of compliant Kraton (Shell Chemical Company) film (matrix). Prior to lamination, an advanced spreading process is performed that aligns the fibers in a parallel arrangement across the armor surface to achieve a prescribed number of fiber ends per unit width. The recommended matrix content by volume is between 8% and 22%. The plies are then laminated under pressure according to a prescribed stacking arrangement (such as a cross-ply, angle ply, etc.) similar to conventional composite laminate designs. The absence of interlaced crossover regions eliminates the kinematic-based energy dissipation mechanisms associated with crimp interchange in wovens. Furthermore, the absence of crossover regions makes UD fabric armors less flexible than wovens, which can affect comfort levels. From an energy transfer perspective, the Kraton matrix provides a viscous-dissipation mechanism analogous to friction in woven fabrics. As the UHMWPE fibers fracture, the fiber tensile forces are transferred to the Kraton matrix, and, when the fiber/matrix bonds fail, shear strain energy is released and fiber slippage occurs in the matrix. The transfer of tensile force from broken yarns to the matrix is addressed through the shear lag theory.²²

Karahan²³ performed ballistic tests on two multilayered para-aramid fabric armor panels. One panel was configured with woven Twaron layers; the other panel consisted of UD Kevlar 129 fiber layers laminated in a cross-ply sequence. The ballistic test samples were

constructed using 20 to 32 plies. The UD Kevlar laminate panels absorbed more energy than did the woven Twaron panels with respect to unit weight because the UD fibers were more efficient in transferring energy than were the woven fibers. A comparison of the energy-absorption results as functions of layer counts was presented. Karahan showed that the energy absorbed per unit weights of the woven and UD panels decreased with increasing ply counts. This observation results from the fact that layers closer to the strike face absorb more energy than those positioned toward the back face.

The subject of modeling ballistic fabrics through analytical and numerical methods is amply described in the literature. Analytical methods are generally used to conduct parametric studies involving a limited number of state variables and energy transfer mechanisms; they are not particularly pursued for describing the complete ballistic impact event because of the abundant and naturally occurring nonlinearities inherent in the (1) yarn/fabric/projectile constitutive behaviors, (2) yarn-yarn kinematics, including extensional and shear jamming, (3) yarn-projectile contact, and (4) layer-layer contact. Numerical methods using high-end commercially available codes, which can explicitly represent the individual yarns while permitting yarn-to-yarn and yarn-to-projectile contact interactions, are uniquely robust for capturing the full architectural response of single and multilayered systems; however, the number of layers that can be modeled is strongly dependent on the computational assets available.

Limited data are often captured during ballistic experiments. Numerical models can serve as a tool to further explore those dynamic mechanisms observed in ballistic tests, such as interactions between yarns, layers, and projectiles. Furthermore, numerical models can provide quantification of specific energy transfer mechanisms that are not obtainable through ballistic experiments.²⁴

Investigators are increasingly developing numerical, finite-element-based models with explicit yarn representations while preserving the critical yarn-yarn and yarn-projectile contact interactions. These models permit, without restriction, the natural effects of friction on energy absorption to be directly addressed as yarn slip, fabric shearing, and crimp interchange.

Shockey, Erlich, and Simons²⁵ evaluated the ballistic resistance of plain-woven Kevlar, Spectra, and Zylon fabrics for enhancing the performance of lightweight fragmentation barriers used in commercial aircraft. Impact tests were conducted on the fabric specimens as well as on aluminum 2024-T3 skin for baseline purposes. The Kevlar, Spectra, and Zylon outperformed the aluminum on an areal density basis by 6 to 1, 7 to 1, and 12 to 1, respectively. Additional tests were performed on Zylon fabric specimens to compare the effects of using biaxially (four sides) clamped versus uniaxially (two sides) clamped conditions. The uniaxially clamped specimens absorbed 25% – 60% more energy than their biaxially clamped counterparts. Numerical finite element analysis (FEA) models were then developed with individual discretized yarns using three-dimensional (3-D) continuum elements. Both yarn-to-yarn and yarn-to-projectile contacts were supported; however, all contact was treated as frictionless. The numerical results successfully showed the effects of clamping conditions on energy absorption as observed in the experimental tests.

Duan, Keefe, Bogetti, and Cheeseman²⁶ and Duan, Keefe, Bogetti, Cheeseman, and Powers^{24,27} performed simulations on single-layer, plain-woven fabrics subjected to ballistic impact with a rigid spherical projectile using numerical models in which the yarns were explicitly represented with yarn-to-yarn and yarn-to-projectile interactions fully supported. Two friction cases were considered, namely $\mu = 0.5$ and $\mu = 0.0$ with the same value of μ assigned to both yarn-yarn and yarn-projectile contacts. Additionally, the effects of boundary conditions on energy absorption were investigated. Two edge-restraint cases were examined: one with all four edges clamped, and the other with only two edges clamped (that is, the edges of only one yarn family were clamped). Their results showed that increases in friction coefficient improved the fabric's energy absorbability, increased the number of primary yarns engaged, increased the impact load, and delayed the arrival time of the peak impact load. Furthermore, the selection of boundary conditions affected the projectile's residual velocity. More energy was absorbed with two clamped edges rather than with four, as demonstrated by reductions in residual velocity.

Tan, Shim, and Zeng²⁸ investigated the effects of crimp using a numerical model similar to that of Roylance et al.¹⁵ Two approaches were evaluated for incorporating yarn crimp. The first approach was an indirect method in which the element strain formulation was adjusted to account for the unrestricted yarn straightening associated with the low fabric strains observed in uniaxial fabric tensile tests. They noted that this method, however, did not allow the Poisson-like effects to occur that are typically observed in fabric tensile tests. The second approach modeled the yarns as interconnected elements arranged in a zigzag manner. Here, yarn stiffness was maximized when the elements became fully straightened. This method did not permit relative slip of the crossing yarns and, therefore, frictional dissipation energies were not developed. Both methods, however, provided good agreement with ballistic test results on single-ply, woven Twaron fabric.

Zeng, Shim, and Tan²⁹ experimentally concluded that the selection of clamped boundary configurations significantly influenced the energy-absorption capacity of the fabric targets. From their results, which agreed with the numerical findings of Duan et al.,²⁶ they also concluded that, because warp yarns generally contain more crimp than weft yarns because of differences in the weaving tensions, the antisymmetric deformation patterns of the four-clamped-edge configuration resulted from crimp differences between warp and weft yarns. The inward motions of the unclamped yarns in the two-clamped-edge configuration, however, masked the effect of crimp difference. Furthermore, their work investigated the influence of yarn slippage along the clamped boundaries, which generally occurs during ballistic experiments. It was shown through numerical modeling that some degree of slippage actually increases the energy-absorption capacity of the woven fabric, but does so at the expense of increased target deflection.

Joo and Kang³⁰ developed a numerical code similar to what Roylance et al.¹⁵ and Tan et al.²⁸ used to characterize up to nine energy-absorption mechanisms in multi-ply, woven-fabric armors. Three distinct impact categories were considered—non-perforating, mature perforation, and premature perforation—which were ranked from smallest to fastest projectile velocity. The influence of crimp interchange was accounted for indirectly in the element strain formulations. Results of each category were used to identify the key energy-absorption mechanisms. For the range of projectile velocities considered, crimp interchange was an important energy-absorption mechanism, and the contributions of yarn bending stiffness were insignificant.

Many modeling studies found in the open literature were focused on improving the robustness of the solutions obtained. Few studies actually used numerical simulation as a tool to evaluate alternative fabric concepts seeking to improve protection levels. Fortunately, many optimization possibilities exist, including crimp imbalance, hybrid fabric systems, bi-modulus yarns, addition of bias yarns, and leno weaves—all of which can be readily evaluated through numerical methods and subsequently validated with experiments. Significant benefits achieved in computational mechanics have enabled researchers to remove restricting assumptions that once resulted in oversimplified solutions. Today's high-end computational analysis systems are extremely capable of providing numerical solutions to alternative construction concepts.

The literature also revealed that most studies generally lacked sufficient descriptions of the fabric constructions. For example, it is inadequate to describe the fabric construction based solely on the counts of warp and weft yarn ends; this research shows that crimp contents along both yarn directions, which can significantly influence protection levels, are required in addition to the yarn end counts. While warp yarns generally contain more crimp than weft yarns as a pure consequence of the weaving process, this study includes for baseline purposes an iso-crimp case that assumes equivalent crimp contents among yarn families. Few studies were identified in which woven fabrics constructed with imbalanced crimp contents were investigated. No studies were found in which multiple crimp-imbalanced constructions were evaluated and directly compared for ballistic protection.

COMPARISON OF WAVE PROPAGATIONS IN WOVEN AND UD FABRIC ARMORS

Stress and transverse wave propagations in yarns are different when the yarns are used in woven versus UD fabrics. A woven fabric is constructed of interlaced yarns that form crossover points. The crossover points act as semitransparent boundaries by reflecting a portion of the transmitted energy along each yarn direction back to the impact zone. Reflections redistribute energy among yarn families. Depending on the levels of crimp contents and yarn densities, the crossover points can alter the transmissibilities of both stress and transverse deflection waves caused during impact events, which in turn affects the spatial and temporal distributions of fabric strain energy, fabric dissipation energy (such as frictional, damping, etc.), and fabric kinetic energy. Because heat dissipation, acoustic energy, and all rotational kinetic energies of the projectile are assumed to be negligible, the governing energy balance expressed in equation (1) must be satisfied for all time during the impact event.

$$\frac{1}{2}m(V_o^2 - V_f^2) = E_{damping} + E_{elastic} + E_{friction} + E_{kinetic} + E_{plastic}, \quad (1)$$

where m is the mass of the FSP, V_o is the initial velocity of the FSP, V_f is the final velocity of the FSP ($V_f = 0$ for non-through-penetrating impacts), $E_{damping}$ is the energy dissipated through viscous damping, $E_{elastic}$ is the fabric elastic strain energy, $E_{friction}$ is the energy dissipated through friction at the yarn-yarn and yarn-FSP contact interfaces, $E_{kinetic}$ is the fabric kinetic energy, and $E_{plastic}$ is the dissipated plastic strain energy of the fabric.

With the appropriate crimp imbalance, stress waves in woven fabrics can be allowed to propagate along the lower crimp content (LCC) yarns without sensing the presence of the crossing higher crimp content (HCC) yarns. The stress-wave arrival times among crossing yarns can be decoupled in such a way that an HCC yarn remains active where a crossing LCC yarn may have previously fractured. Additionally, the reflected waves are delayed in time because the incident waves traveling along the LCC yarns propagate farther outward, thus distributing energy farther away from the impact zone.

Crimp modifications, which can be tailored to meet specific threat types, can be used to selectively (1) increase the energy absorbability of woven fabric armors, (2) increase V_{50} levels and (3) control the size of the affected zone, which can influence multi-hit performance.

A simple string model is presented to demonstrate the dynamic behavior and advantages of crimp imbalance on woven fabrics subjected to dynamic loads. Both stress and transverse wave propagations are described by Smith, Blandford, and Schiefer³¹ for single yarns of infinite length (that is, unconstrained) and by Gu¹³ for single yarns of finite length (that is, constrained).

The example string model consists of one principal string (LCC) AB orthogonally arranged among two parallel crossing strings (HCC) CD and EF as depicted in figure 1.

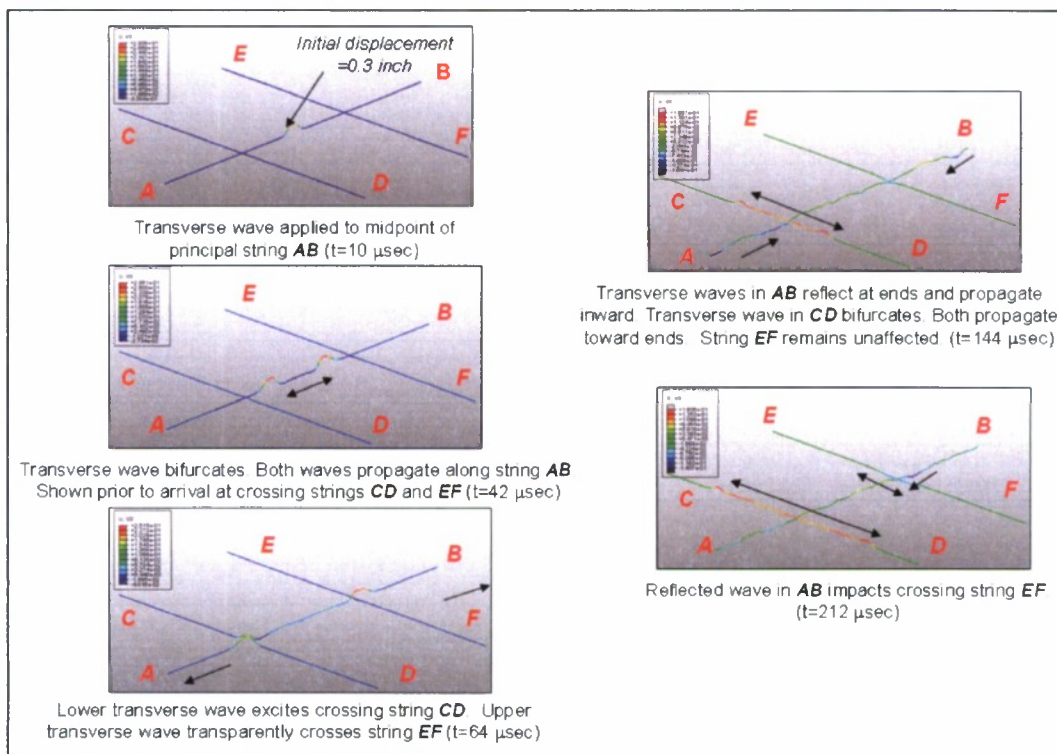


Figure 1. Effects of Crimp on the Transverse Waves
(Shown for $\delta = 0.10$ Inch)

Crossing string CD is offset above the principal string by δ ; crossing string EF is offset below the principal string by δ . The offset distance δ represents a simplified source of crimp imbalance. Mechanical and geometric properties of the strings are shown in table 1. Simple damping was provided in the form of a bulk viscosity assumed to behave linearly with volumetric strain rate. Each string is initially unstressed. Fixed displacement boundary conditions are assigned to the ends of each string. The model is excited by subjecting the midspan node of the principal string to an enforced transverse displacement of 0.3 inch. Transverse and stress-wave propagations and the energy distributions between the principal and crossing strings were monitored for characterizing their dependence on δ .

Table 1. Mechanical and Geometric Properties of the Strings

Property	Value
Elastic Modulus E_{string}	1.275 ksi
String Diameter D_{string}	0.01 in
Mass Density ρ_{string}	2.3030E-04 lb/in ³
Mass per unit Length α_{string}	1.809E-08 lb/in
Bulk Viscosity Damping Coefficient	0.06
Initial Tension $F_{tension}$	0 lb

Time-history results of the transverse waves demonstrated that the amplitudes produced in the crossing strings decreased by 45% as δ increased from 0.01 inch to 0.10 inch as shown in figure 2. The transverse wave arrival times are listed in table 2. Arrival times of the transverse waves in crossing strings CD and EF were extended by 10.2 μ sec and 135.7 μ sec, respectively, as δ increased accordingly. The latter delay is explained as follows. For $\delta = 0.01$ inch, the transverse wave in string AB impacted string EF upon the first crossing. Alternatively, when $\delta = 0.10$ inch, the transverse wave in string AB transparently traversed string EF and, only after the wave reflected at the boundary, did the impact occur with string EF . The transverse waves produced in the crossing strings were out of phase because of their alternating over/under placements relative to the principal string.

The stress-wave arrival times are listed in table 3. Stress waves traveling along principal string AB oscillated from its center to its boundaries several times prior to excitation of the first engaged crossing string CD and later followed by excitation of the second crossing string EF . Stress amplitudes at the string boundaries reduced with increasing δ as shown in table 4.

The time-history results of the various energy terms are shown in the plots in figure 3. Energies transferred from principal string AB to crossing strings CD and EF reduced considerably with increasing δ . Furthermore, arrival times of the traveling transverse waves within the crossing strings were shifted in time.

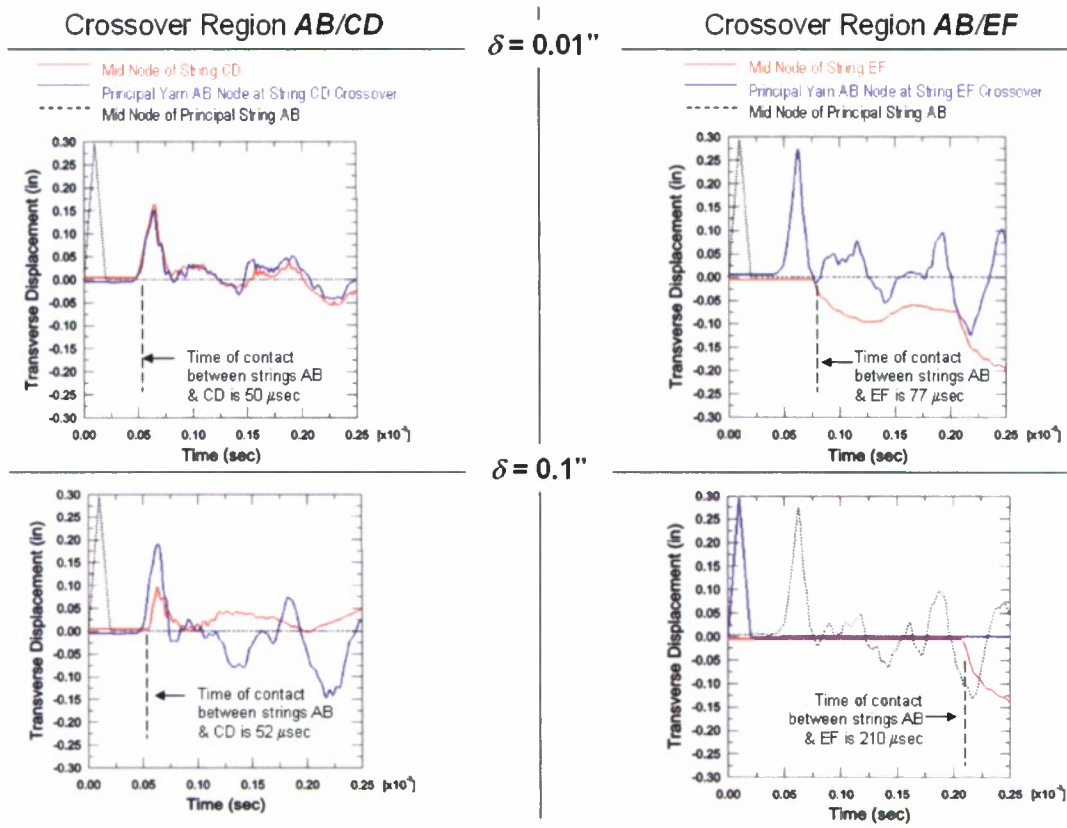


Figure 2. Transverse Wave Time-Histories at Crossover Regions

Table 2. Transverse Wave Arrival Times at String Boundaries (μsec)

Yarn	Offset Distance Between Crossing Strings		Delay (μsec)
	$\delta = 0.01$ Inch	$\delta = 0.10$ Inch	
AB	134.3	134.3	0.0
CD	256.2	300.1	43.9
EF	516.3	576.1	53.7

Table 3. String Model: Stress-Wave Arrival Times (μsec)

Yarn	Offset Distance Between Crossing Strings			
	$\delta = 0.01$ Inch		$\delta = 0.10$ Inch	
	at String Center	at String Boundary	at String Center	at String Boundary
AB	0.0	20.0	0.0	20.0
CD	46.1	70.2	56.3	76.3
EF	76.3	98.2	212.0	232.0

Table 4. String Model: Stress-Wave Amplitudes at String Boundaries

Yarn	Stress -Wave Amplitudes at Boundaries (psi)		% Reduction
	$\delta = 0.01$ Inch	$\delta = 0.10$ Inch	
AB	1,142,530	1,142,530	0.0
CD	406,404	336,915	17.1
EF	280,607	177,106	36.9

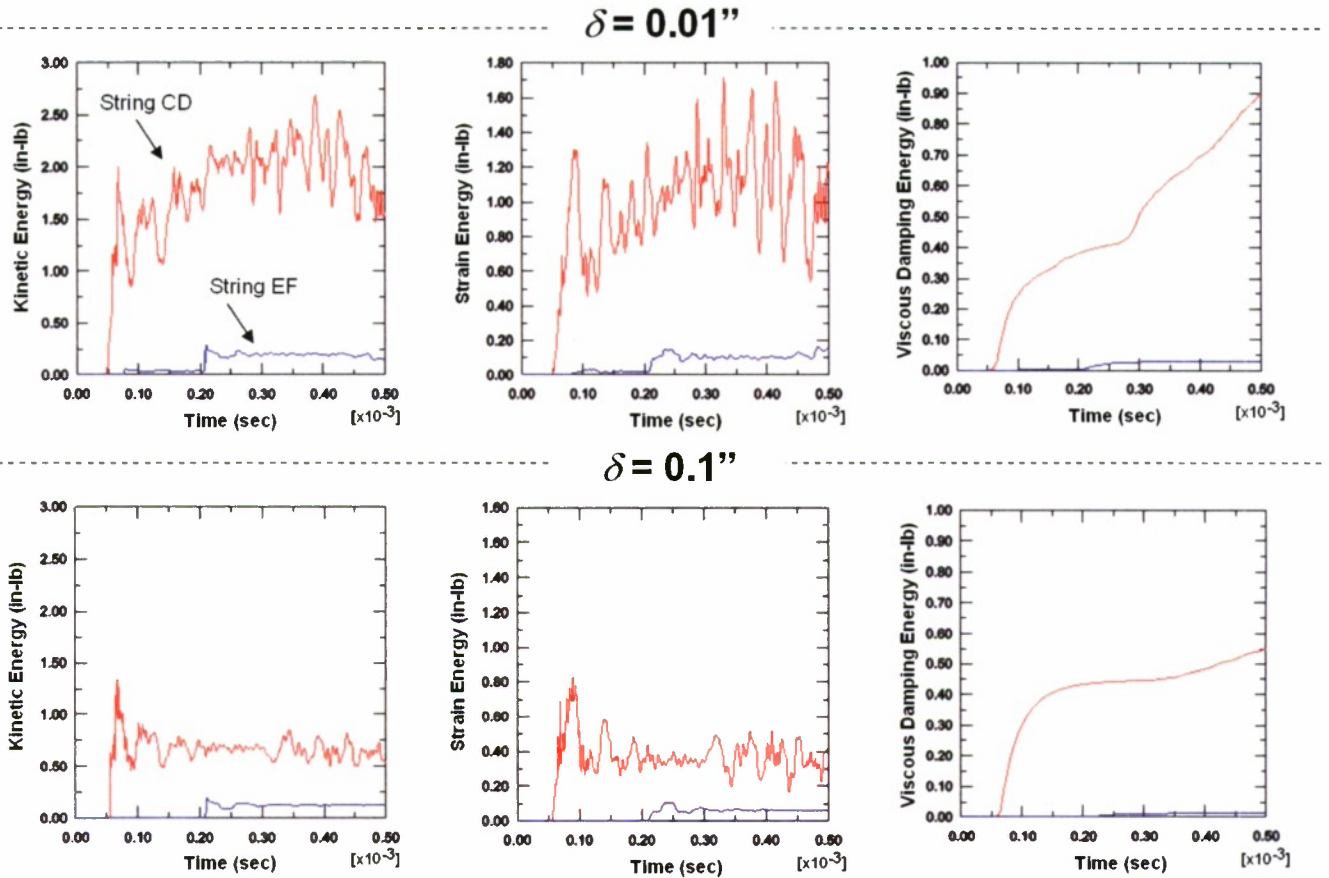


Figure 3. Energy Time-History Results as Functions of δ

This string model demonstrates the effectiveness of crimp-imbalance to (1) shift the arrival times of stress waves and transverse waves between yarn families, (2) distribute energy farther outward from the impact zone than is possible with an iso-crimp fabric, (3) reduce amplitudes of reflected waves developed at crossover regions, and (4) provide extended protection by allowing the HCC yarns to remain active longer at the crossover regions where LCC yarns may have previously failed.

CURRENT RESEARCH AND APPROACH

Because of the focus on protection against fragmentation devices, tests on fabric armors are often performed using FSPs. The tests use rigid right-circular cylinders (RCCs) as projectiles sized according to a 2-, 4-, 16-, and 64-grain size series. Furthermore, RCCs do not deform during impact with fabric armors. Studies conducted by the U.S. Army's Ballistic Research Laboratory³² established that 95% of all bomb fragments under 4 grains (0.26 gram) have a limit velocity of 3000 ft/sec or less. These studies further determined that a textile system with a minimum areal weight density of 1.1 lb/ft² was required to defeat fragment threats of the complete grain series at limit velocities.

The present research considers only the 2-grain RCC FSP at velocities of 600, 750, 1200, 1800, 2400, and 3000 ft/sec. The 2-grain RCC is the smallest of the FSP series and was, therefore, chosen because it provides the greatest potential to penetrate the fabric by simple yarn migration with or without the occurrence of yarn breakage. Two impact orientations were considered: (1) a normal event (90°) and (2) an oblique event (combined 45° off-normal and 45° in-plane with respect to either yarn family). The in-plane component of the firing axis of the oblique event was aligned along an equibaised orientation with respect to the warp and weft yarns.

The approach for simulating the impact response of a single-layer textile target subject to normal and 45°/45° oblique impacts is as follows:

1. Measure the residual kinetic energies in models experiencing full perforation.
2. Measure the rebound kinetic energies in models experiencing rebound.
3. Quantify the number of primary yarns active in perforating and non-perforating events.
4. Determine the effects of crimp imbalance and friction over the range of FSP initial velocities considered.
5. Identify the principal observed fabric deformation modes, such as shear jamming and extensional jamming.
6. Quantify the relative slip velocities between adjacent primary yarns versus FSP initial velocities.
7. Discuss the observed trends in energy absorption for the iso-crimp and crimp-imbalanced fabric architectures.

Numerical models of a plain-woven Vectran fabric in which the yarns were explicitly represented were developed. In addition to elastic-plastic yarn constitutive behavior, full kinematic behaviors arising from yarn-to-yarn and yarn-to-FSP interactions were preserved. Preservation of yarn motions ensured that yarn-to-yarn contact, friction, slip, and rotation at the crossover regions occurred—all of which are necessary for crimp interchange to develop without artificial restriction.

There are many examples of single-layer models in which the yarns are completely and explicitly represented with full contact surface interfaces described in the scientific literature; far fewer examples of multilayered models with the same yarn representations are available because of the computational costs for multilayered modeling.

SINGLE-PLY MODEL

Finite element models of single-ply, plain-woven Vectran targets were generated using a Fortran preprocessing code. The code was written to efficiently generate complete input decks based on user specification of fabric construction parameters (that is, yarn dimensions, yarn end counts, spacings, and crimp contents), material properties, contact surface definitions, boundary conditions, element sizes, FSP dimensions, and velocities. Additionally, contact surface definitions of all yarns and the FSP were automatically created. Solutions were obtained using the ABAQUS explicit finite element solver.³³

The yarns were represented as zero-twist Vectran yarns (tows) using membrane elements. Though such elements do not support through-thickness deformations, yarn compaction at the crossover regions was assumed negligible because of the small yarn thickness-to-width aspect ratios that were considered. Furthermore, strain energy caused by bending was assumed negligible, which is consistent with Joo and Kang³⁰ and Cavallaro, Sadegh, and Quigley.³⁴ As 3-D continuum and shell elements are formulated to include bending strain energies, their use would yield artificially stiff responses affecting the governing energy balance. Additionally, the use of 3-D continuum elements severely restricts the number of layers possible for future modeling of multi-ply fabric targets. The use of membrane elements was necessary to allow larger quantities of yarns to be modeled—especially in multilayered models.

For this investigation, it was decided that the fabric modeled would be constructed of multiple, continuous filament, non-twisted Vectran yarns (that is, tows) in the 1000-denier series arranged in a plain-woven architecture of 28 warp yarns x 28 weft yarns. Table 5 lists the filament counts N_{fils} and cross-sectional areas for the commercially available Vectran yarns as a function of denier. Yarn cross-sectional areas were computed based on the product of N_{fils} and filament diameter d_{fil} of 9.0551E-04 inch (23.0 microns). The resulting warp and weft yarn widths used in each model were 0.025 inch. Fixed displacement boundary conditions were applied to simulate clamped constraints at the yarn ends and along the outer edges of those yarns defining the swatch boundaries.

Table 5. Geometric Properties of Vectran Yarns

Denier	Thickness (in)	N_{fils}	Yarn Area (in ²)
1500	0.007728	300	0.0001932
1000	0.005152	200	0.0001288
750	0.003864	150	0.0000966
500	0.002576	100	0.0000644
300	0.001546	60	0.0000386

Because the selection of boundary conditions used in this research was discretionary, it is recommended that future efforts consider the range of boundary conditions commonly employed in the literature. For example, several researchers^{25, 26, 27, 29} have investigated the influence of boundary conditions by comparing the energy absorptions for models with four clamped edges, two clamped edges, four clamped corners clamped, and no clamped constraints. Ultimately, the selected boundary conditions warrant justification based on matching the farfield stress distributions expected within the end product.

Mechanical properties of the Vectran yarns are presented in table 6. Vectran was chosen for the current study because its tenacity level is at the midrange of the high-performance fibers category typically used in fabric armors. Elastic-plastic constitutive behavior was assumed based on the tensile yield σ_{ty} values and ultimate tensile strength σ_{tu} value. In the absence of available material damping properties, the linear bulk viscosity described in the string model was used to represent the sole source of damping in the Vectran yarns. Viscoelastic effects were not included at this time. A tensile failure criterion was employed in which elements having integration point stresses exceeding σ_{tu} were deleted from the model with no further mass or stiffness contributions made during the remainder of the impact event. As constructed, the models support damage caused by yarn pullout, fracture at impact sites, fracture at yarn boundaries, and partial yarn fractures.

Table 6. Mechanical Properties of Vectran Yarns

Property	Value
Tenacity	28.0 g/denier
Density ρ	1.300E-04 lbm/in ³
Elastic Modulus E	11,400 ksi
Poisson's Ratio ν	0.3
Tensile Yield Stress σ_{ty}	460 ksi
Ultimate Tensile Stress σ_{tu}	465 ksi
Bulk Viscosity Damping Coefficient	0.06

Four crimp content cases, as shown in figure 4, were evaluated using a fixed LCC (weft) yarn crimp content of 1.2% and described in table 7. The geometric cover factor F_{cover} was 99.56% for each crimp case. It is important to note that the number of yarn ends per unit length was equal for all four crimp models described in table 7. However, a consequence of increasing crimp imbalance for a given LCC crimp content was additional fabric mass. Areal weight densities increased as a function of increasing crimp imbalance, as shown in figure 5. The maximum weight increase of the cases considered was 10%, which occurred for case A.

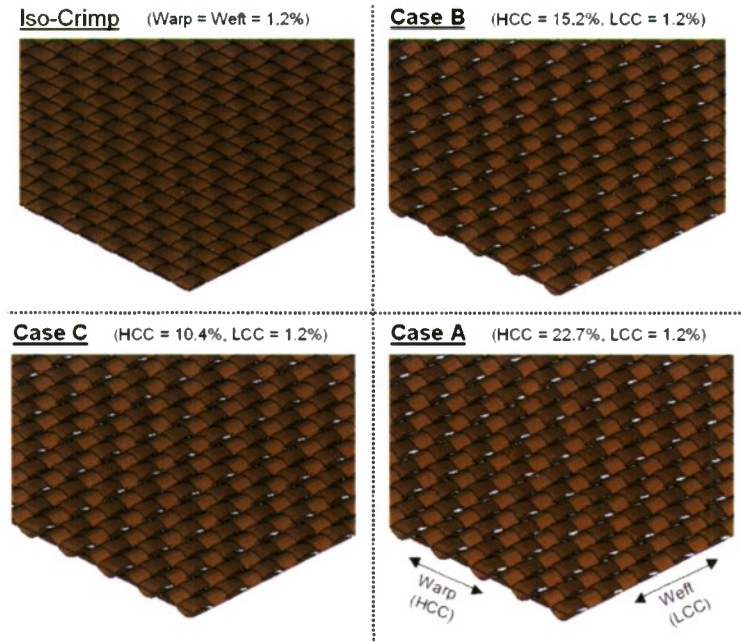


Figure 4. Views of Crimped Fabric Model Cases

Table 7. Crimp Contents for Model Cases

	Crimp Contents (%)		HCC-to-LCC Ratio
	HCC (Warp)	LCC (Weft)	
Case A	22.7	1.2	18.92
Case B	15.2	1.2	12.67
Case C	10.4	1.2	8.67
Iso-Crimp	1.2	1.2	1.00

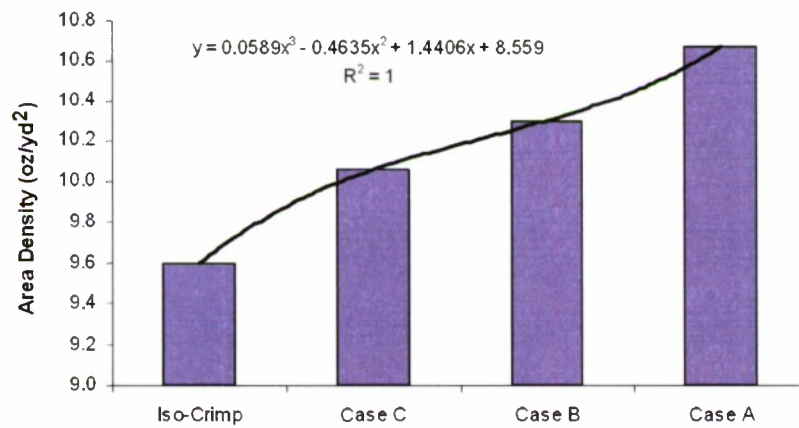


Figure 5. Areal Weight Densities for Model Cases

The FSP was modeled as a non-deformable (rigid), RCC with geometry and mass properties as shown in table 8.

Table 8. FSP Geometry and Mass Properties

Property	Value
Diameter D_{FSP}	0.11 inch
Length L_{FSP}	0.11 inch
Aspect Ratio (L_{FSP}/D_{FSP})	1.0
Material	steel
Mass M_{FSP}	2.05 grains

The FSP degrees of freedom are shown in figure 6. Six initial velocities (V_o) along the longitudinal axis were considered, namely 600, 750, 1200, 1800, 2400, and 3000 ft/sec and all initial rotational velocities (that is, ω_{yaw} , ω_{pitch} , ω_{roll}) were zero. Because no symmetry boundary conditions were sought, no constraints were applied to restrict the FSP rigid body motions. Rather, the effects of fabric deformations were allowed to alter the trajectory of the FSP during non-perforating (rebound) and perforating impacts. Other researchers have imposed symmetry boundary conditions to maximize the effective model size while minimizing solution times.

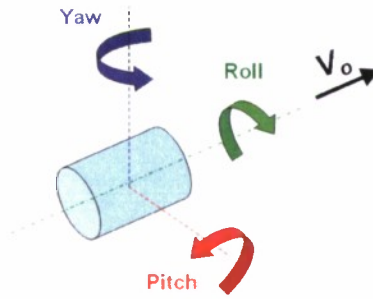


Figure 6. FSP Degrees of Freedom

Kinematic behaviors of the yarn-yarn and yarn-FSP contact interactions were governed by using simple isotropic, Coulomb friction. Here, a common coefficient of friction, μ , was used for both types of interactions—each assuming μ to be invariant with contact pressure, slip rate, and temperature. Two values of μ were used, namely 0.1 and 0.5, to establish a reasonable range of frictional influence on energy absorption.

Full perforation is said to have occurred when the following two conditions are satisfied: (1) the FSP must have a non-zero, final velocity magnitude and (2) the velocity vector cannot reverse from its initial direction.

For non-fully perforating impacts, the rebound velocities $V_{rebound}$ will be recorded and the ratio $V_{rebound}^2/V_o^2$, which represents the amount of recoverable (elastic) energy E_{rf} , absorbed by

the fabric, will be obtained by equation (2). During rebound, E_{rf} is transferred to the FSP; that is, after arrest, the fabric performs work on the FSP.

$$E_{rf} = E_{elastic} + E_{kinetic} = \frac{1}{2}mV_o^2 - E_{damping} - E_{friction} - E_{plastic}. \quad (2)$$

An upper limit of $V_{rebound}$ for non-perforating impacts using a rigid FSP can be derived by equation (3). It is assumed that the rebound kinetic energies are entirely converted to translational kinetic energies (that is, no rotational kinetic energies are developed in the FSP with respect to the yaw, pitch, or roll axes).

$$V_{rebound} = \sqrt{\frac{2}{m}(E_{elastic} + E_{kinetic})}. \quad (3)$$

Since energy is conserved during impact, the total energy absorbed by the fabric is simply the difference between initial and residual kinetic energies of the FSP. For normal impacts, the projection of the FSP center position was directly aligned at the gap formed between primary yarns as shown in figure 7 rather than directly on a crossover region. This alignment was expected to yield lower bound energy-absorption levels, as discussed by Tabiei and Nilkantan,⁷ because of the increased probability that the projectile would slip through the fabric because of yarn migrations. Primary yarns are defined as those yarns remaining in direct contact with the FSP throughout the impact event. By contrast, secondary yarns do not experience direct contact with the FSP.

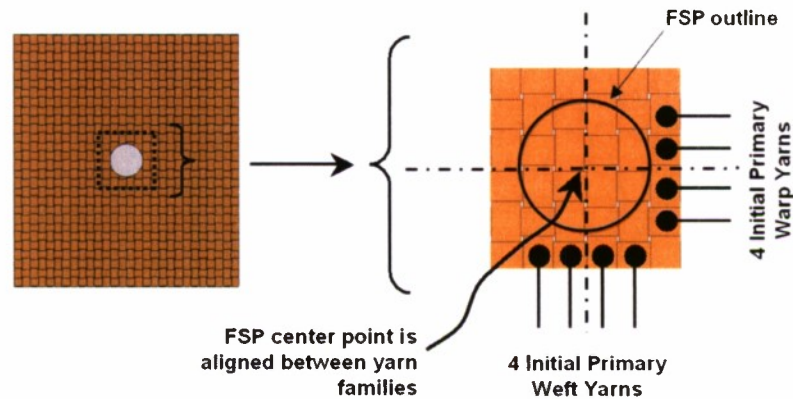


Figure 7. FSP Center Projection on Woven Fabric Target Subject to Normal Impact

Only one oblique impact orientation was considered in this investigation, namely a 45°/45° event in which the FSP was oriented 45° off the normal axis and 45° along the in-plane bias direction as shown in figure 8. This orientation was selected because it was expected to produce large shearing and slip deformations leading to larger viscous-dissipation energies than those observed in normal impact events.

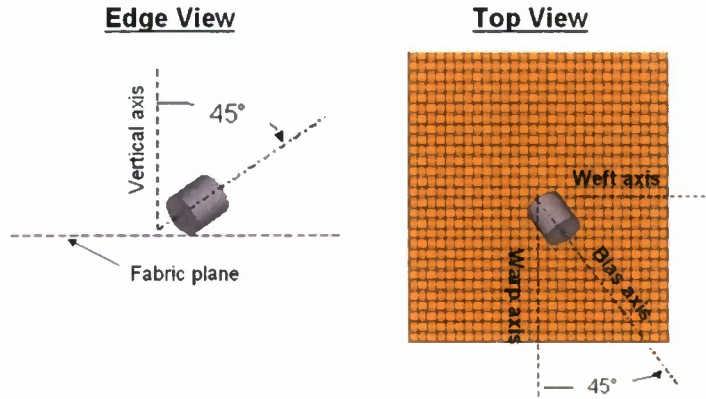


Figure 8. FSP Orientation for 45°/45° Oblique Impact

NORMAL IMPACT RESULTS

For fully perforating impacts, the residual velocities $V_{residual}$ and the number of fractured primary yarns N_{fpy} were recorded. Deformation plots for the normal impacts are shown in figures 9 – 12 for each crimp case, FSP velocity, and coefficient of friction (yarn-to-yarn and yarn-to-FSP). Residual velocity results versus V_o are graphically presented in figures 13 and 14.

Total energies absorbed by the fabric, expressed as a percentage of the FSP initial kinetic energy, are shown in figures 15 and 16. Similarly the recoverable and irrecoverable fabric energies are plotted in figures 17 and 18. Figure 18 shows that E_{rf} decreased with increasing crimp imbalance while the iso-crimp construction maximized E_{rf} . This result occurred because the irrecoverable fabric energy E_{irf} , namely, the sum of $E_{damping}$, $E_{friction}$, and $E_{plastic}$, increased with increasing crimp imbalance, which is further explained by the observation that increasing crimp imbalance produced greater plastic strains in the LCC yarns and greater dissipative energies among the HCC yarns. Energy absorbed by the fabric as viscous damping energy increased as friction decreased. This result was expected because relative yarn mobilities increased with decreasing friction. Alternatively, energy absorbed by the fabric in the form of kinetic energy increased with increasing friction. The increased viscous damping energies (portion of irrecoverable energy) of the fabric realized through the lower coefficients of friction were generally offset by the fabric's decreased kinetic energies (portion of recoverable energy).

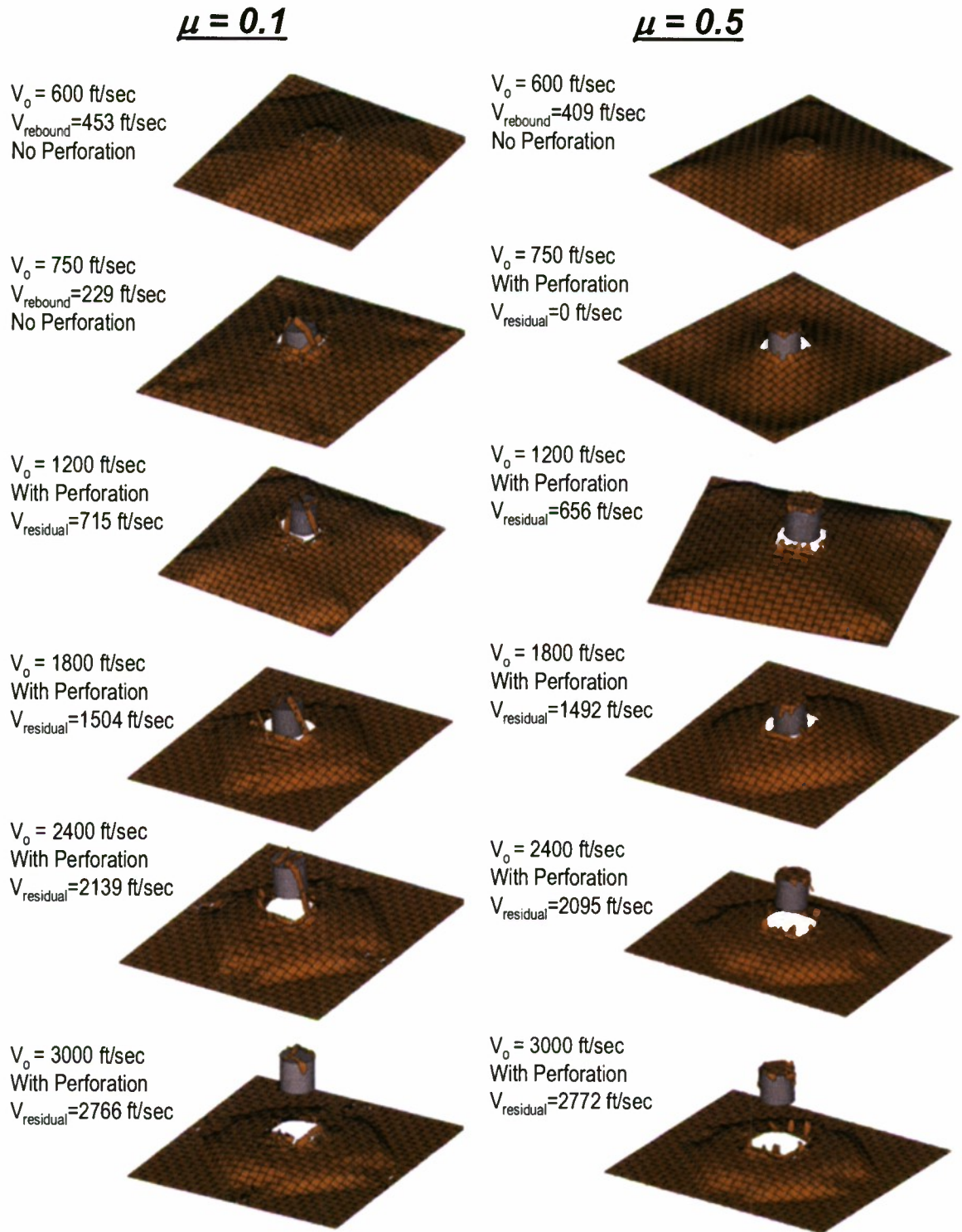


Figure 9. Impact Deformations As Functions of FSP Initial Velocity: Iso-Crimp Case

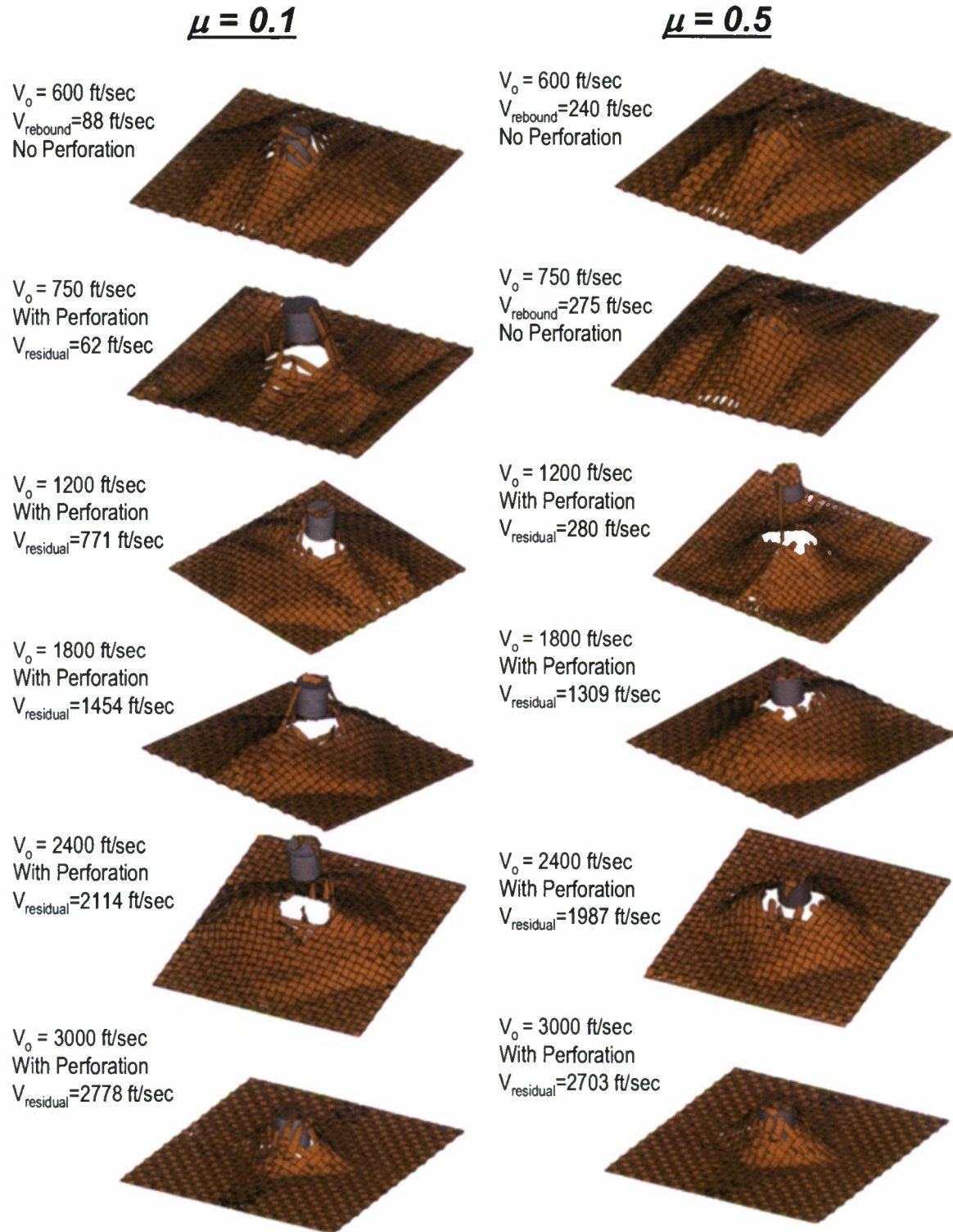


Figure 10. Impact Deformations As Functions of FSP Initial Velocity: Crimp Case C

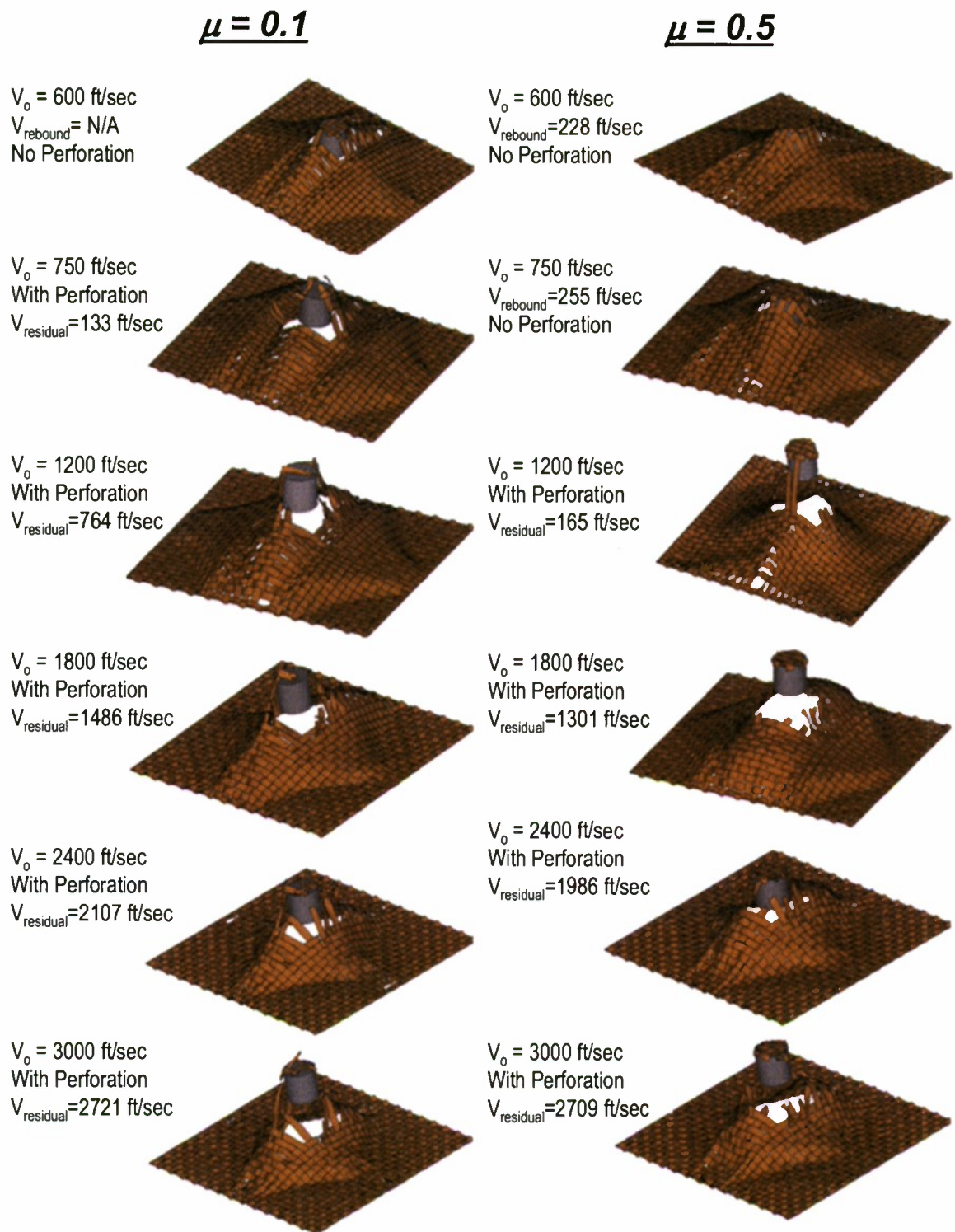


Figure 11. Impact Deformations As Functions of FSP Initial Velocity: Crimp Case B

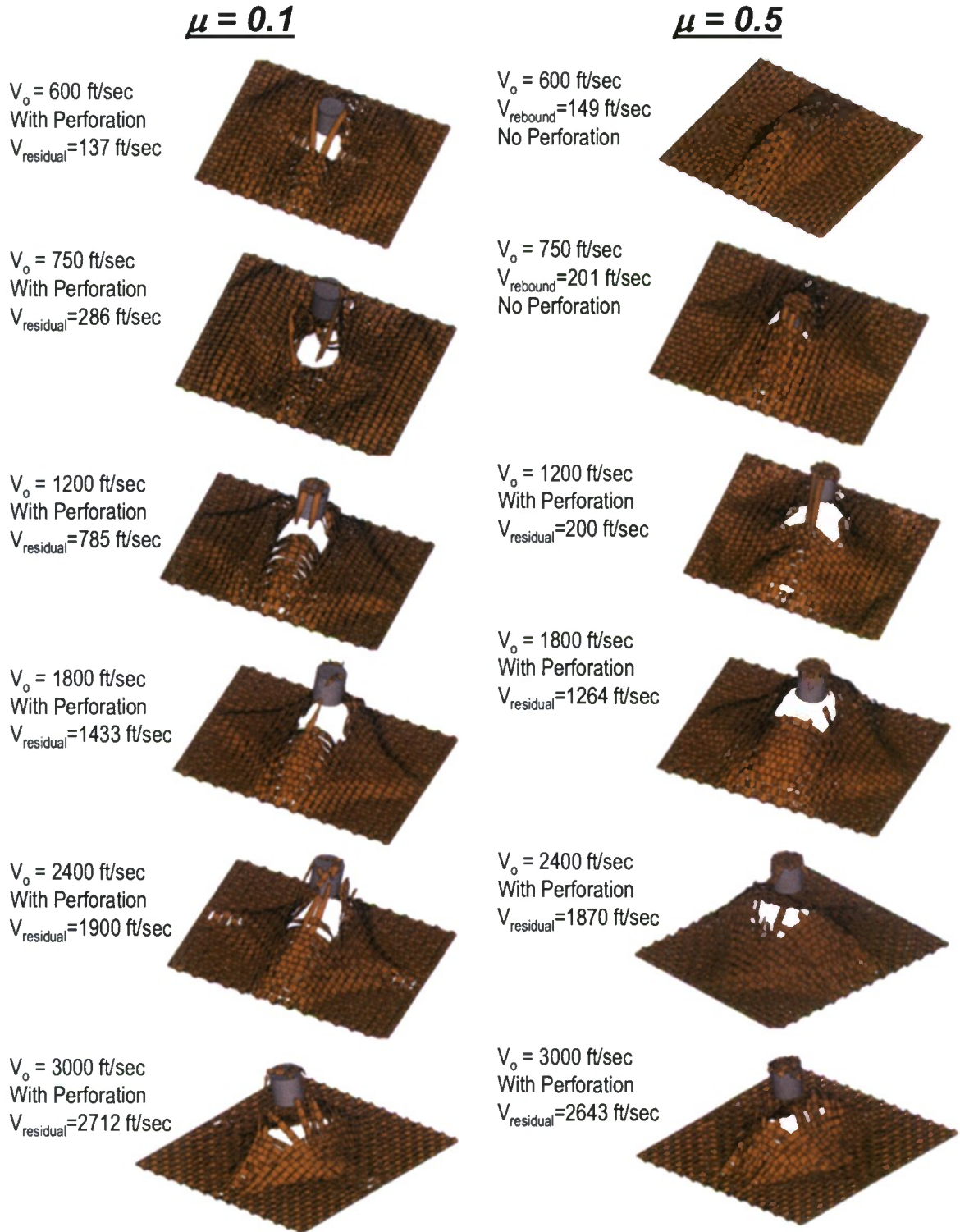


Figure 12. Impact Deformations As Functions of FSP Initial Velocity: Crimp Case A

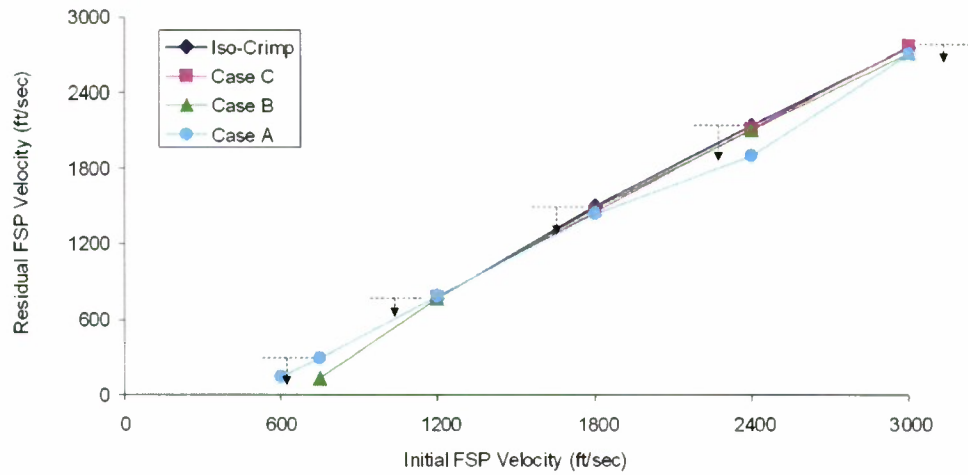


Figure 13. Residual Velocities for Fully Perforated Normal Impacts, $\mu = 0.1$

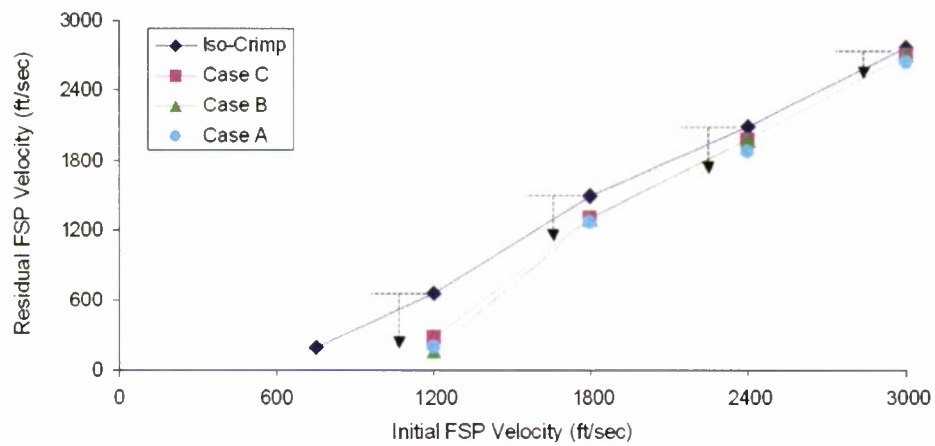


Figure 14. Residual Velocities for Fully Perforated Normal Impacts, $\mu = 0.5$

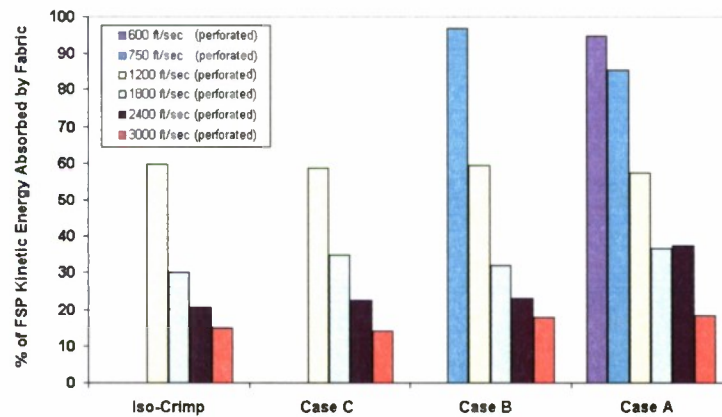


Figure 15. Percentage of FSP Kinetic Energy Absorbed by Fabric for Fully Perforated Normal Impacts, $\mu = 0.1$

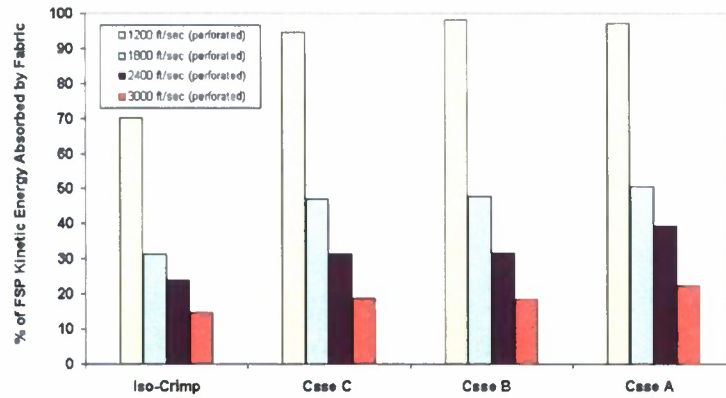


Figure 16. Percentage of FSP Kinetic Energy Absorbed by Fabric for Fully Perforated Normal Impacts, $\mu = 0.5$

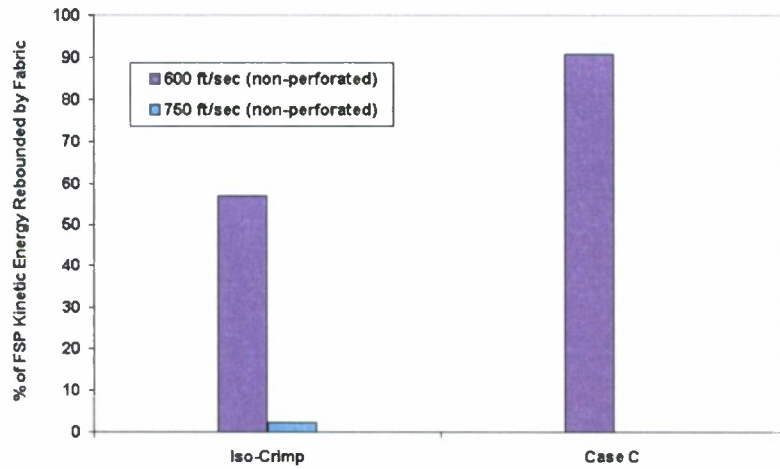


Figure 17. E_{rf} As Percentage of FSP Kinetic Energy for Non-Fully Perforated Normal Impacts, $\mu = 0.1$

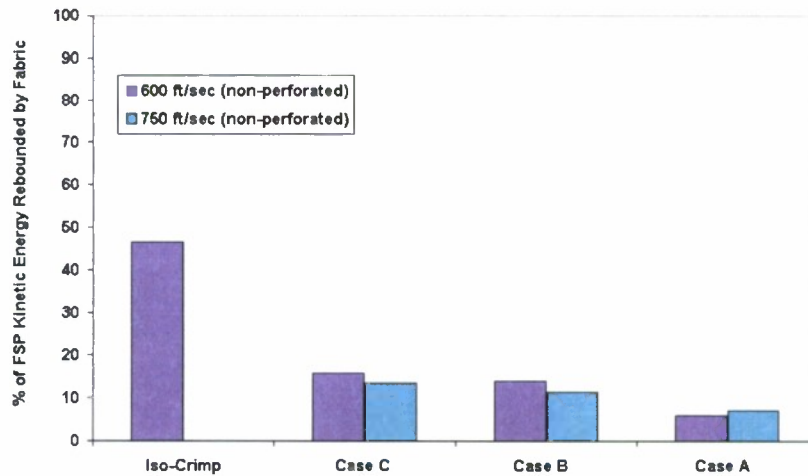


Figure 18. E_{rf} As Percentage of FSP Kinetic Energy for Non-Fully Perforated Normal Impacts, $\mu = 0.5$

Residual velocity and primary yarn fracture results are listed in table 9. Fractures always initiated in the LCC yarns of the crimp-imbalanced cases prior to fractures in the HCC yarns regardless of friction coefficient μ . Full perforation occurred for all crimp cases with $V_o \geq 1200$ ft/sec regardless of friction coefficient μ .

Table 9. Velocity and Primary Yarn Fracture Results for Normal Impacts

FSP Initial Velocity V_o (ft/sec)	Crimp Case	$\mu = 0.1$		$\mu = 0.5$	
		Residual (Rebound) Velocity (ft/sec)	N_{fpy}	Residual (Rebound) Velocity (ft/sec)	N_{fpy}
600	A	137	0	(149)	No Perforation
	B	(N/A)	No Perforation	(228)	No Perforation
	C	(88)	No Perforation	(240)	No Perforation
	Iso-Crimp	(453)	No Perforation	(409)	No Perforation
750	A	286	2	(201)	No Perforation
	B	133	2	(255)	No Perforation
	C	62	4	(275)	No Perforation
	Iso-Crimp	(229)	No Perforation	*	*
1200	A	785	4	200	8
	B	764	4	165	8
	C	771	4	280	8
	Iso-Crimp	715	4	656	8
1800	A	1433	4	1264	8
	B	1486	4	1301	8
	C	1454	4	1309	8
	Iso-Crimp	1504	4	1492	8
2400	A	1900	4	1870	8
	B	2107	4	1986	8
	C	2114	4	1987	8
	Iso-Crimp	2139	4	2095	8
3000	A	2712	4	2643	8
	B	2721	4	2709	8
	C	2778	4	2703	8
	Iso-Crimp	2766	4	2772	8

() indicates rebound velocity, no perforation.

* indicates ballistic limit, zero residual velocity with complete perforation.

The energy-absorption results were plotted in conventional ballistic limit graphs (see figures 19 and 20) and percent projectile, kinetic energy graphs (see figures 21 and 22).

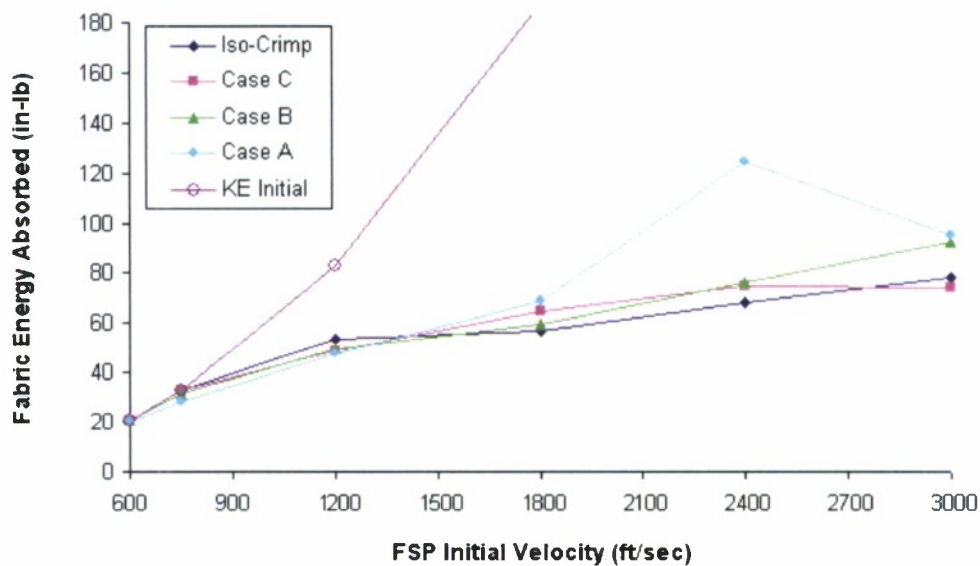


Figure 19. Ballistic Limit Curves for Normal Impacts, $\mu = 0.1$

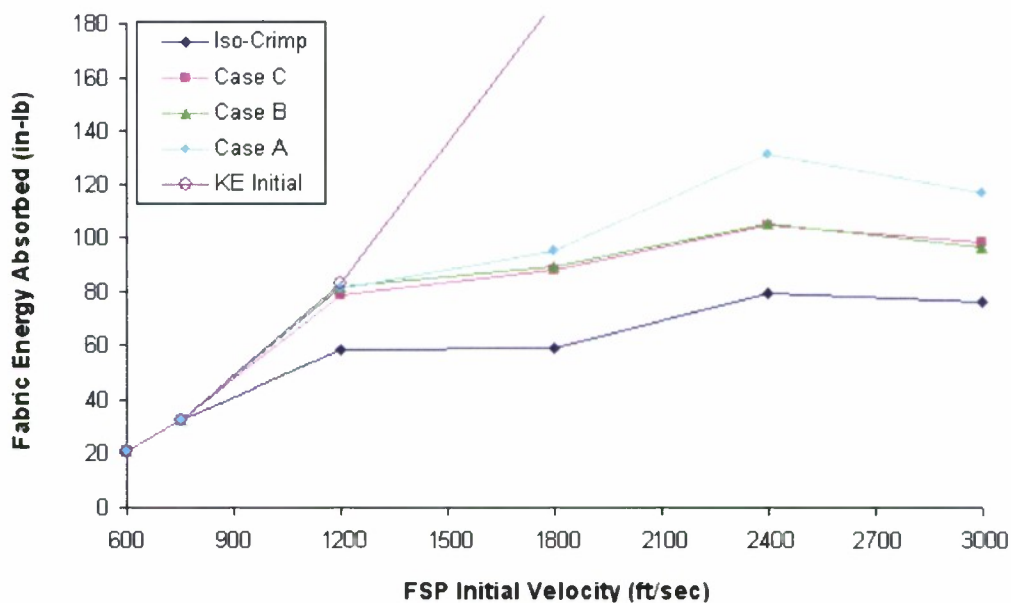


Figure 20. Ballistic Limit Curves for Normal Impacts, $\mu = 0.5$

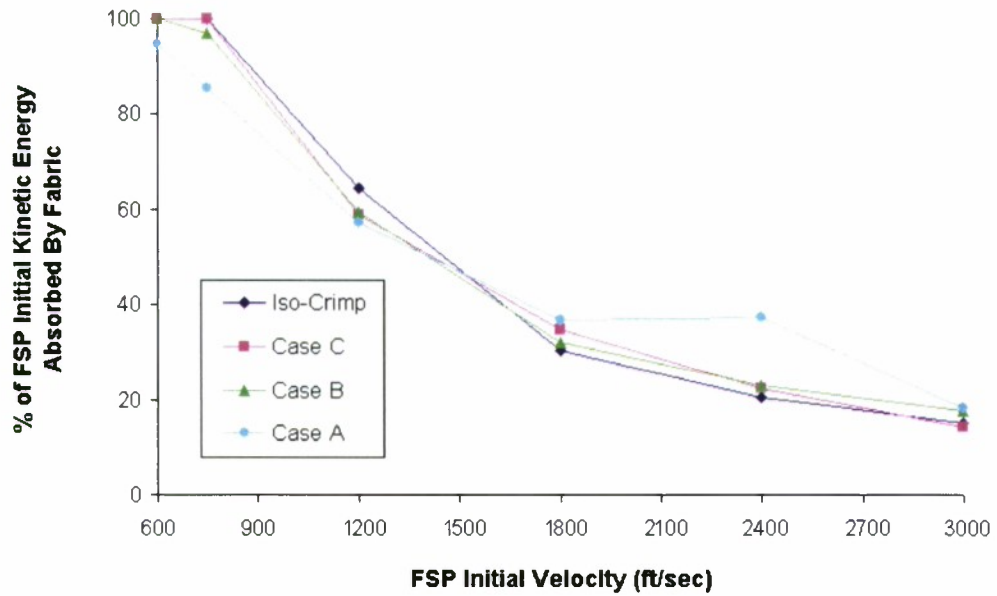


Figure 21. Percentage of FSP Initial Kinetic Energy Absorbed by Fabric for Normal Impacts, $\mu = 0.1$

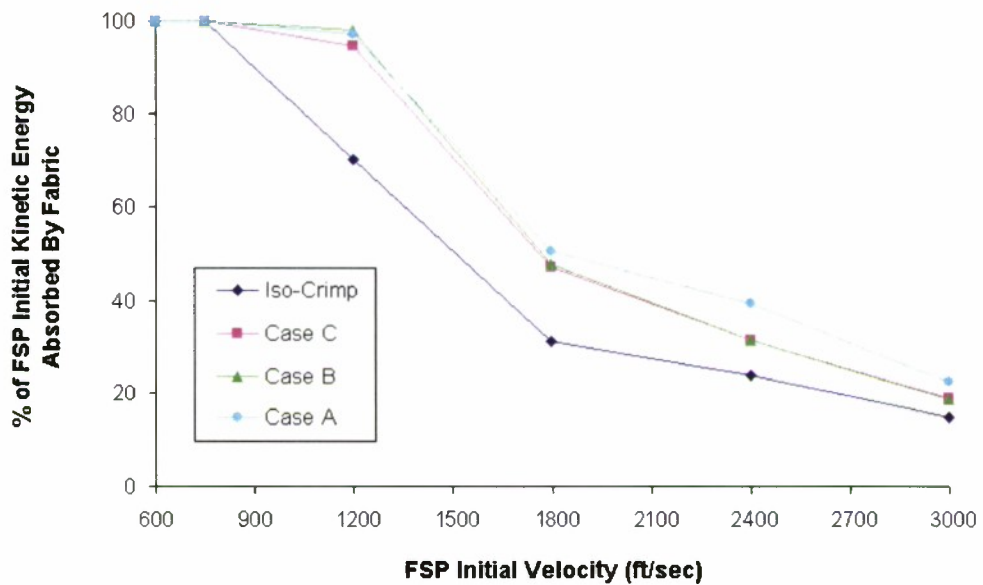


Figure 22. Percentage of FSP Initial Kinetic Energy Absorbed by Fabric for Normal Impacts, $\mu = 0.5$

The effects of crimp imbalance were mixed for the relatively low value of $\mu = 0.1$. First, a fully perforated failure occurred for case A without fracture of any of the primary yarns for $V_o = 600$ ft/sec. Here, the FSP penetrated the fabric by pure yarn migration as the interstices between yarns increased sufficiently, enabling the FSP to slip through the fabric. It was for this reason that the present research considered the smallest FSP size within the test series. No fully perforated failures occurred for the remaining crimp cases with $\mu = 0.1$ at $V_o = 600$ ft/sec. Furthermore, for $\mu = 0.1$ and $V_o = 600$ and 750 ft/sec, perforation-threshold velocities decreased with increasing crimp imbalance. The iso-crimp case provided the highest perforation velocity threshold of 1200 ft/sec. For $\mu = 0.1$ and $V_o \geq 1200$ ft/sec, the beneficial effects of crimp imbalance developed as reductions in $V_{residual}$ were achieved with increasing crimp imbalance. Only half the initial primary yarns, however, actively participated up to the time of full perforation; that is, $N_{fpy} = N_{py}/2$ for $V_o \geq 1200$ ft/sec. The iso-crimp case consistently produced the highest values of $V_{residual}$ for each V_o with $\mu = 0.5$.

Results also demonstrated that N_{fpy} increased with increasing values of FSP velocity and friction μ . Alternatively, N_{fpy} decreased with decreasing values of FSP velocity and μ . For relatively small values of μ , such as 0.1, the interfacial shear stresses provided very limited slip resistance. The lower this limit, the earlier the crossing yarns slipped and migrated away from the impact zone prior to achieving full perforation, thereby reducing N_{fpy} . This limited resistance produced a dwell time delaying the onset of primary yarn migrations. If V_o was sufficiently greater than the slip velocity of the crossing yarns, V_{scy} , then the time required by the FSP to perforate the fabric, t_{perf} , was less than the time that the crossing yarns required to slip, t_{slip} , and, furthermore, N_{fpy} increased with increasing V_o . Table 9 lists N_{fpy} , $V_{rebound}$, and $V_{residual}$ for both values of $\mu = 0.1$ and $\mu = 0.5$. Note that, for fully perforated failures with $\mu = 0.5$, $N_{fpy} = N_{py}$ which indicated that yarn migrations were negligible in each crimp case. An observation to the contrary occurred for $\mu = 0.1$ and $V_o = 600$ ft/sec, in which penetration occurred completely by yarn migration without any yarn fracture; that is, N_{fpy} was identically 0. The relationships between $V_{residual}$ and V_o for both values of μ were approximately linear. Furthermore, for these values of μ , the slopes of the curves in figures 13 and 14 were nearly identical. This provides a convenient method for interpolating single-ply energy absorptions for other values of V_o .

For $\mu = 0.5$, increases in crimp imbalance raised the perforation threshold velocities and significantly decreased $V_{residual}$ when compared to the iso-crimp case. The iso-crimp case consistently provided the highest values of $V_{residual}$ and the least amount of energy absorbed for all V_o 's leading to full perforation. At $V_o = 1200$ ft/sec, results suggest that the optimum crimp imbalance existed at case B. For the lower V_o velocities of 600 and 750 ft/sec, the fabric absorbed 100% of the FSP kinetic energies with no perforations. Yarn migrations and/or yarn fractures were not sufficient at these velocities to allow penetration. Although several primary yarns did fail at these velocities, the FSP was arrested. For fully perforating impacts, N_{fpy} remained constant at eight (sum of four LCC yarns and four HCC yarns) regardless of V_o . The influence of friction on N_{fpy} was highly significant: N_{fpy} increased by 200% as the coefficient of friction μ increased from 0.1 to 0.5.

A unique occurrence was observed for the iso-crimp case with $\mu = 0.5$ and $V_o = 750$ ft/sec. Here, the fabric experienced 100% fracturing of the primary yarns ($N_{fpy} = 8$, sum of four LCC yarns and four HCC yarns), yet the FSP was completely arrested (that is, $V_{residual} = 0$). This observation described a numerically predicted ballistic limit for this specific iso-crimp case.

The dominant failure mechanisms leading to full perforation differed depending on values of μ used. Fully perforated failures exhibited combined yarn migrations and fractures when $\mu = 0.1$. In contrast with $\mu = 0.5$, fully perforated failures were exclusively the result of plug-type fractures with negligible yarn migrations.

The effects of crimp imbalance shown in this research provided performance improvements similar to the effects of boundary conditions observed by Shockey et al.,²⁵ Duan et al.,²⁶ Duan et al.,²⁷ and Zeng et al.²⁹ These researchers noted that the fabric absorbed more energy and that greater impact loads developed with the use of two clamped edges rather than four clamped edges. These results were attributed to the fact that stress waves in the unclamped yarns do not reflect from their free ends back to the impact site. For the fully perforated, crimp-imbalanced cases with all yarn edges clamped, stress waves in the HCC yarns were delayed in time from reaching their boundaries and, if full perforation occurred prior to the reflected stress waves returning to the impact site, then the reflected waves did not influence the ballistic limit. Zeng et al.²⁹ further concluded that the limited slip phenomenon of using non-idealized clamped boundaries provided performance improvements similar to the two-clamped-edge versus four-clamped-edge models. Each of these modifications serves to delay the arrival of stress waves at the boundaries as well as their reflections along at least one yarn direction. The positive effects of these delays achieved greater energy absorption by the fabric. Furthermore, as projectile velocity increases, boundary conditions and model size have decreasing influence on the energy absorbed by the fabric. If stress waves reach the model boundaries after full perforation has occurred, then boundary conditions and model size do not influence the ballistic behavior. Similar stress-wave phenomena can also be achieved with hybrid fabrics constructed with different warp and weft yarn materials.³⁵

The ballistic limit curves shown in figure 20 for the case with $\mu = 0.5$ show that the fully perforated velocity thresholds were lowest for the iso-crimp case and notably greater with increasing crimp imbalance.

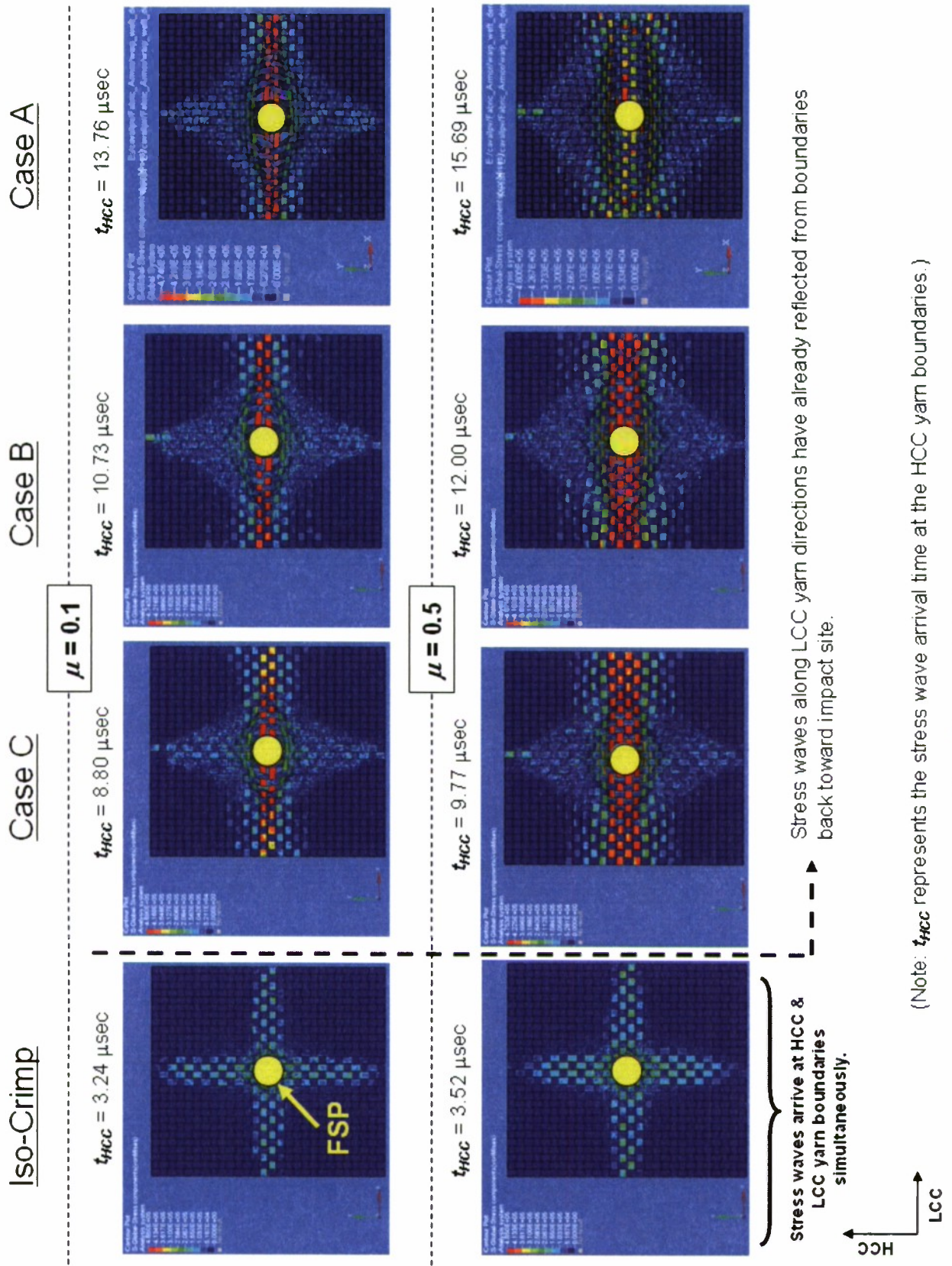
STRESS-WAVE RESULTS

The spatial and temporal influences of crimp imbalance on stress-wave propagations can be readily seen in the Von Mises stress plots shown in figure 23. Crimp imbalance delays the propagation of stress waves produced in the HCC yarns. Stress waves traveling along the LCC yarns reach a given radial distance away from the impact zone prior to the arrival of stress waves in the HCC yarns at the same distance. This sequence ensures that, if crossing yarns fail, the failures will not be simultaneous—thus providing the advantage of having critical primary yarns maintained in position as long as possible during the impact event. Note that while this time delay may be in the order of several to tens of microseconds, this advantage becomes critical during impact events in which the projectile fractures, producing multiple smaller sized fragments.

The plots in figure 23 reflect the approximate times the stress waves along the HCC yarn directions reach their boundaries. This time, designated t_{HCC} , increases with increasing crimp imbalance regardless of the value of μ . Furthermore, for crimp imbalance cases A, B, and C, the LCC yarns have already reflected their stress waves at their boundaries back to the impact zone prior to the stress waves in the HCC yarns reaching their boundaries.

A further assessment of the temporal effects achieved through crimp imbalance was made by monitoring the tensions in a pair of primary crossing yarns. Tensions were tracked at the clamped ends of the central-most HCC (warp) and LCC (weft) yarns at corresponding points A and B, respectively, as shown in figure A-1. The plots in figures A-2 through A-5 clearly demonstrate that increased crimp imbalance extends the arrival time of the transmitted force observed at the boundary of the central-most HCC yarn for a given V_o . Recall that the tenacity limit of the 1000-denier Vectran yarns was 28.0 gpd (corresponds to 59.7 lb); the peak tenacity values developed for each crimp case (V_o and μ) reached this limit.

When the tenacity limit (28 gpd) was reached, plasticity in the yarns began to develop and element failures subsequently followed at the tensile failure stress of 465 ksi. The plastic strain-energy time-history plots, described for the entire fabric (that is, not shown separately for the HCC and LCC yarn families) are shown in the energy plots of figures B-2 through B-7. The distribution of plastic strain energy between HCC and LCC yarn families increasingly dominates in the LCC yarns as crimp imbalance is increased. Total plastic strain energy in the fabric was shown to increase as the coefficient of friction increased. This result was not unexpected for the following reason: increased friction causes more primary yarns to remain in position, thus allowing more fractures of the primary yarns to occur and more energy to be absorbed by secondary yarns.



PRIMARY YARN MIGRATION, SLIP VELOCITY, AND MOBILITY

Deformation plots were used to compare the effects of weave construction, friction, and V_0 on yarn migrations occurring at the impact sites.* Figure 24 shows contour plots of primary yarn X-, Y-, and Z-displacements prior to perforation at identical times of $t = 10 \mu\text{sec}$. These plots reveal the local fabric deformations and slip magnitudes at the impact site and provide comparative views for addressing the influences of crimp imbalance and friction. Yarn migrations and interstitial sizes were noticeably greater with lower coefficient of friction. More primary yarns remained engaged with the FSP, and N_{fpy} was greater for the higher coefficient of friction (refer to table 9). Alternatively, as N_{fpy} decreased with decreasing friction, the interstitial regions expanded with decreasing friction; however, for either friction value used, N_{py} at time $t = 10 \mu\text{sec}$ and N_{fpy} on full perforation remained invariant with crimp imbalance. Table 10 lists the maximum normal (Z-axis) displacement of a primary yarn corresponding to $t = 10 \mu\text{sec}$ for each crimp case considered. The maximum normal yarn displacements increased with increasing crimp imbalance.

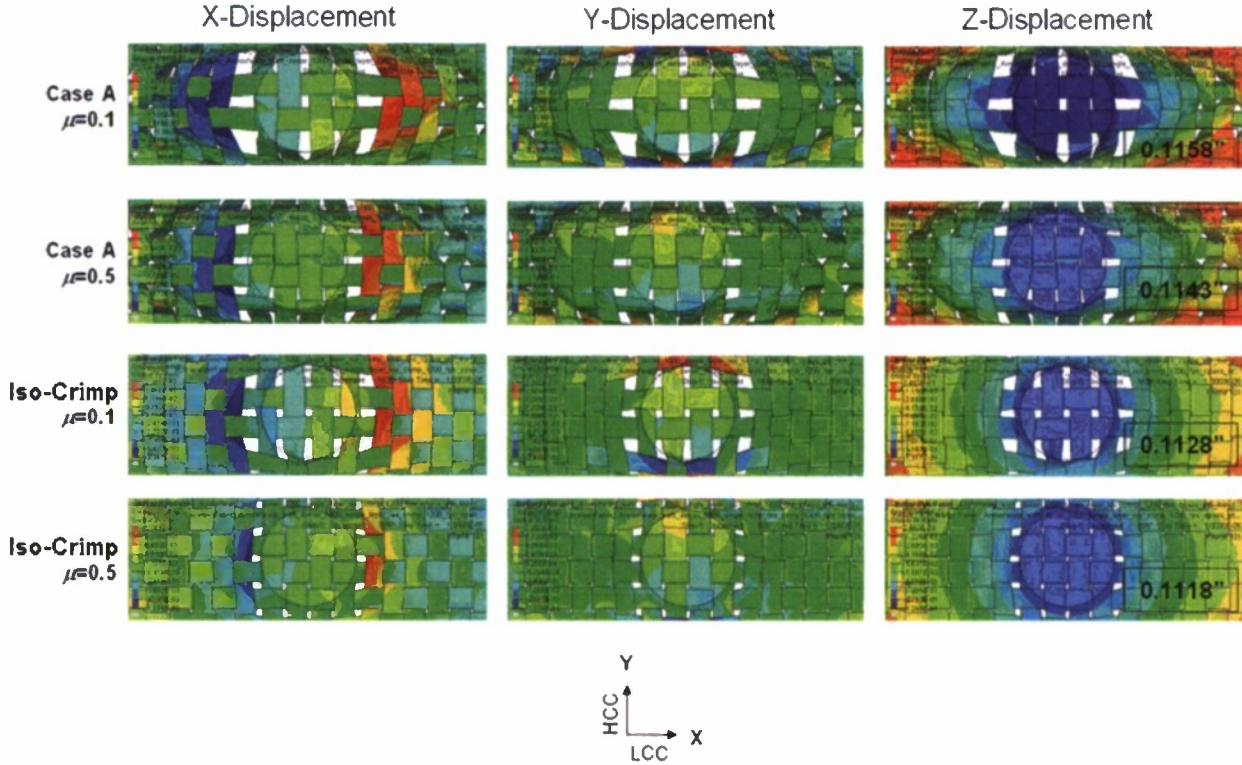


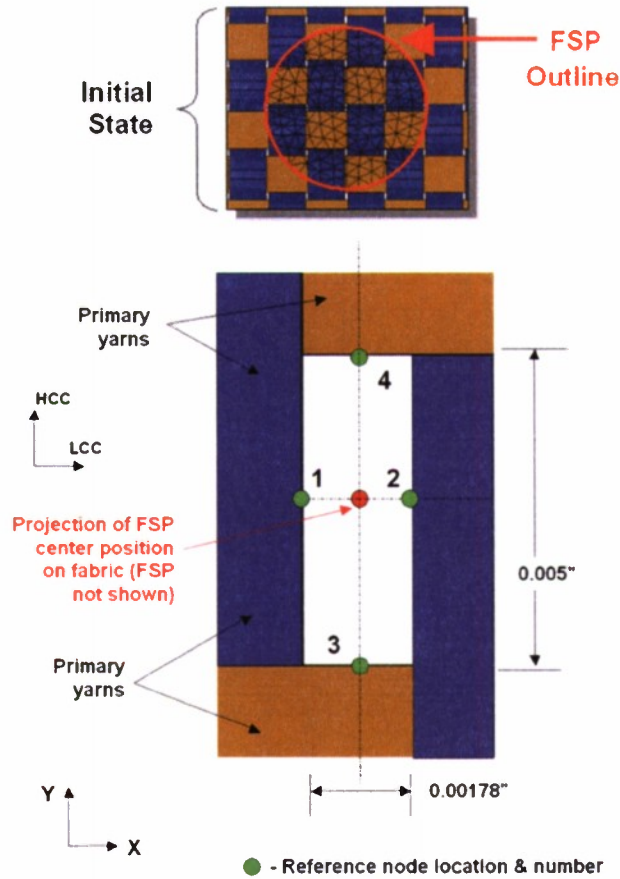
Figure 24. Primary Yarn Displacement Contours Shown for Normal Impacts with $V_0 = 1200 \text{ ft/sec}$ at $10 \mu\text{sec}$

* Note that migration refers to relative motions of primary yarns within the vicinity of the projectile (that is, nearfield) and that mobility refers to relative yarn motions remote from the projectile (that is, farfield). This distinction is important for understanding the effects of frictional energy dissipation.

Table 10. Peak Yarn Normal Displacements at $t = 10 \mu\text{sec}$

Crimp Case	Peak Yarn Z-Displacement (at $t = 10 \mu\text{sec}$) (in)	Comparison to ISO-Crimp Baseline (%)
A	0.1158	3.6
B	0.1143	2.2
C	0.1128	0.9
Iso-Crimp	0.1118	0.0

Yarn migrations were further investigated by characterizing the relative slip velocities among primary yarns. Here, only normal impacts of the extreme architectures were considered, namely, the iso-crimp case and case A, for $V_o = 1200 \text{ ft/sec}$. The primary yarn nodes shown in figure 25 were monitored; their relative in-plane component velocities are plotted in figure 26.



The primary yarn relative slip velocities along the X- and Y- axes are computed by:

$$V_{xslip} = V_{1x} - V_{2x}$$

$$V_{yslip} = V_{4y} - V_{3y}$$

Figure 25. Relative Slip Velocity Computations of Primary Yarns

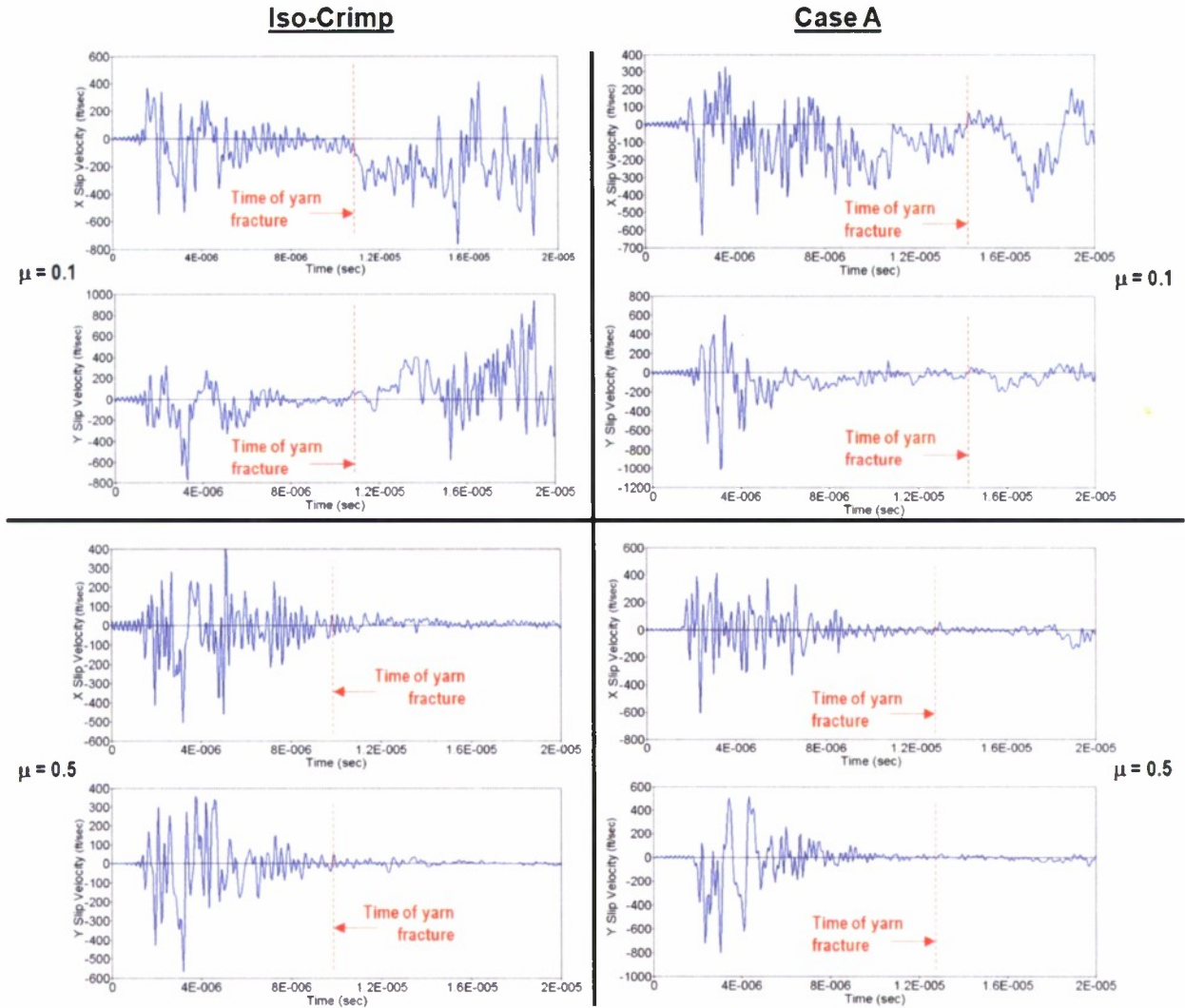


Figure 26. Time-History Plots: X- and Y-Velocity Components for Primary Yarn Tracked Nodes with $V_o = 1200$ ft/sec

Decreased friction and increased crimp imbalance were shown to increase the relative slip velocities at the tracked primary yarn nodes. (Note that the designated times at which yarn fractures occurred were approximate.) As expected, slip velocity components V_{xslip} and V_{yslip} were similar in magnitude within either iso-crimp model. For the crimp imbalance for case A, V_{yslip} was notably greater than V_{xslip} . The increased slip velocities and yarn mobilities of case A (in contrast to the iso-crimp case) contributed to the increased damping, frictional, and plastic strain energies (irrecoverable) of the fabric, as demonstrated in the energy time-history plots in figures B-2 through B-7 with increasing V_o . With the proper crimp imbalance and sufficient friction, energy absorptions by the fabric can be tailored for optimal performance.

45°/45° OBLIQUE IMPACT RESULTS

An oblique impact event was investigated to further explore the effects of crimp imbalance on energy absorption. The FSP shown in the biased orientation in figure 8 was chosen because of its ability to impart significantly greater shear and extensional jamming deformations to the fabric than those observed in normal impacts. Table 11 lists the velocity vector components as functions of V_o .

Table 11. Velocity Components Corresponding to 45°/45° Oblique Impacts

FSP Initial Velocity V_o	FSP Velocity Components (ft/sec)		
	V_x	V_y	V_z
600	300	300	424
750	375	375	530
1200	600	600	849
1800	900	900	1273
2400	1200	1200	1697
3000	1500	1500	2121

A key difference between normal and oblique impacts is the latter's ability to convert the initial translational kinetic energy of the FSP partly to rotational kinetic energy about the yaw, pitch, and roll axes. This conversion can increase the threshold penetration velocities by increasing the FSP's projected area on the target, thus increasing the number of primary yarns (N_{py}). This conversion, however, in part, makes the use of analytical methods difficult to employ for oblique impacts because the kinetic energy of the projectile is no longer completely translational but rather a mixture of translational and rotational components. Additionally, changes between the initial and residual velocity vector directions will generally occur.

The partial conversion of translational to rotational kinetic energies during oblique impact is greatly influenced by the highly nonlinear yarn deformations and migrations occurring within the target. The energy balance of equation (4), which was rewritten for perforating oblique impacts, requires that the rotational velocities of the FSP be described throughout the entire impact event. Fortunately, this is readily accomplished through the use of numerical FEA methods.

$$\frac{1}{2}mV_o^2 = \frac{1}{2}m(V_x^2 + V_y^2 + V_z^2)_f + \frac{1}{2}(I_x\omega_x^2 + I_y\omega_y^2 + I_z\omega_z^2)_f + E_{trans}, \quad (4)$$

where V_x , V_y , and V_z are the magnitudes of the translational velocity components; I_x , I_y , and I_z are the mass moments of inertia; ω_x , ω_y , and ω_z are the magnitudes of the rotational velocity components; and E_{trans} is the sum of the absorbed and dissipated fabric energies.

Figures 27 and 28 show deformation patterns for which the coefficient of friction values (μ) are equal to 0.1 and 0.5, respectively. Note that the patterns outlined in red indicate the presence of penetration failures resulting from yarn migrations and fractures. The FSP was fully arrested for those velocities corresponding to the images that are not outlined.

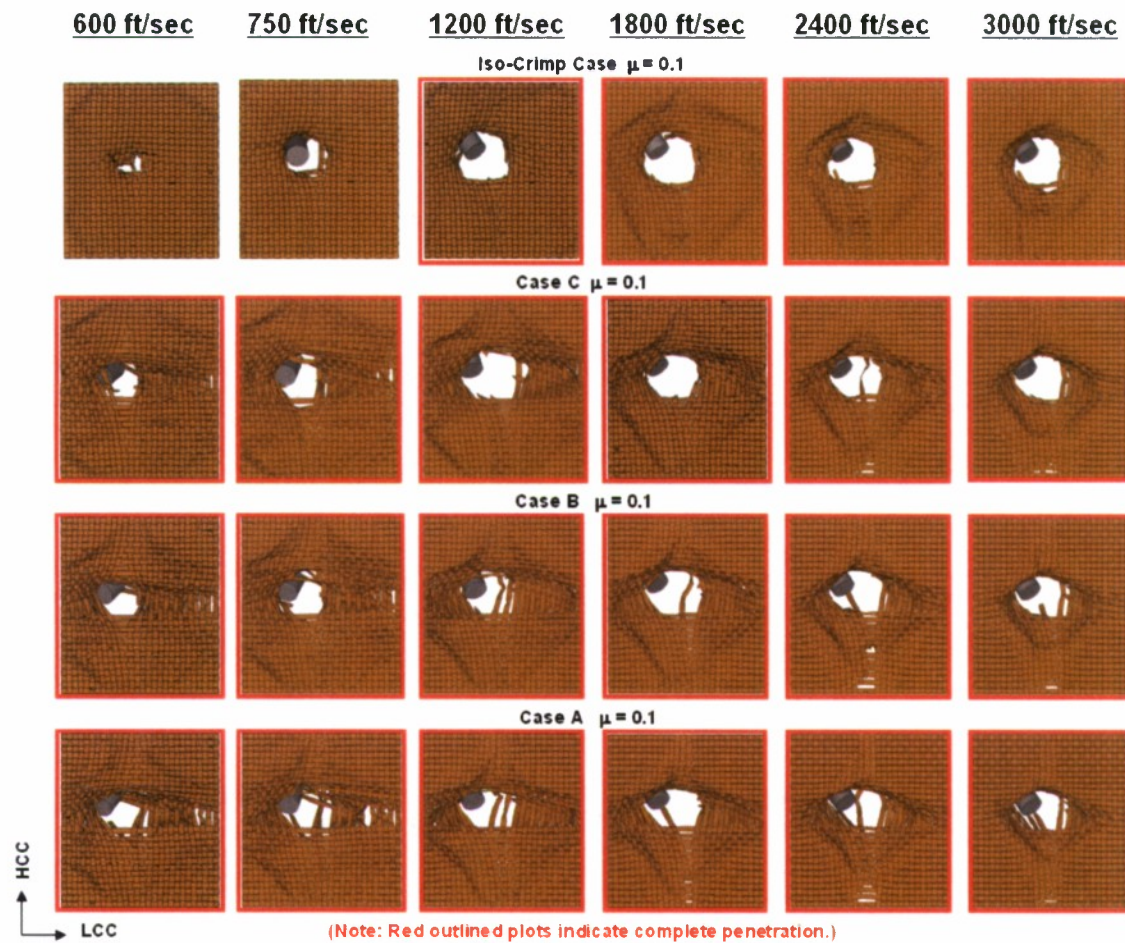


Figure 27. Oblique Impact Deformations for $\mu = 0.1$

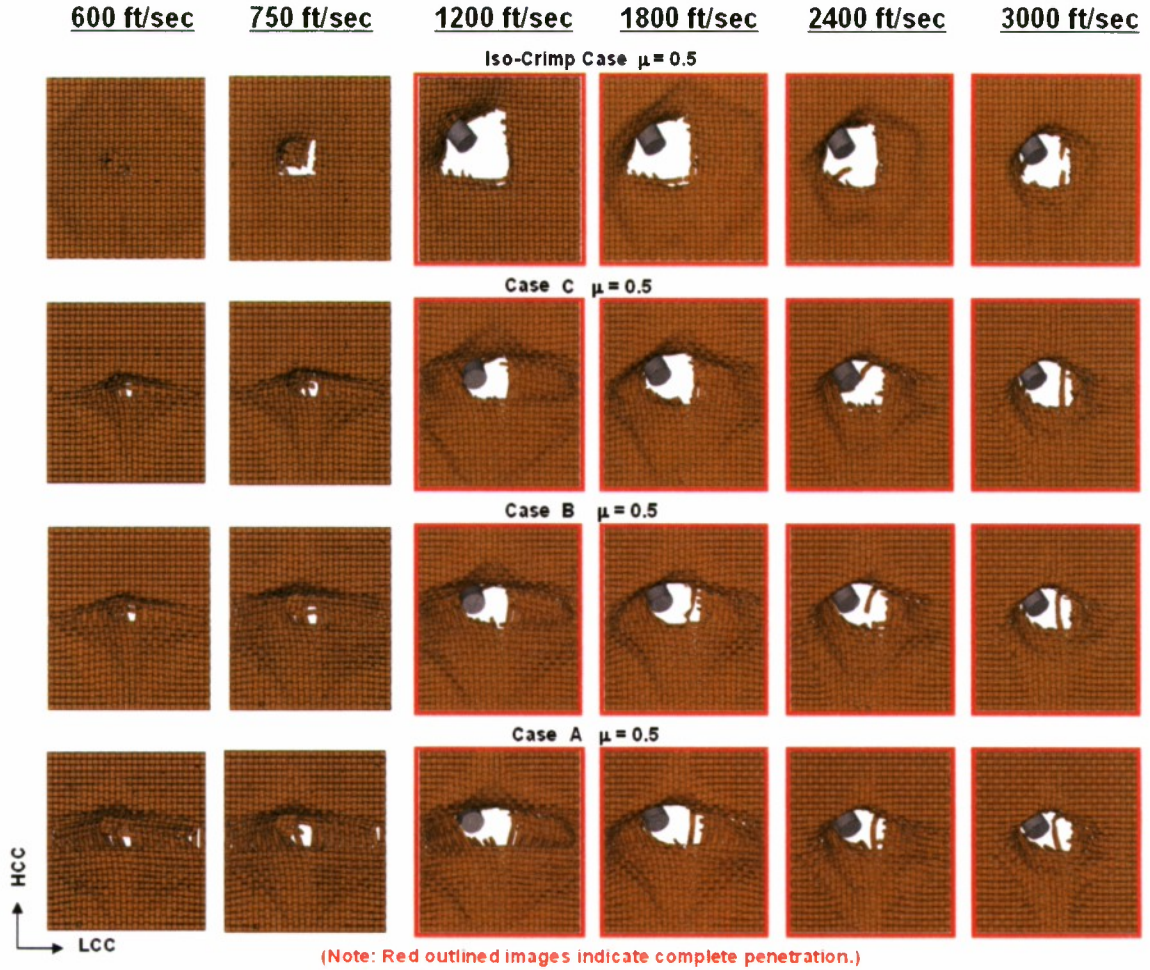


Figure 28. Oblique Impact Deformations for $\mu = 0.5$

Regions of shear and extensional jamming deformations were identified in the perforation patterns shown in figure 29 for $V_o = 1200$ ft/sec. Here, the influences of friction and crimp imbalance on perforation patterns are shown. Considering the iso-crimp fabric, perforation patterns for $V_o = 1200$ ft/sec were notably circular-like when $\mu = 0.1$ and were triangular when $\mu = 0.5$. Significantly greater shearing deformations, which were observed with decreasing yarn-yarn friction and increased crimp imbalance, served to blunt the damage zone; that is, the increased yarn mobility of the crimp-imbalanced case promoted migration of unbroken yarns toward the fracture fronts. The positive influence of the yarn mobilities resulted in a grouping or bundling effect, which locally reinforced the damage front—thus avoiding the sequential fracturing process of individual yarns observed with the iso-crimp architecture.

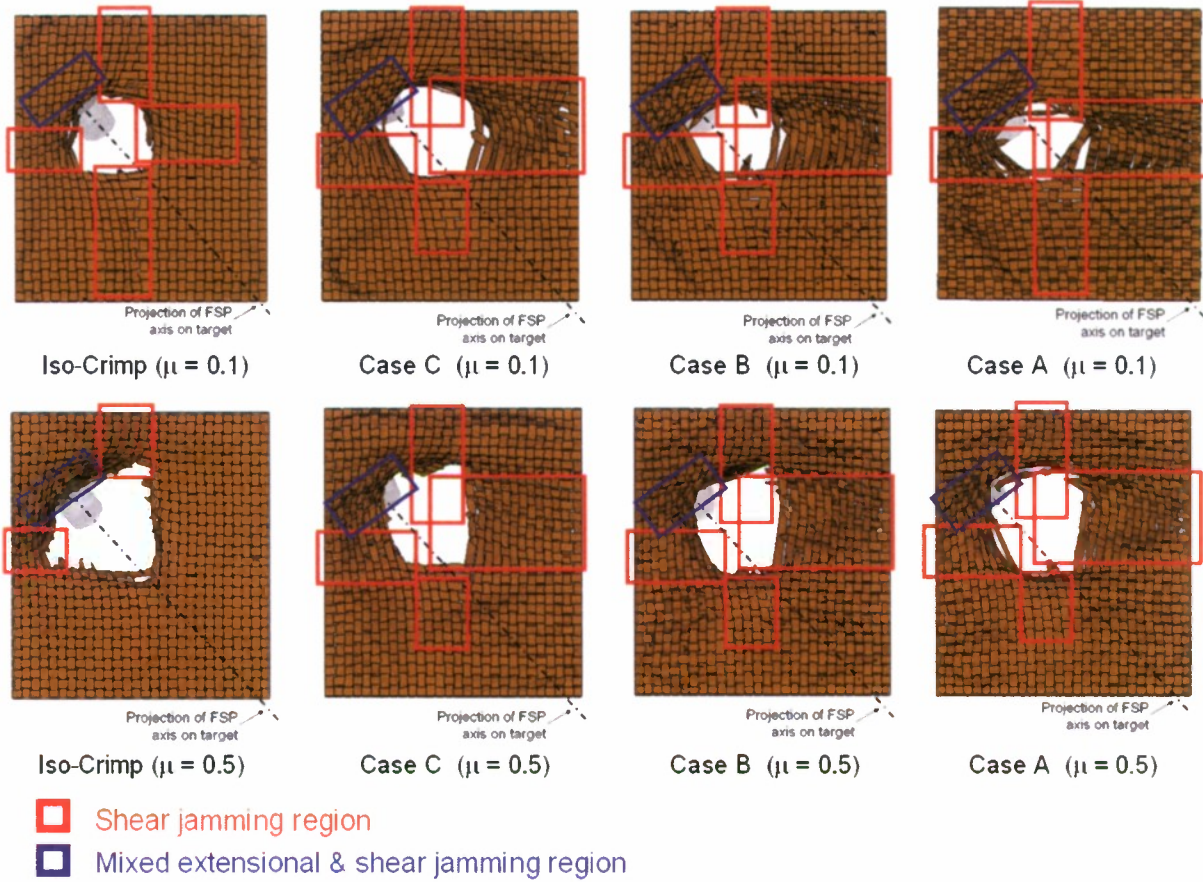


Figure 29. Shear and Extensional Jamming Regions with $V_o = 1200$ ft/sec and $\mu = 0.5$

Von Mises stress contours are shown in figures 30 and 31 for the extreme crimp cases considered, namely, the iso-crimp (figure 30) and case A crimp (figure 31) cases with $V_o = 1200$ ft/sec. The iso-crimp case with $\mu = 0.5$ exhibited a particularly noteworthy example of a progressive fracture mechanism. Figure 30 clearly suggests that a rip-stop fabric construction could blunt the damage zone and minimize successive yarn fractures. Stress waves in the wake of the FSP propagated and reflected from their boundaries prior to the arrival times of stress waves located ahead of the FSP. The peak Von Mises stresses consistently occurred along the regions dominated by shear jamming deformations. The total number of failed yarns (primary and secondary) $N_{fytotal}$ was 24.

Results of case A, with $\mu = 0.5$ and $V_o = 1200$ ft/sec, revealed that $N_{fytotal}$ was equal to 12 (sum of 8 LCC and 4 HCC yarns). Comparison of these two crimp cases showed that a 20- μ sec delay was produced in the arrival time of HCC stress waves for case A.

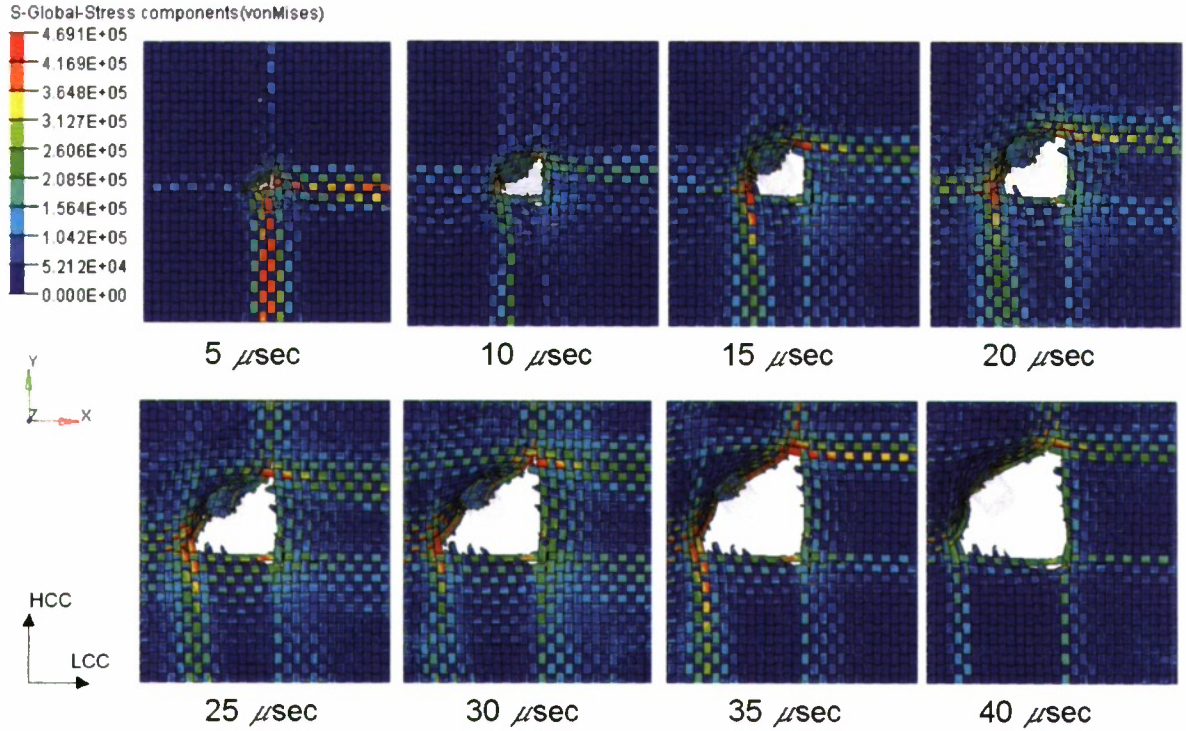


Figure 30. Von Mises Stress Plots Demonstrating Progressive Yarn Fractures (Iso Crimp Case with $V_o = 1200$ ft/sec and $\mu = 0.5$)

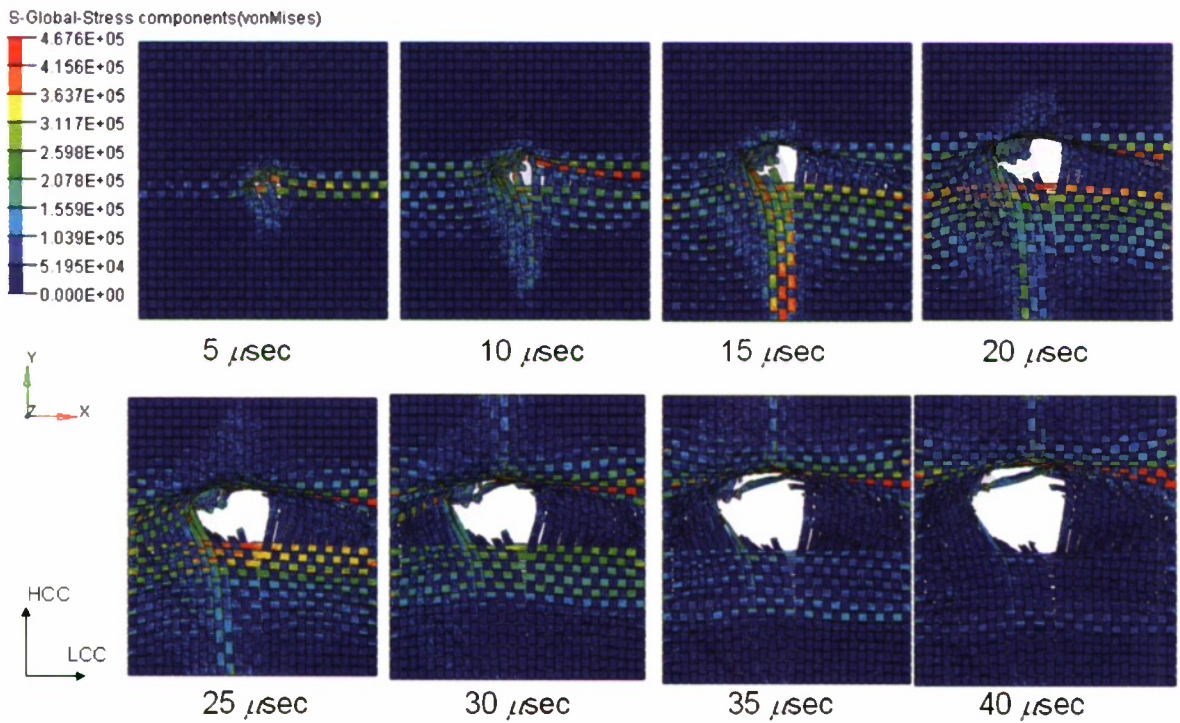


Figure 31. Von Mises Stress Plots for Case A with $V_o = 1200$ ft/sec and $\mu = 0.5$

The ability of the fabric targets to impart rigid body rotations to the FSP is a positive mechanism that can enhance protection against oblique impacts. Here, only some of the translational kinetic energy is converted to rotational kinetic energy primarily due to the formation of rotational velocities about the pitch and yaw axes. Furthermore, these rotations serve to increase the projected area of the FSP on the targets to the extent that the number of primary yarns may increase. The FSP rigid body rotations (1) increased with decreasing V_o , (2) increased with increased coefficient of friction, and (3) increased with increased crimp imbalance when $V_o > 1800$ ft/sec. This ability was confirmed by the resultant rotational velocity time-histories shown in figure 32.

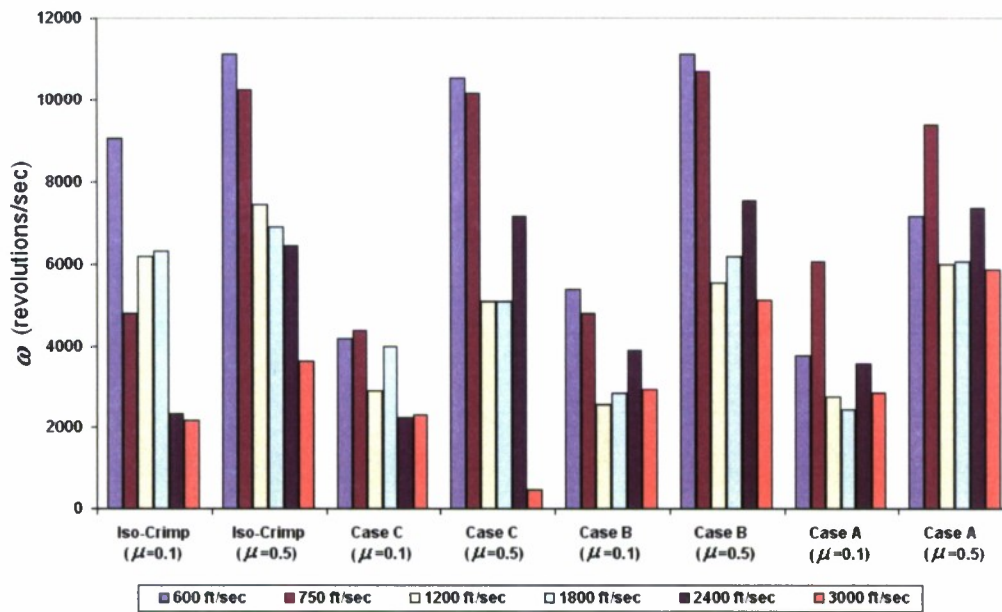


Figure 32. Peak Magnitudes of FSP Resultant Rotational Velocities for 45°/45° Oblique Impacts

Energy absorption results for the 45°/45° oblique impacts are shown in table 12 for a fixed LCC (weft) yarn crimp content of 1.2%. The results were notably dependent on the specific coefficient of friction used. For the iso-crimp case and $V_o = 1200$ ft/sec, 42% more energy was absorbed by the fabric when $\mu = 0.5$ in contrast to when $\mu = 0.1$. This result was expected because the higher coefficient of friction produced a greater number of yarn fractures. For $\mu = 0.1$, the absorbed energies of the crimp imbalanced architectures exceeded those obtained from the iso-crimp case only when $V_o > 1200$ ft/sec. Energy absorptions for fully perforating impacts with $\mu = 0.5$ continually increased with increasing crimp imbalance. The iso-crimp case provided the minimum energy absorption regardless of V_o . For $V_o = 3000$ ft/sec and $\mu = 0.5$, a 34.4% increase in energy absorption was achieved with case A in comparison to the iso-crimp case. The advantages achieved through increased crimp imbalance in the oblique impact event are qualitatively consistent with those observed in the normal impact event for $\mu = 0.5$.

Table 12. Fabric Absorbed Energies for 45°/45° Oblique Impacts with Fixed LCC (Weft) Yarn Crimp Content of 1.2%

		Energy Absorbed by Fabric with $\mu = 0.1$			
V_o (ft/sec)	$KE_{Initial}$ (in-lb)	Iso-Crimp (in-lb)	Case C (in-lb)	Case B (in-lb)	Case A (in-lb)
600	20.83	<u>20.83</u>	19.16	17.80	17.78
750	32.54	<u>32.54</u>	29.82	26.69	25.34
1200	83.31	57.39	52.47	40.98	39.60
1800	187.44	71.08	73.98	57.97	65.09
2400	333.23	70.89	73.30	98.47	88.02
3000	520.67	87.66	92.75	97.56	111.18
		Energy Absorbed by Fabric with $\mu = 0.5$			
V_o (ft/sec)	$KE_{Initial}$ (in-lb)	Iso-Crimp (in-lb)	Case C (in-lb)	Case B (in-lb)	Case A (in-lb)
600	20.83	<u>20.83</u>	<u>20.83</u>	<u>20.83</u>	<u>20.83</u>
750	32.54	<u>32.54</u>	<u>32.54</u>	<u>32.54</u>	<u>32.54</u>
1200	83.31	81.66	79.54	80.48	81.89
1800	187.44	113.84	115.02	110.24	120.30
2400	333.23	127.34	135.28	137.44	138.55
3000	520.67	107.88	118.91	125.54	145.05

X indicates that no complete penetration occurred.

X indicates the result at the time of complete penetration.

For non-penetrating impacts, recoverable energy E_{rf} is plotted in figures 33 and 34 for $\mu = 0.1$ and $\mu = 0.5$, respectively. The recoverable energy represents the rebound energy that performs work on the projectile after arrest.

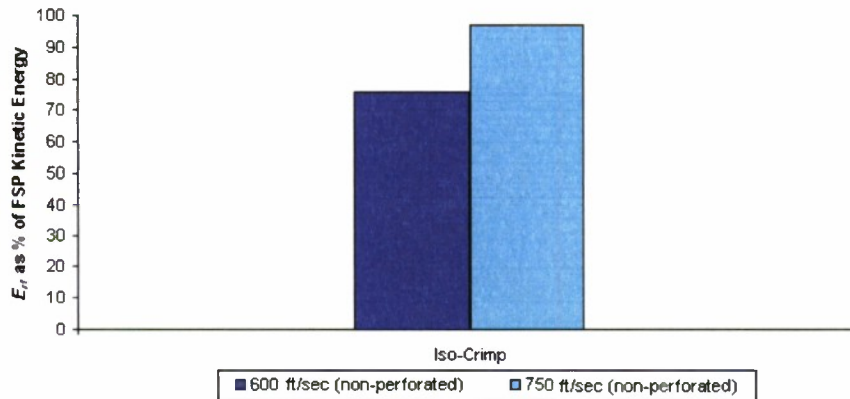


Figure 33. E_{rf} As a Percentage of FSP Kinetic Energy for Non-Through Penetrating 45°/45° Oblique Impacts ($\mu = 0.1$)

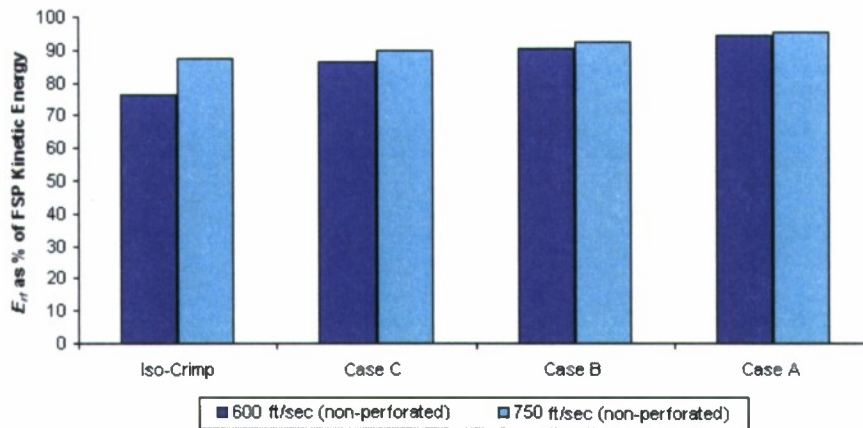


Figure 34. E_r As a Percentage of FSP Kinetic Energy for Non-Through Penetrating 45°/45° Oblique Impacts ($\mu = 0.5$)

The 45°/45° oblique impacts produced yarn fractures not only at the impact sites but also along the clamped ends. Figures C-1 through C-6 revealed the yarn fracture locations as functions of crimp case, μ , and V_o . Note that these plots are shown in the undeformed state, that is, fabric deformations were turned off for clarity. Yarn end fractures were shown to increase with increasing crimp imbalance, while no end fractures developed for the iso-crimp architecture regardless of the values chosen for V_o and μ . End fractures resulted from the increased stress magnitudes associated with reflected stress waves at the clamped boundaries and were more prevalent with relatively lower friction (that is, $\mu = 0.1$ versus 0.5). This result clearly established that crimp imbalance enabled more energy that was absorbed by the fabric to be distributed farther away from the impact site than did the iso-crimp architecture. Multiple fractures were identified along individual yarns and were generally confined to the impact site. A further review of the stress contour plots confirmed that these multiple fractures occurred within the primary yarns because of the cutting action developed by contact along the projectile's circumference.

Yarn fracture totals and distributions among LCC and HCC yarn families are summarized in table 13. Yarn fracture totals generally increased with decreasing crimp imbalance for the oblique fully perforating impacts regardless of what friction coefficient was used. Fracture totals for the warp and weft yarns of the iso-crimp architecture matched reasonably well for each FSP initial velocity V_o . (Recall that the warp and weft directions were aligned along the HCC and LCC directions, respectively.) Yarn fractures in the crimp-imbalanced architectures, however, were generally dominant along the LCC versus HCC yarn direction. This result was expected because of the delayed stress-wave effect incorporated by the HCC yarns. Consider now the results corresponding to 0.5-coefficient of friction. Yarn fracture totals were maximized at $V_o = 2400$ ft/sec—the velocity at which the peak ballistic limit values were achieved. For $V_o > 2400$ ft/sec, yarn fractures decreased as did the energies absorbed by the fabric.

Table 13. Fractured Yarn Counts for 45°/45° Oblique Impacts with Fixed LCC (Weft) Yarn Crimp Content of 1.2%

45°/45° Oblique Impact Event							
FSP Initial Velocity V_o (ft/sec)	Crimp Case	$\mu = 0.1$			$\mu = 0.5$		
		LCC N_{fy}	HCC N_{fy}	Total N_{fy}	LCC N_{fy}	HCC N_{fy}	Total N_{fy}
600	A	2	1	3	4	0	4
	B	3	0	3	5	0	5
	C	3	1	4	4	0	4
	Iso-Crimp	0	0	0	0	1	1
750	A	3	1	4	5	0	5
	B	3	1	4	5	0	5
	C	4	1	5	5	4	9
	Iso-Crimp	3	5	8	6	6	12
1200	A	3	1	4	8	4	12
	B	4	1	5	10	4	14
	C	5	3	8	9	5	14
	Iso-Crimp	6	7	13	10	10	20
1800	A	4	4	8	12	4	16
	B	4	3	7	11	4	15
	C	6	3	9	13	6	19
	Iso-Crimp	5	7	12	12	13	25
2400	A	4	3	7	13	4	17
	B	7	3	10	13	5	18
	C	3	3	6	13	7	20
	Iso-Crimp	3	6	9	13	13	26
3000	A	5	3	8	9	4	13
	B	4	3	7	9	4	13
	C	4	4	8	8	5	13
	Iso-Crimp	5	7	12	8	10	18

X indicates that no complete penetration occurred.

X indicates that complete penetration occurred.

Penetration velocity thresholds increased significantly from approximately 600 ft/sec to 1100 ft/sec as the coefficient of friction μ was increased from 0.1 to 0.5, respectively (see figures 35 and 36). For $V_o > 1200$ ft/sec, however, increased energy-absorption levels were achieved with the crimp-imbalanced architectures in contrast to the iso-crimp construction.

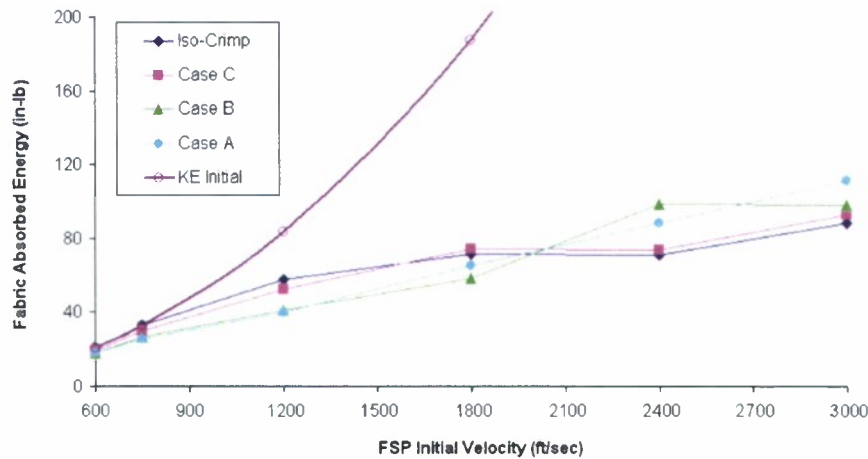


Figure 35. Ballistic Limit Curves for 45°/45° Oblique Impact Event with $\mu = 0.1$

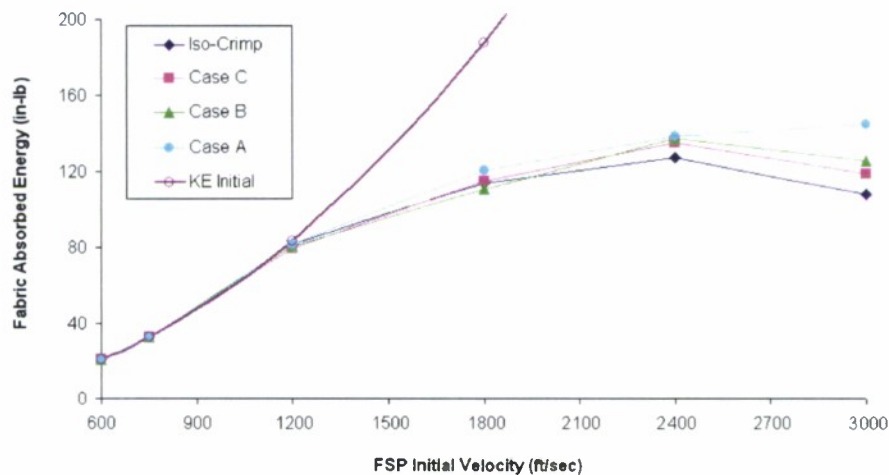


Figure 36. Ballistic Limit Curves for 45°/45° Oblique Impact Event with $\mu = 0.5$

The results appear to be contradictory from a cursory perspective. The following explanation clarifies how greater energy absorption can be achieved with fewer yarn fractures. First, crimp imbalance in time decouples the stress waves propagating along the LCC and HCC yarns, as was demonstrated by the string model example. By controllably delaying these propagations, the LCC yarns transferred more energy outward from the impact site while the HCC yarns minimized reflected stress-wave energies associated with the yarn crossover points. (Additionally, the delayed stress waves also extended the presence of active HCC crossing yarns in regions where LCC yarns previously failed, which provides further protection against possible penetration by fragments resulting from projectile fractures upon target impact.)

Second, viscous damping, frictional, plastic dissipation energies, and fabric kinetic energies increased with increasing crimp imbalance and V_o as shown in figures D-2 and D-3. The iso-crimp case consistently provided less viscous damping energy regardless of V_o and μ , and, for fully perforating impacts, the iso-crimp case generally provided the least fabric kinetic energy, as shown in figures D-2 and D-3. The elastic and plastic strain energies produced in the yarns were minimally affected by friction coefficient and crimp imbalance at the times at which complete target penetration occurred as indicated in figures D-2 and D-3. The viscous damping and frictional (irrecoverable) energies and fabric kinetic (recoverable) energies provided the key energy-transfer mechanisms that enabled crimp imbalance to increase the energy absorbability of the fabric.

The deformation patterns shown in figure 29 correspond to $V_o = 1200$ ft/sec and were captured at nearly the same relative projectile position on perforation, which was necessary to establish a basis for comparing the amounts of fabric shearing motions. Consider now the iso-crimp case with $\mu = 0.5$. It is readily apparent that shearing deformations in the wake of the projectile were substantially smaller with increased friction and decreased crimp imbalance. The fabric region ahead of the projectile transitioned to a blunting zone of approximately 180° in which extensive shear jamming was produced. All yarns within the wake, however, completely fractured and provided no additional energy absorption. Yarn fractures occurred locally at each end of the blunting zone, resulting in a sequential fracture mechanism for both yarn families as clearly observed in the Von Mises stress plots of figure 30. Further energy absorption was primarily achieved through successive fractures of individual yarns of both families. Viscous damping energy was greatly reduced because fabric shearing and yarn slip were relatively restricted. No yarn fractures were observed at the clamped boundaries, which suggested that stress-wave reflections at the yarn crossover points limited both the transfer of energy away from the impact site and the spatial distribution of yarn fractures.

Consider now the deformation patterns of the crimp imbalanced architectures. The number of fractured HCC yarns within the wake of the projectile was substantially less than that of the iso-crimp case. Because the fabric shearing motions forced the HCC yarns to migrate away from the projectile, greater shearing deformations developed and the blunting zone extended not only ahead of the projectile but also within the wake. The additional energy required to expand the size of the blunting zone was responsible for the increase in viscous damping, frictional, and kinetic energies, which increased with increasing crimp imbalance. It appears, therefore, that optimizing the dynamic energy absorbability of woven fabrics for ballistic and fragment impacts involves maximizing the performance of the damping and frictional dissipation energies and kinetic energy of the fabric as previously indicated. Crimp imbalance is one method that can achieve this maximization.

CONCLUSIONS

The concept of crimp imbalance for use as an architectural mechanism to increase the ballistic energy-absorption capacity of plain-woven, single-ply Vectran fabrics was described and numerically evaluated. A wide range of model parameters was exercised: (1) one crimp-balanced and three crimp-imbalanced woven architectures, (2) six FSP initial velocities, (3) two friction cases, and (4) two angles of incidence (normal and oblique). All crimp cases used a fixed 1.2% crimp content along the LCC (weft) yarn direction and the same geometric cover factor of 99.56%—a value considered excessive for ballistic protection but appropriate for stab protection. Recalling that cover factors for ballistic protection are generally required to be smaller than those required for stab resistance so as to not restrict yarn mobilities, the excessive geometric cover factor used in the present research was intentional to provide lower-bound values of the increased ballistic energy absorptions achieved through crimp imbalance. The selected 45°/45° oblique impact event was chosen because of its preclusivity for generating relatively high levels of shearing deformations resulting from the in-plane velocity component aligned to the target's maximum bias angle. Solutions were obtained using the ABAQUS³³ explicit finite element solver, and discretization of each yarn was directly performed. The obtained solutions fully supported the kinematic interactions between yarns and projectile, friction at all contact surfaces, nonlinear large deformations, element tensile failures, and elastic-plastic constitutive behaviors of the yarns. For non-perforating impacts, the recoverable energies were computed, and, for perforating impacts, the residual energies and exit velocities were obtained. The effects of crimp imbalance and friction coefficient on primary yarn migrations, primary yarn fractures, and perforation patterns were established.

Crimp imbalance was shown to provide greater energy absorptions for both normal and oblique impacts with two-grain FSP projectiles, particularly when higher friction coefficients were present for yarn-yarn and yarn-projectile contacts (that is, $\mu = 0.5$ versus $\mu = 0.1$). For normal impacts, the optimal crimp imbalance case considered provided a 61% increase in energy absorption for $V_o = 1800$ ft/sec and $\mu = 0.5$ in contrast to the iso-crimp (baseline) construction at the same velocity. The findings suggest that for specific threats (that is, projectile types and velocities), there exist preferable levels of crimp imbalance that can be used to maximize energy-absorption levels and possibly increase perforation threshold velocities. The normal impact ballistic limit curves shown in figure 20 for the case with $\mu = 0.5$ indicated that the perforation-velocity thresholds were lowest for the iso-crimp case and notably greater with increasing crimp imbalance.

Increases in friction coefficients were shown to maximize the number of primary yarns, one of several key factors for increasing ballistic energy absorption. When lower coefficients of friction were employed (that is, $\mu = 0.1$) in the oblique impacts, the advantages of crimp imbalance were delayed and realized for only $V_o \geq 1800$ ft/sec. The benefits of crimp imbalance for $V_o < 1800$ ft/sec were masked by the extent of primary yarn migrations that occurred with lower friction at the yarn-yarn and yarn-projectile interfaces. Substantial yarn migrations occurred away from the impact zone, thus significantly reducing the number of primary yarn fractures. For higher coefficients of friction (that is, $\mu = 0.5$), the advantages of crimp imbalance in the oblique impacts were immediately achieved for all values of V_o beyond the ballistic limit.

Energy absorption results for normal and oblique impacts do not easily scale for single-layer, woven fabrics—especially when yarn-projectile and yarn-yarn friction are relatively low. Difficulties arise from kinematic mechanisms such as yarn-yarn slip, yarn-projectile slip, fabric shearing, and crimp interchange. These mechanisms dictate the number of primary yarns that remain actively engaged throughout the impact event leading up to the ballistic limit and beyond. Similarly, these mechanisms make it difficult to correlate single-layer ballistic performance to static yarn pullout tests.

Crimp imbalance was shown to delay the propagation of stress waves along the HCC yarn direction. The delay provided an increased level of semitransparency of stress waves at the crossover regions, resulting in the rate at which energy propagated outward from the impact site increased along the LCC yarns. In contrast, the crimp-balanced architecture reflected more stress-wave energy from the crossover regions back to the impact site. These crossover reflections negatively affected the ballistic protection levels by decreasing the absorbed fabric energies for fully perforating impacts. The normal and 45°/45° oblique impacts produced yarn fractures occurring not only at the impact sites but also along the clamped yarn ends. End fractures resulted from the increased stress magnitudes associated with reflected stress waves at the yarn boundaries. The number of end fractures increased with increasing crimp imbalance. No end fractures were observed in any of the iso-crimp models, thus confirming that crimp imbalance minimizes crossover reflections and promotes further energy transfer away from the impact site. Additionally, multiple fractures were observed along individual yarns due to cutting action produced between primary yarns and the leading circumferential edge of the FSP. A key benefit of delayed stress waves was the extended presence of active HCC crossing yarns in regions where LCC yarns previously failed. The extended presence of active HCC yarns further protects against penetration by fragments resulting from projectile fractures upon target impact.

Peak energy-absorption capacities were obtained when the viscous damping and frictional dissipation (that is, increasing crimp interchange, yarn slip, and rotation) and fabric kinetic energies were maximized. Viscous damping and frictional energies were maximized for a given architecture and friction coefficient once the shear jamming and extensional jamming states were achieved around the impact site. Crimp interchange, yarn slip, and fabric shearing were the key deformation mechanisms for enabling the jamming states to develop. Crimp-imbalanced architectures further enabled these deformation mechanisms, thus increasing the energy-absorption capacities of the fabrics.

Weaving methods for imparting the desired crimp contents among yarn directions are generally process driven. Yarn tensions and shuttle velocities are the key weaving parameters that control crimp distributions among yarn families. Crimp imbalance can be readily achieved in current weaving processes and, when coupled with appropriate fiber-sizing methods, can also increase yarn-yarn friction if necessary. Additional methods, such as the use of temporary yarn coatings, can be used to geometrically lock in the desired crimp distributions. The coating thickness dictates the amount of additional crimp content produced in the fabric and is removed postweaving by solvent wash or other appropriate process. This method may be simultaneously performed with yarn-sizing operations to increase overall processing efficiencies.

Results of the single-ply models indicate that deviations in crimp contents can have pronounced effects on energy absorptions and projectile residual velocities. Accordingly, it is recommended that crimp contents be specified as design parameters for soft, woven armors. Furthermore, it is recommended that crimp contents be monitored and controlled during manufacturing and that quality assurance testing be conducted on the finished product to ensure that crimp contents are within prescribed tolerances.

Yarn mobility is a critical mechanism for enhancing ballistic energy absorption in woven fabrics. If yarn mobility is restricted, ballistic energy absorption can decrease leading to premature fractures of the primary yarns. Furthermore, yarn mobility is responsible for the blunting effect observed along the damage fronts of oblique impacts. Blunting was shown to be a particularly beneficial reinforcing mechanism. When sufficient yarn mobility exists, fabric damping and frictional dissipation energies and yarn kinetic energy mechanisms become substantial. These specific energy mechanisms allow crimp-imbalanced fabrics to outperform their crimp-balanced counterparts as evidenced by these results. This important observation further suggests that crimp imbalance can also be used to increase the ballistic energy absorption in highly dense fabrics designed for stab protection.

The normal impact results may also provide useful insights for understanding the mechanics of stab impacts on woven targets. Recalling the observed dependence of N_{fpy} on μ and V_o , stab impacts from, for example, awls, needles, and knives will involve penetrator velocities significantly smaller than the ballistic values considered here. Therefore, yarn mobilities will expectedly increase with increasing values of t_{perf} (that is, $t_{slip} < t_{perf}$) for a given stab threat. To counter stab threats, stab resistant woven textiles require (1) high cover factors (that is, dense weave constructions), (2) twisted yarns to prevent filament migration within the yarns, (3) high yarn-to-yarn coefficients of friction, and (4) extensional and shear jamming states that are reached with only minimum fabric distortion. Once these criteria are met, such stab threats must fail the fabric by cutting of the yarns or filament migration within the yarns to allow puncturing. The crimp imbalanced fabric architectures of the current research have the capacity to synergistically increase both the ballistic and stab protections levels simultaneously. This is achieved through the combined use of crimp imbalance and high cover factors. Cover factors for ballistic protection are generally required to be smaller than those required for stab resistance.

Future research tasks include (1) ballistic testing of crimp-imbalanced, single-ply fabrics for model validation purposes, (2) expansion to other fixed LCC (weft) crimp values, (3) development of plain-woven, crimp-imbalanced, multi-ply numerical models to establish the coupled system effects from layer-to-layer contact on deflection and stress wave propagations and (4) the influence of crimp imbalance on energy absorption of bi-plain triaxial and leno weave fabric architectures.

REFERENCES

1. “Ballistic Resistance of Body Armor,” NIJ Standard-0101.06, National Institute of Justice, July 2008.
2. “Ballistic Test Method for Personal Armour Materials and Combat Clothing,” NATO Standardization Agreement (STANAG) 2920, Edition 2, North Atlantic Treaty Organization, 31 July 2003.
3. “Pinnacle Armor,” <http://www.pinnaclearmor.com>.
4. P. Cunniff, M. Auerbach, E. Vetter, and D. Sikkema, “High Performance “M5” Fiber for Ballistics/Structural Composites,” <http://web.mit.edu/course/3/3.91/www/slides/cunniff.pdf>.
5. Paul Cavallaro, private communications with Charles Howland, Warwick Mills, New Ipswich, NH, June 2008.
6. X. Chen and I. Chaudhry, *Ballistic Protection, Textiles for Protection*, R. Scott, ed. Woodhead Publishing Co., 2005.
7. A. Tabiei and G. Nilakantan, “Ballistic Impact of Dry Woven Fabric Composites: A Review, *Applied Mechanics Review*, vol. 61, pp. 1 – 13, 2008.
8. N. V. David, X. L. Gao, and J. Q. Zheng, “Ballistic Resistant Body Armor: Contemporary and Prospective Materials and Related Protection Mechanisms,” *Applied Mechanics Review*, vol. 62, pp. 1 – 20, 2009.
9. J. W. S. Hearle, P. Grosberg, and S. Backer, *Structural Mechanics of Fibers, Yarns and Fabrics*, John Wiley & Sons, Inc., New York, 1969.
10. W. D. Freeston, M. M. Platt, and M. M. Schoppee, “Mechanics of Elastic Performance of Textile Materials,” Part XVIII, “Stress-Strain Response of Fabrics Under Two-Dimensional Loading,” *Textile Research Journal*, vol. 37, pp. 948 – 975, 1967.
11. B. Parga-Landa and F. Hernandez-Olivares, “An Analytical Model to Predict Impact Behaviour of Soft Armours,” *International Journal of Impact Engineering*, vol. 16, pp. 455 – 466, 1995.
12. I. S. Chocron-Benloulou, J. Rodriguez, and V. Sanchez-Galvez, “A Simple Analytical Model to Simulate Textile Fabric Ballistic Impact Behavior,” *Textile Research Journal*, vol. 67, pp. 520 – 528, 1997.
13. B. Gu, “Analytical Modeling for the Ballistic Perforation of Planar Plain-Woven Fabric Target by Projectile,” *Composites: Part B Engineering*, vol. 34, pp. 361 – 371, June 2003.

14. P. M. Cuniff, "An Analysis of the System Effects in Woven Fabrics Under Ballistic Impact," *Textile Research Journal*, vol. 62, pp. 495 – 509, 1992.
15. D. Roylance, P. Chammas, J. Ting, H. Chi, and B. Scott, "Numerical Modeling of Fabric Impact," *Proceedings of the National Meeting of the American Society of Mechanical Engineers (ASME)*, San Francisco, CA, October 1995.
16. X. Zeng, V. B. C. Tan, and V. P. W. Shim, "Modeling Inter-Yarn Friction in Woven Fabric Armour," *International Journal for Numerical Methods in Engineering*, vol. 66, pp. 1309 – 1330, 2006.
17. C. T. Lim, V. P. W. Shim, and Y. H. Ng, "Finite-Element Modeling of the Ballistic Impact of a Fabric Armor," *International Journal of Impact Engineering*, vol. 28, pp. 13 – 31, 2003.
18. H. H. Billon and D. J. Robinson, "Models for the Ballistic Impact of Fabric Armor," *International Journal of Impact Engineering*, vol. 25, pp. 411 – 422, 2001.
19. F. Figucia, "Energy Absorption of Kevlar Fabrics Under Ballistic Impact," U.S. Army Natick Research and Development Command, 1980.
20. J. W. S. Hearle, C. M. Leech, C. Cork, and B. A. Adeyefa, "Ballistic Impact of Resistance of Multilayer Textile Fabrics," University of Manchester Institute of Science and Technology, October 1981.
21. C. T. Lim, V. B. C. Tan, and C. H. Cheong, "Perforation of High-Strength Double-Ply Fabric System by Varying Shaped Projectiles," *International Journal of Impact Engineering*, vol. 27, pp. 577 – 591, 2002.
22. J. Hedgepeth, "Stress Concentrations in Filamentary Structures," NASA TN D-882, National Aeronautics and Space Administration, Washington, DC, May 1961.
23. M. Karahan, "Comparison of Ballistic Performance and Energy Absorption Capabilities of Woven and Unidirectional Aramid Fabrics," *Textile Research Journal*, vol. 78, pp. 718 – 730, 2008.
24. Y. Duan, M. Keefe, T. A. Bogetti, B. A. Cheeseman, and B. Powers, "A Numerical Investigation of the Influence of Friction on Energy Absorption by a High-Strength Fabric Subjected to Ballistic Impact," *International Journal of Impact Engineering*, vol. 32, pp. 1299 – 1312, 2006.
25. D. A. Shockey, D. C. Erlich, and J. W. Simons, "Lightweight Fragment Barriers for Commercial Aircraft," *18th International Symposium on Ballistics*, San Antonio, TX, November 15 – 19, 1999.

26. Y. Duan, M. Keefe, T. A. Bogetti, and B. A. Cheeseman, "Modeling the Role of Friction During Ballistic Impact of a High-Strength Plain-Weave Fabric," *Journal of Composite Structures*, vol. 68, pp. 331 – 337, 2005.
27. Y. Duan, M. Keefe, T. A. Bogetti, B. A. Cheeseman, and B. Powers, "Modeling Friction Effects on the Ballistic Impact Behavior of a Single-Ply High-Strength Fabric," *International Journal of Impact Engineering*, vol. 31, pp. 996 – 1012, 2005.
28. V. B. C. Tan, V. P. W. Shim, and X. Zeng, "Modeling Crimp in Woven Fabrics Subjected to Ballistic Impact," *International Journal of Impact Engineering*, vol. 32, pp. 561 – 574, 2005.
29. X. Zeng, V. P. W. Shim, and V. B. C. Tan, "Influence of Boundary Conditions on the Ballistic Performance of High-Strength Fabric Targets," *International Journal of Impact Engineering*, vol. 32, pp. 631 – 642, 2005.
30. K. Joo and T. J. Kang, "Numerical Analysis of Energy Absorption Mechanism in Multi-Ply Fabric Impacts," *Textile Research Journal*, vol. 78, pp. 561 – 576, 2008.
31. J. Smith, J. Blandford, and H. Schiefer, "Stress-Strain Relationships in Yarns Subjected to Rapid Impact Loading: Part VI: Velocities of Strain Waves Resulting from Impact," *Textile Research Journal*, vol. 30, pp. 752 – 760, 1 October 1960.
32. W. Johnson, C. Collins, and F. Kindred, "A Mathematical Model for Predicting Residual Velocities of Fragments After Perforating Helmets and Body Armor," Technical Note 1705 Ballistic Research Laboratories, October 1968.
33. *ABAQUS/Explicit, Version 6.6*, ABAQUS Inc., Pawtucket, RI, 2007.
34. P. Cavallaro, A. Sadegh, and C. Quigley, "Decrimping of Plain Woven Fabrics Subjected to Coupled Biaxial Tension and Shear Stresses," *Textile Research Journal*, vol. 77, pp. 403 – 416, 2007.
35. M. Chitrangad, "Hybrid Ballistic Fabric," U.S. Patent No. 5,187,003, 16 February 1993.

APPENDIX A
YARN TENSIONS FOR NORMAL IMPACTS

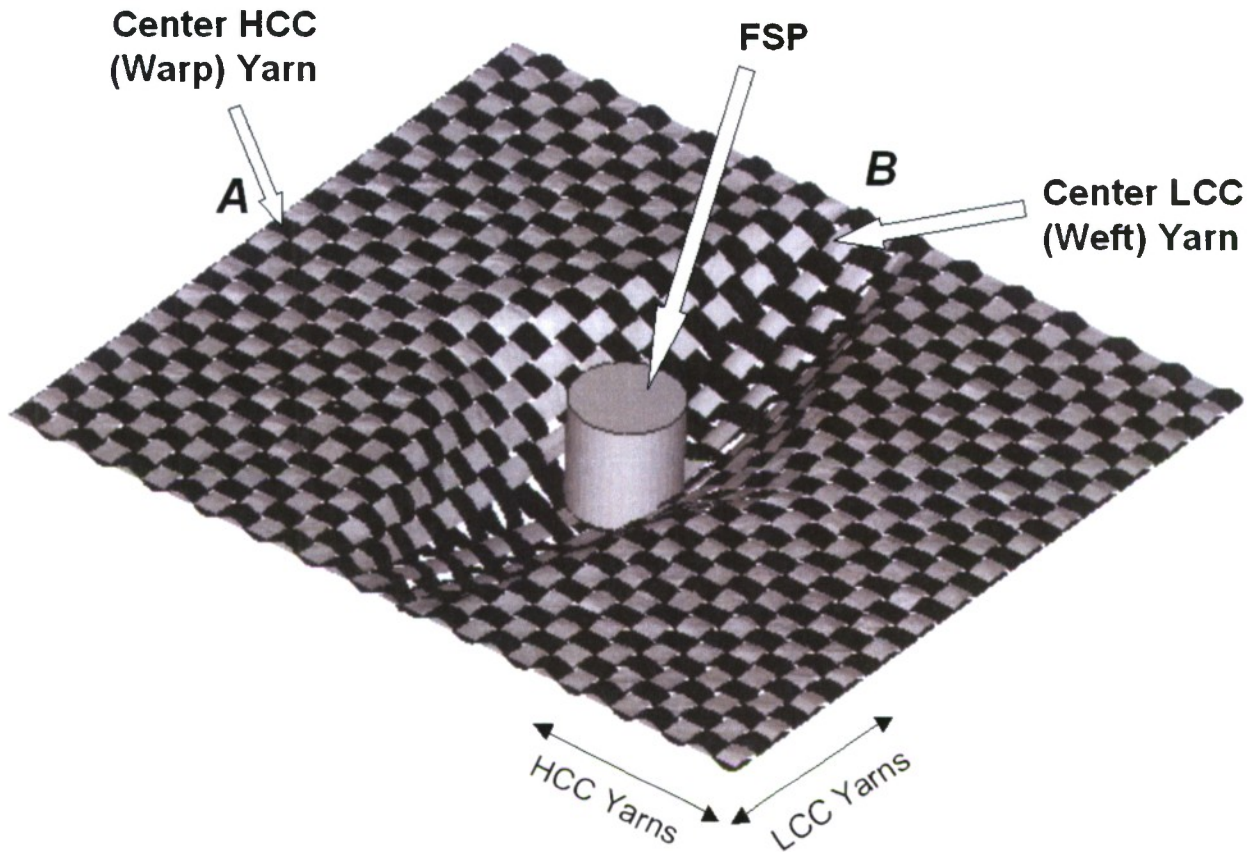
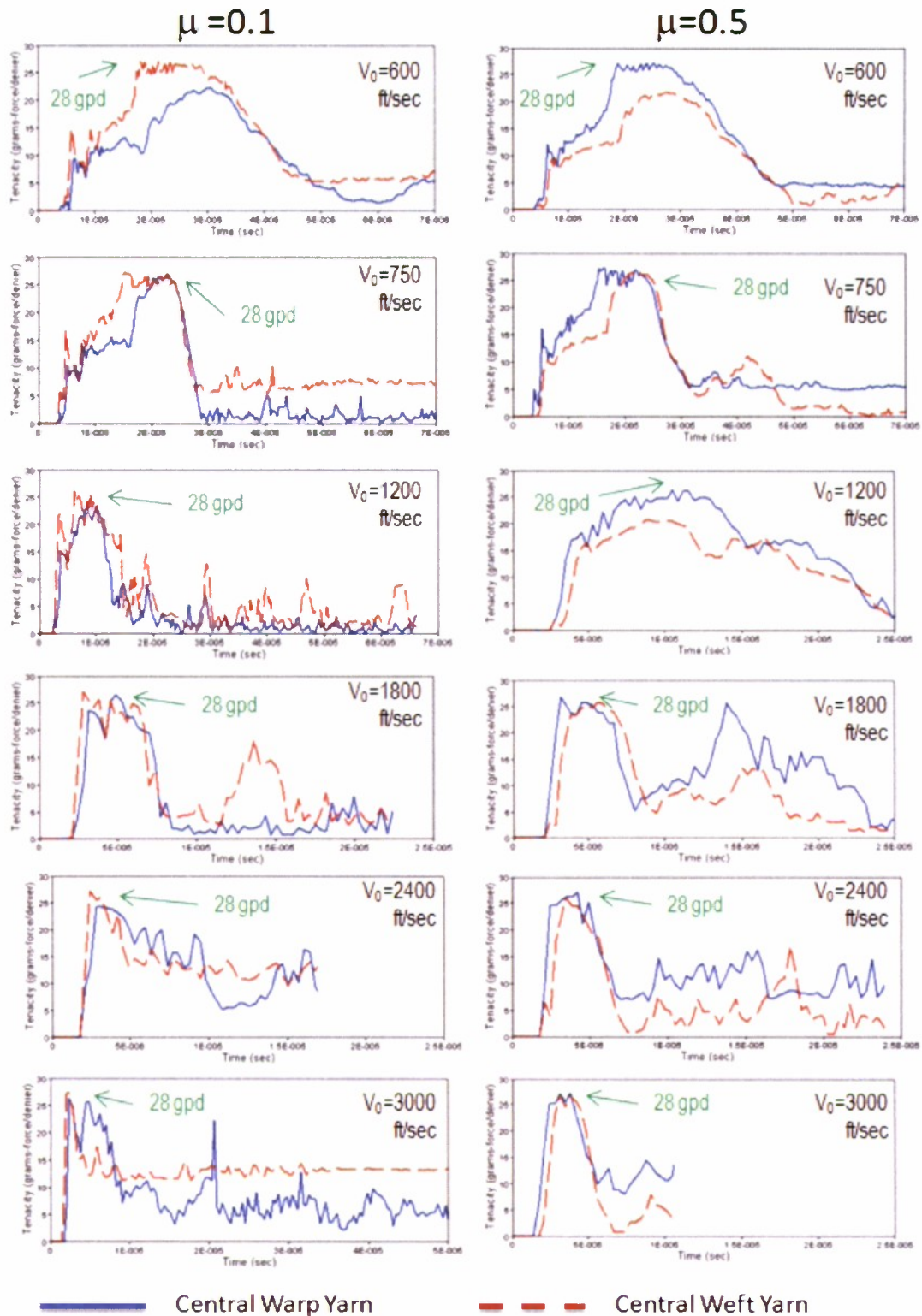
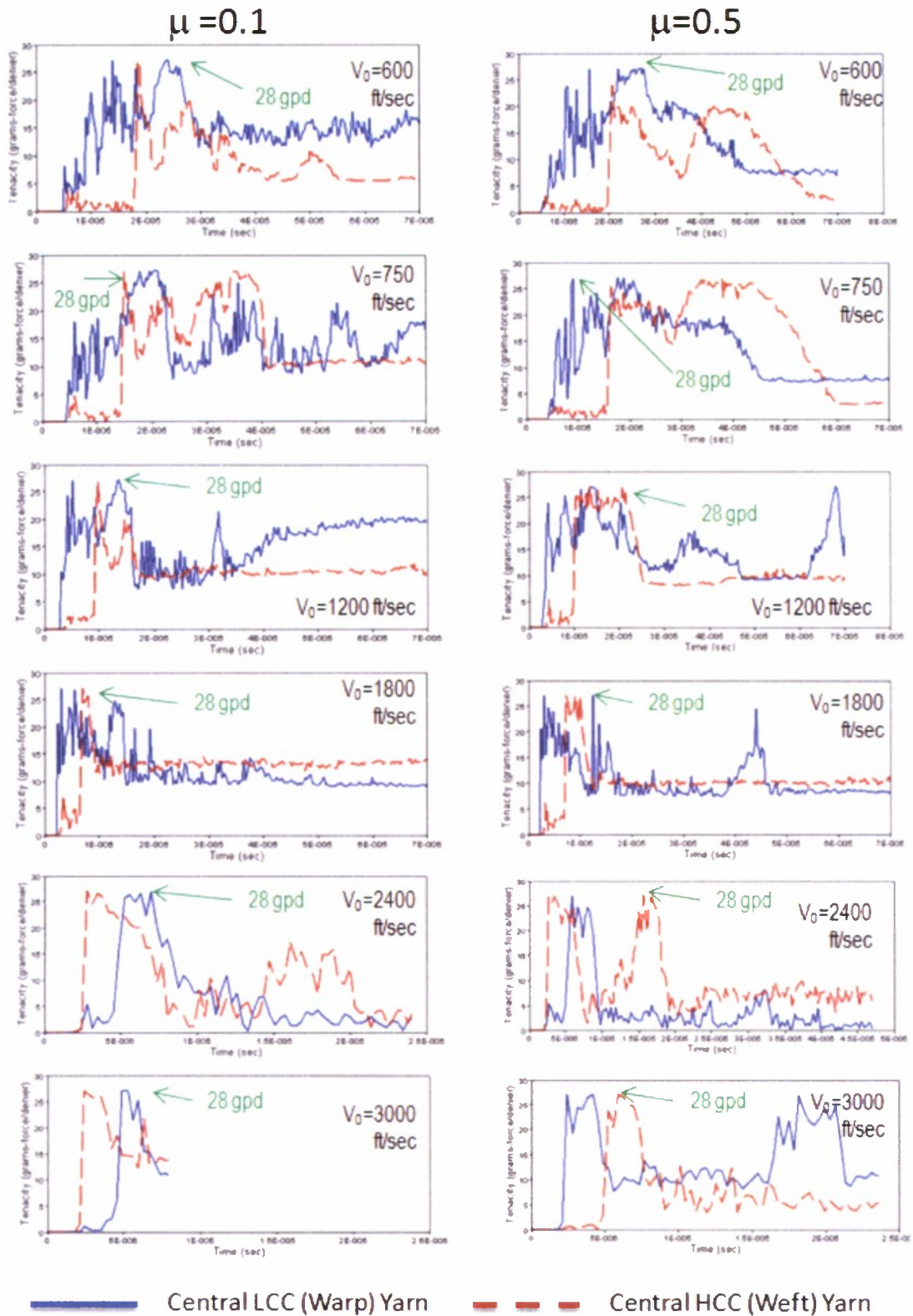


Figure A-1. Tension Monitoring Locations for the Central-Most HCC (Warp) and LCC (Weft) Yarns



**Figure A-2. Yarn Tension History Plots
for Normal Impacts: Iso-Crimp Case**



**Figure A-3. Yarn Tension History Plots
for Normal Impacts: Case C**

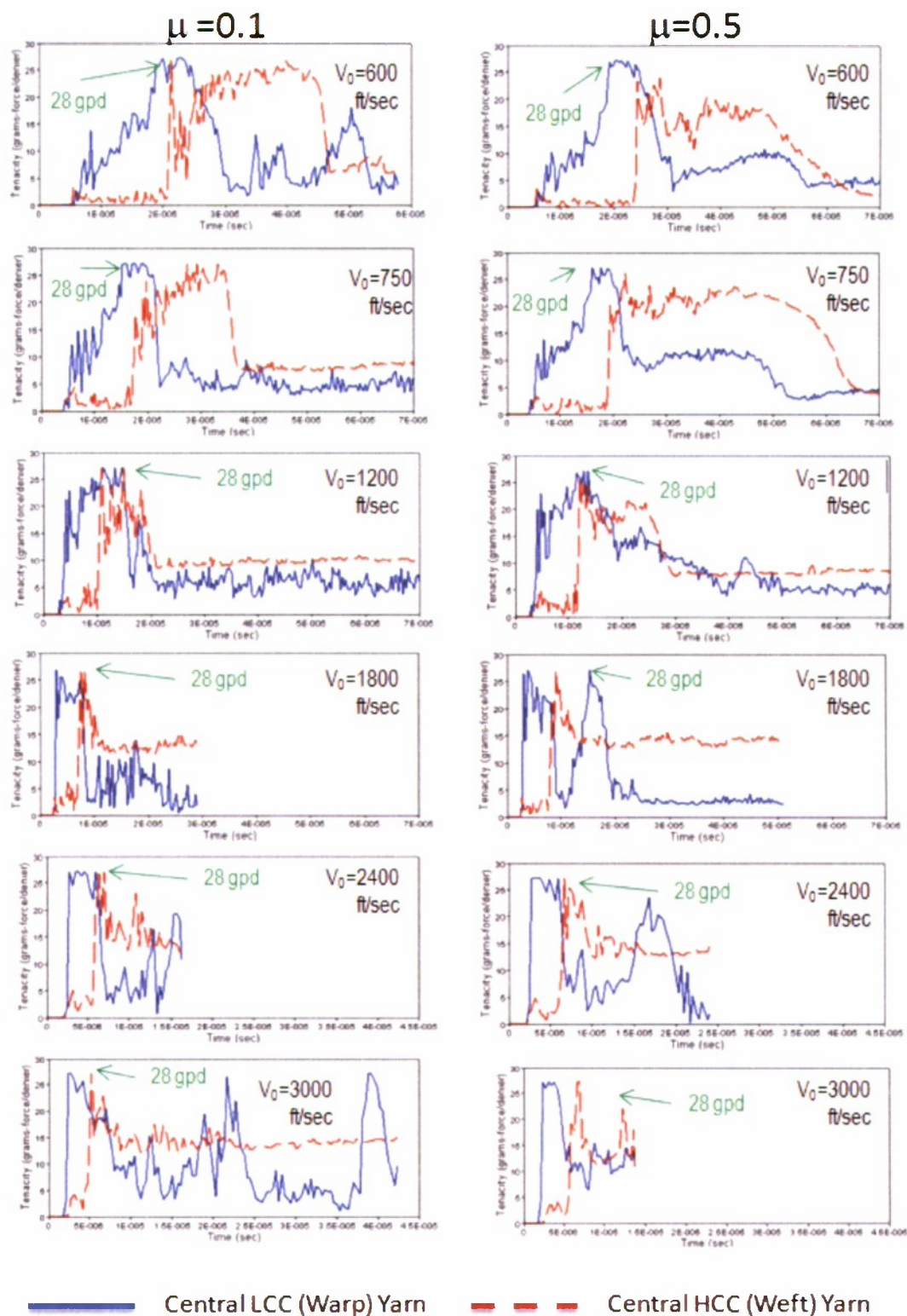


**Figure A-4. Yarn Tension History Plots
for Normal Impacts: Case B**



**Figure A-5. Yarn Tension History Plots
for Normal Impacts: Case A**

APPENDIX B
TIME-HISTORY PLOTS OF FSP AND FABRIC ENERGIES FOR NORMAL IMPACTS

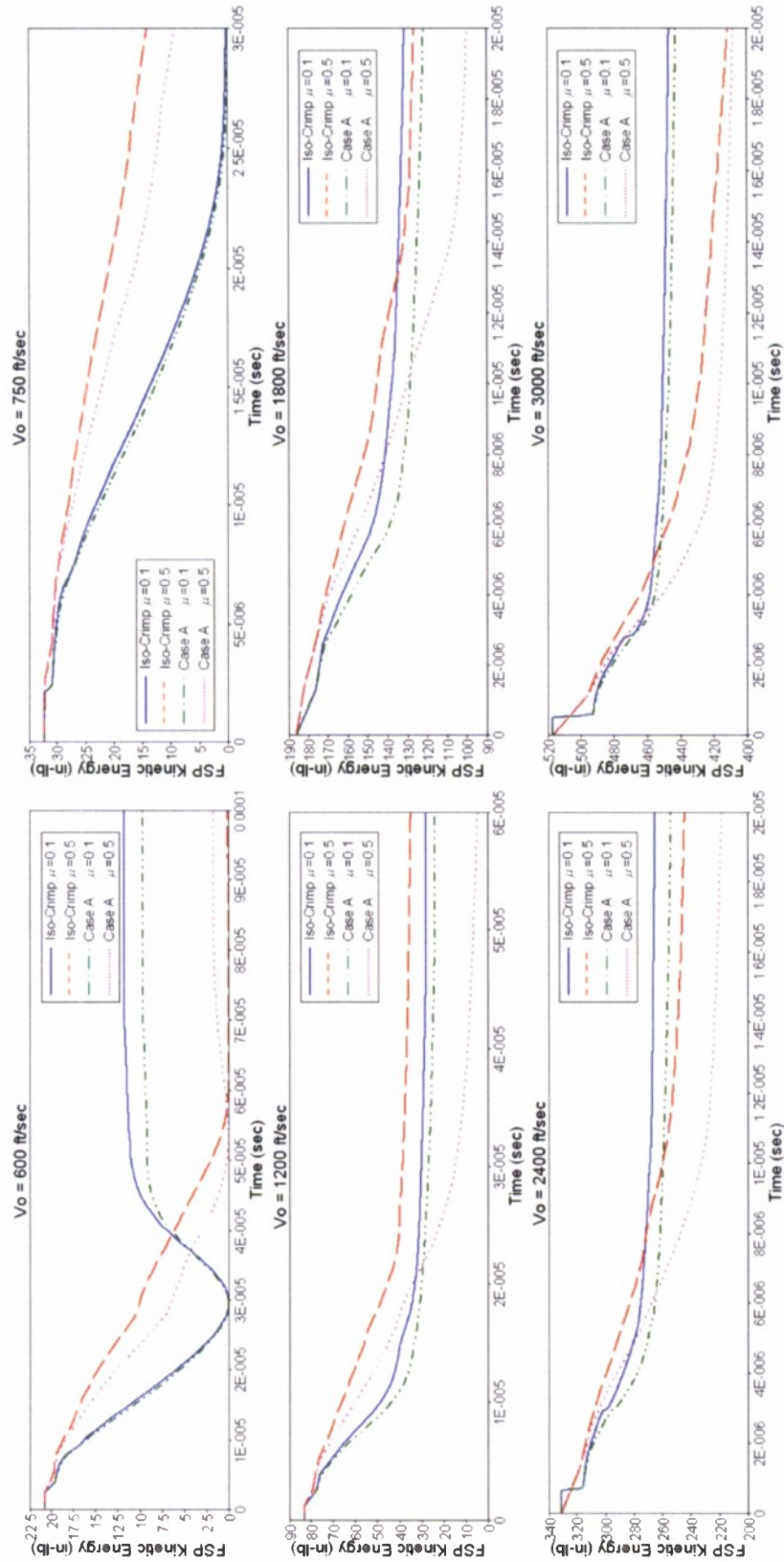


Figure B-1. Time-History Plots of FSP Kinetic Energies for Normal Impact

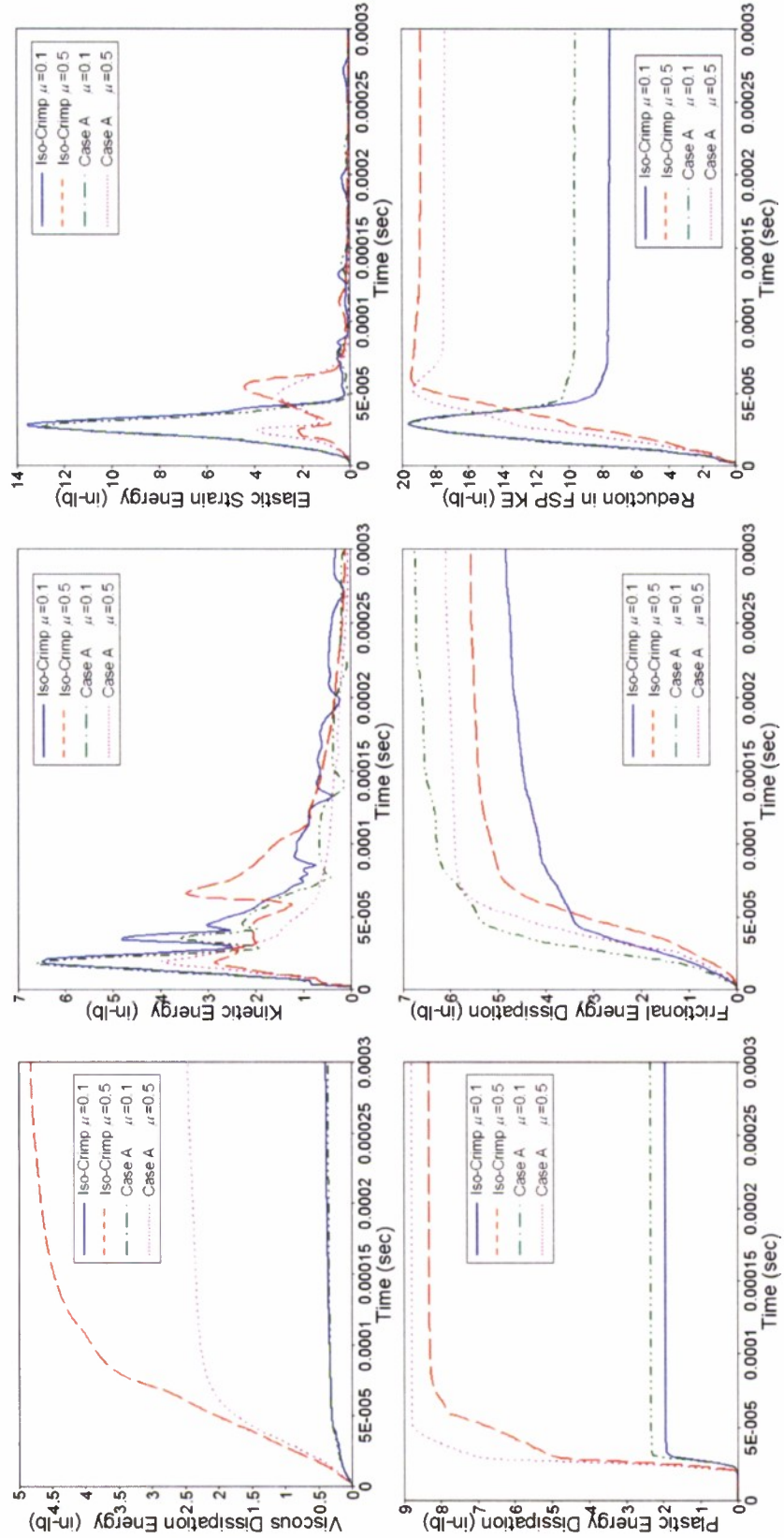


Figure B-2. Time-History Plots of Fabric Energies, Normal Impact with $V_0 = 600$ ft/sec

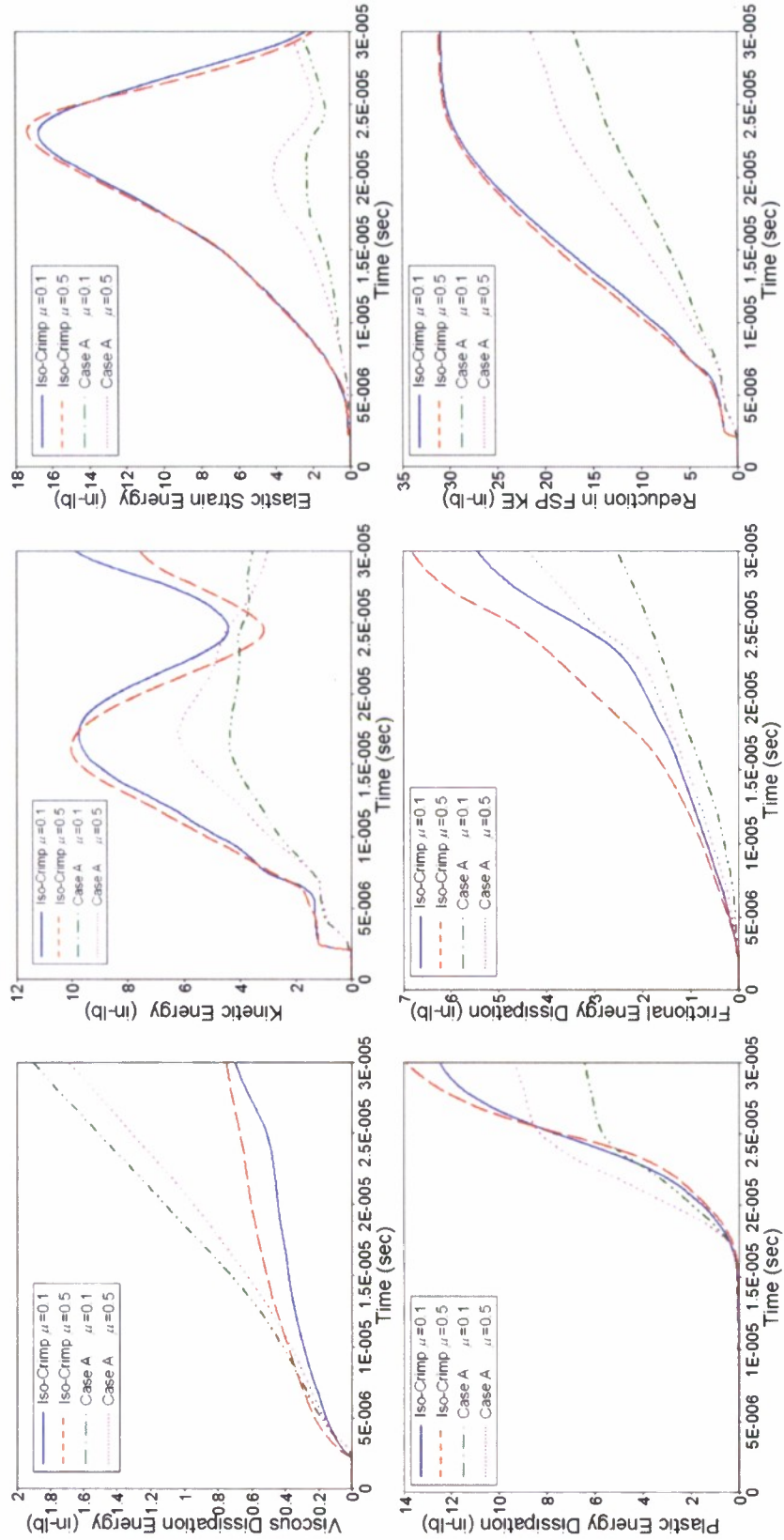


Figure B-3. Time-History Plots of Fabric Energies, Normal Impact with $V_0 = 750$ ft/sec

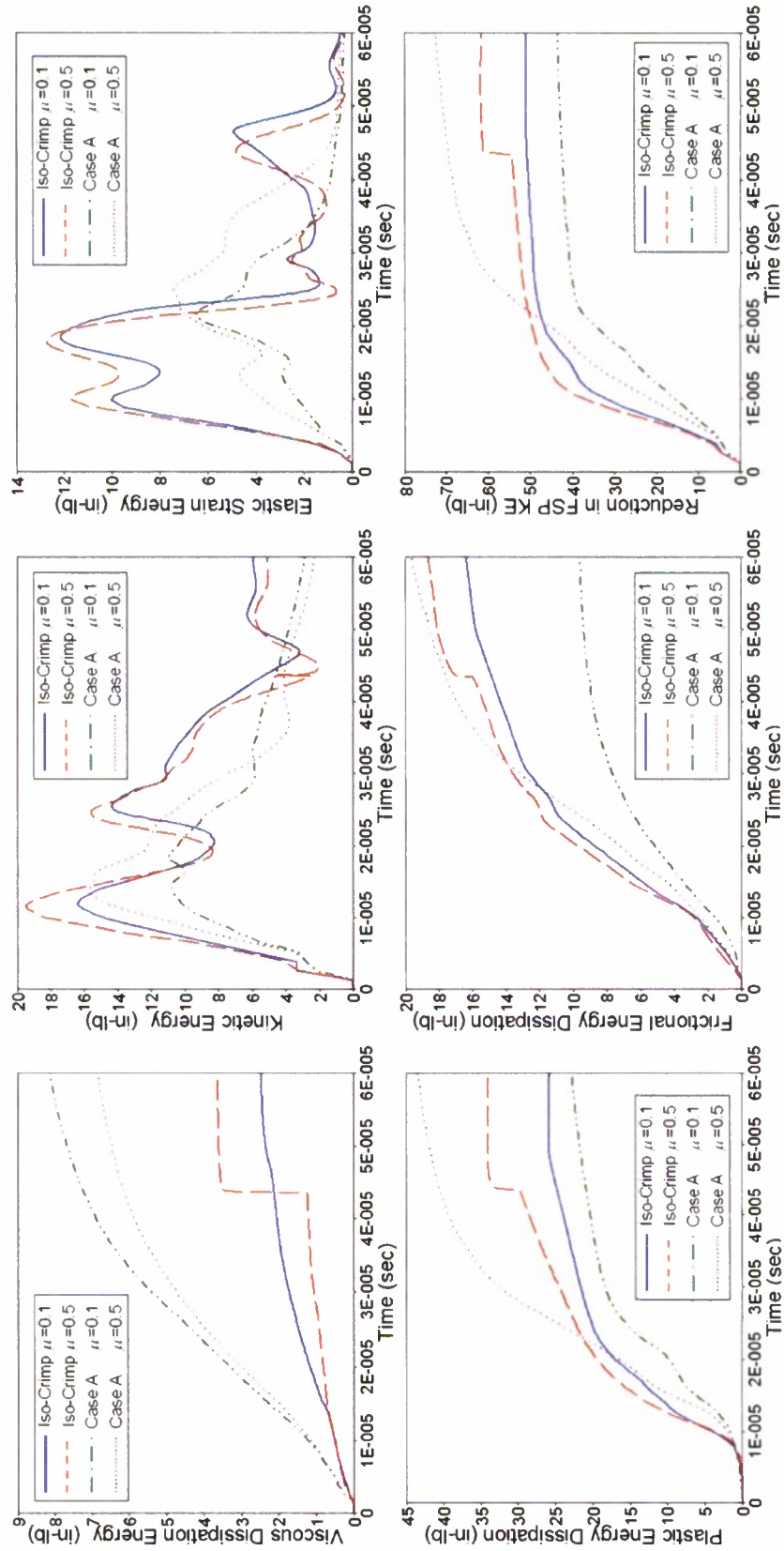


Figure B-4. Time-History Plots of Fabric Energies, Normal Impact with $V_0 = 1200$ ft/sec

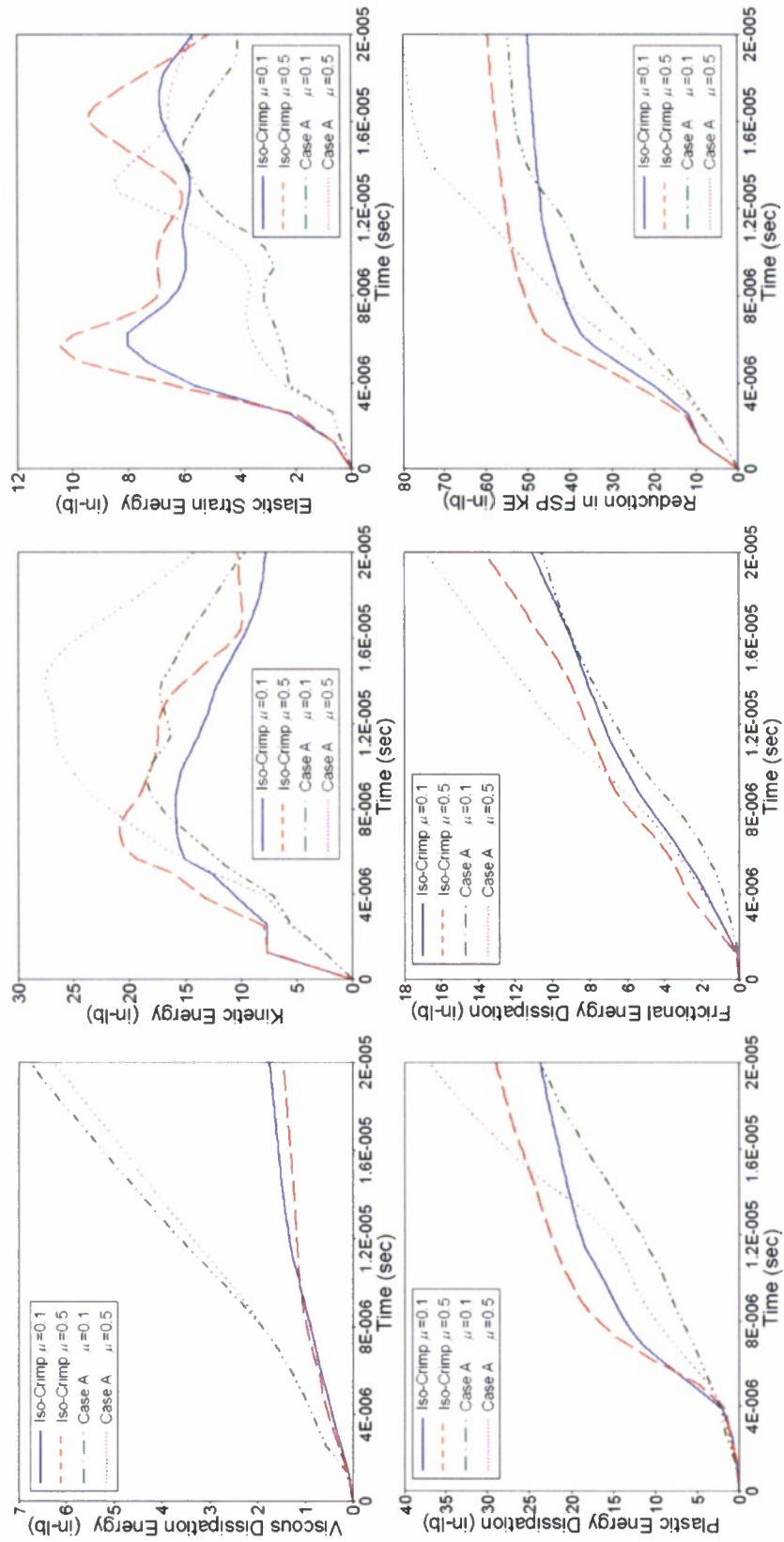


Figure B-5. Time-History Plots of Fabric Energies, Normal Impact with $V_0 = 1800$ ft/sec

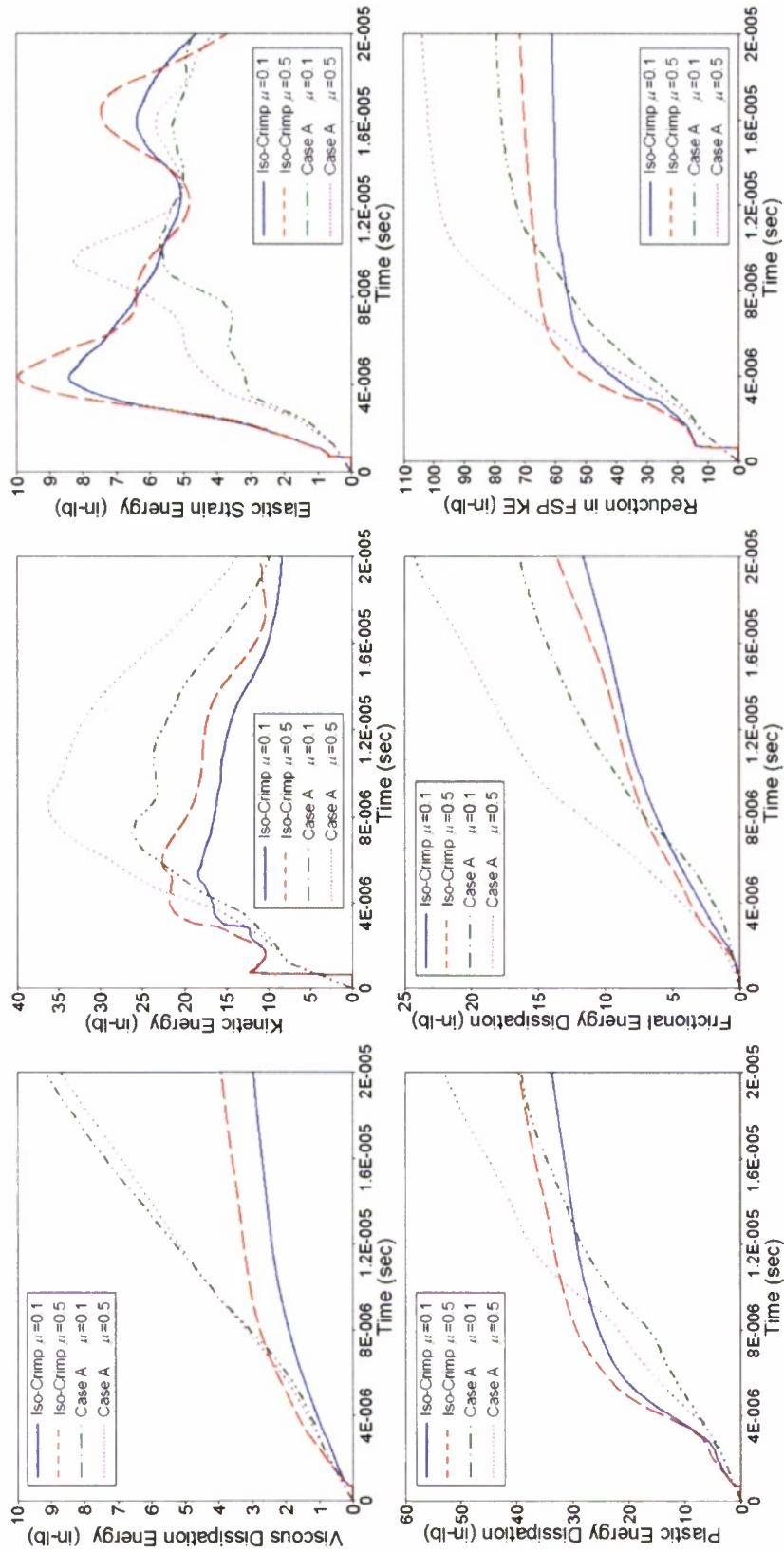


Figure B-6. Time-History Plots of Fabric Energies, Normal Impact with $V_0 = 2400$ ft/sec

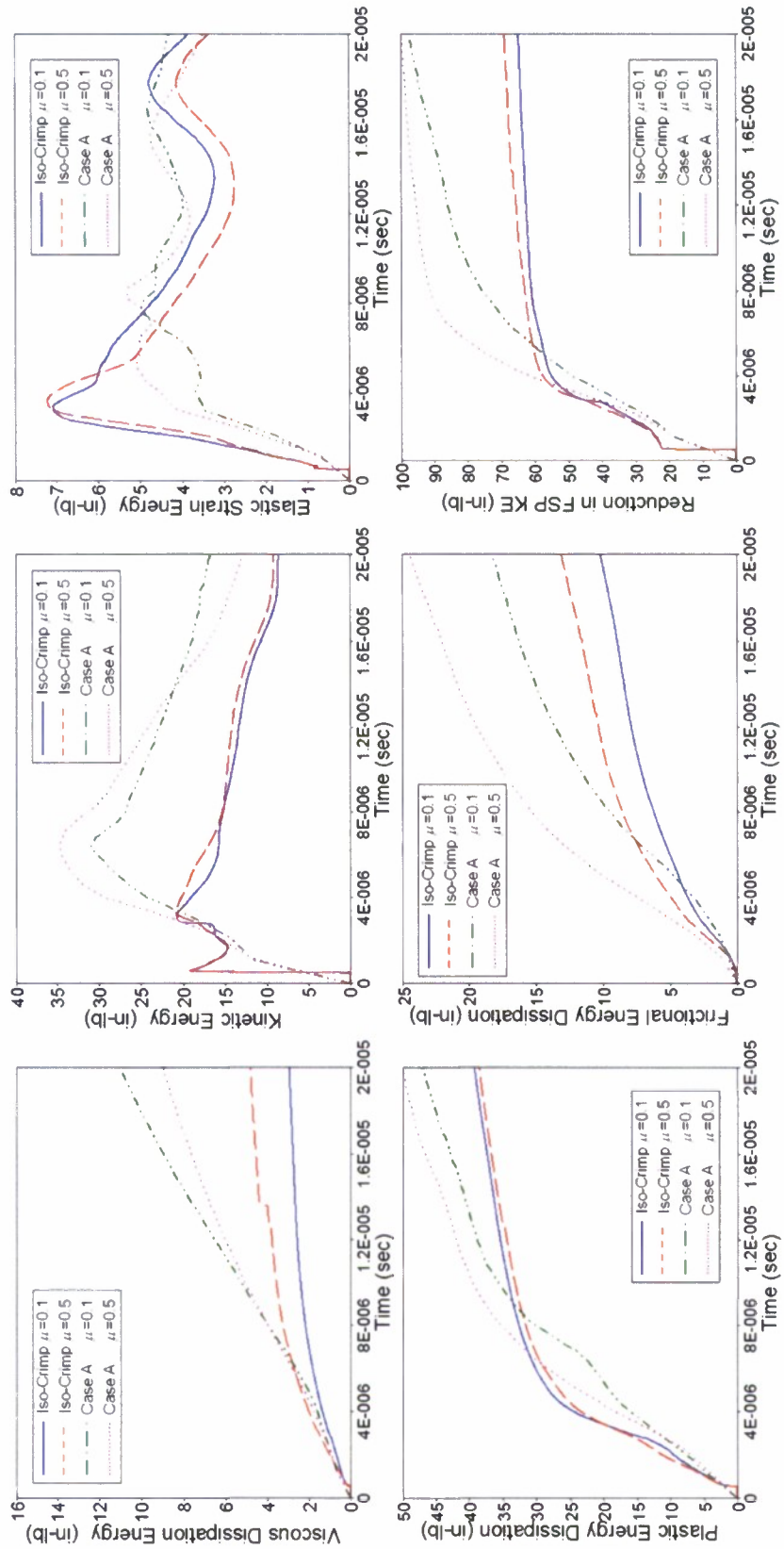


Figure B-7. Time-History Plots of Fabric Energies, Normal Impact with $V_0 = 3000$ ft/sec

APPENDIX C
YARN FAILURE PLOTS FOR OBLIQUE IMPACTS

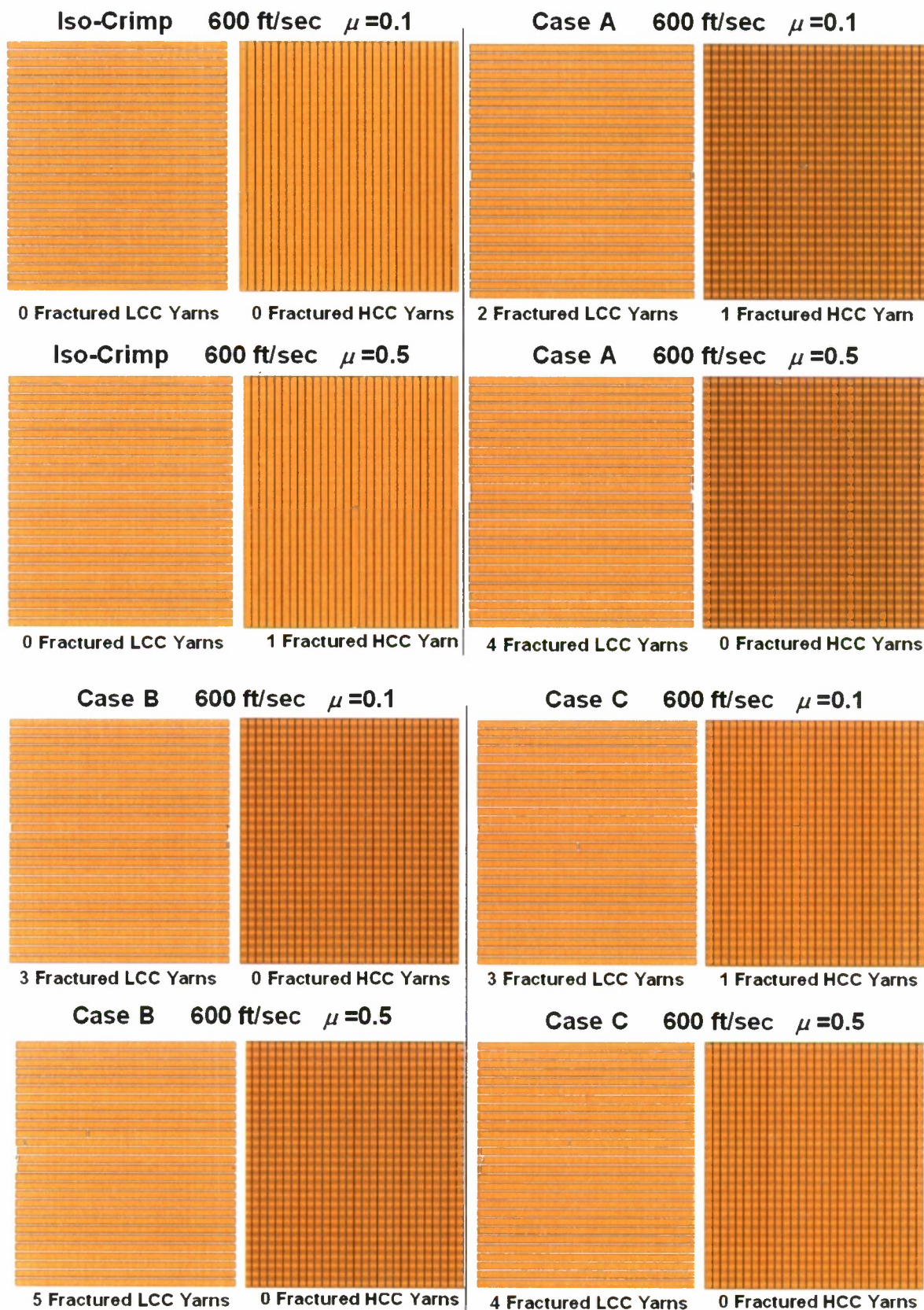


Figure C-1. Yarn Failure Plots for Oblique Impacts with $V_o = 600$ ft/sec

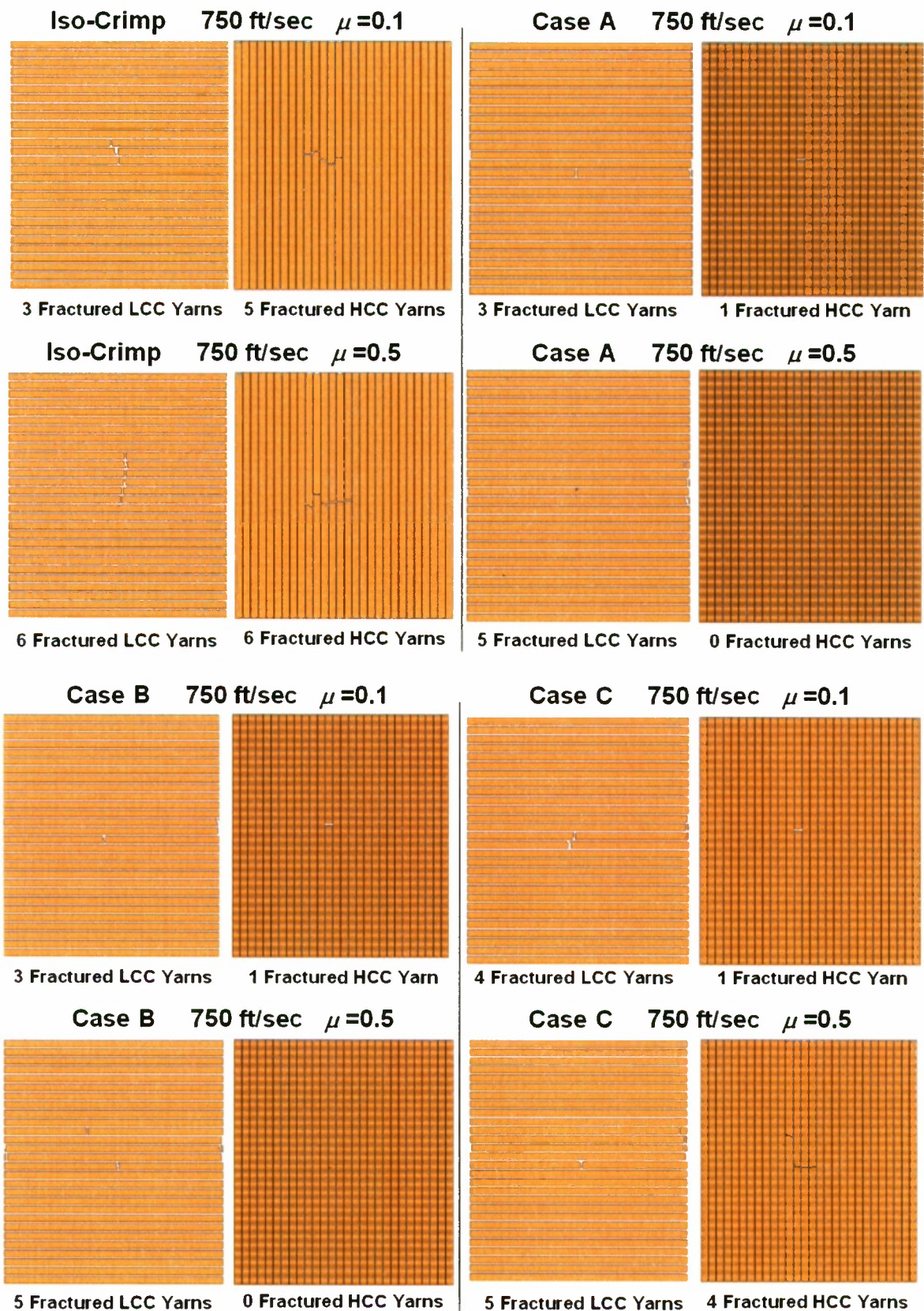


Figure C-2. Yarn Failure Plots for Oblique Impacts with $V_o = 750$ ft/sec

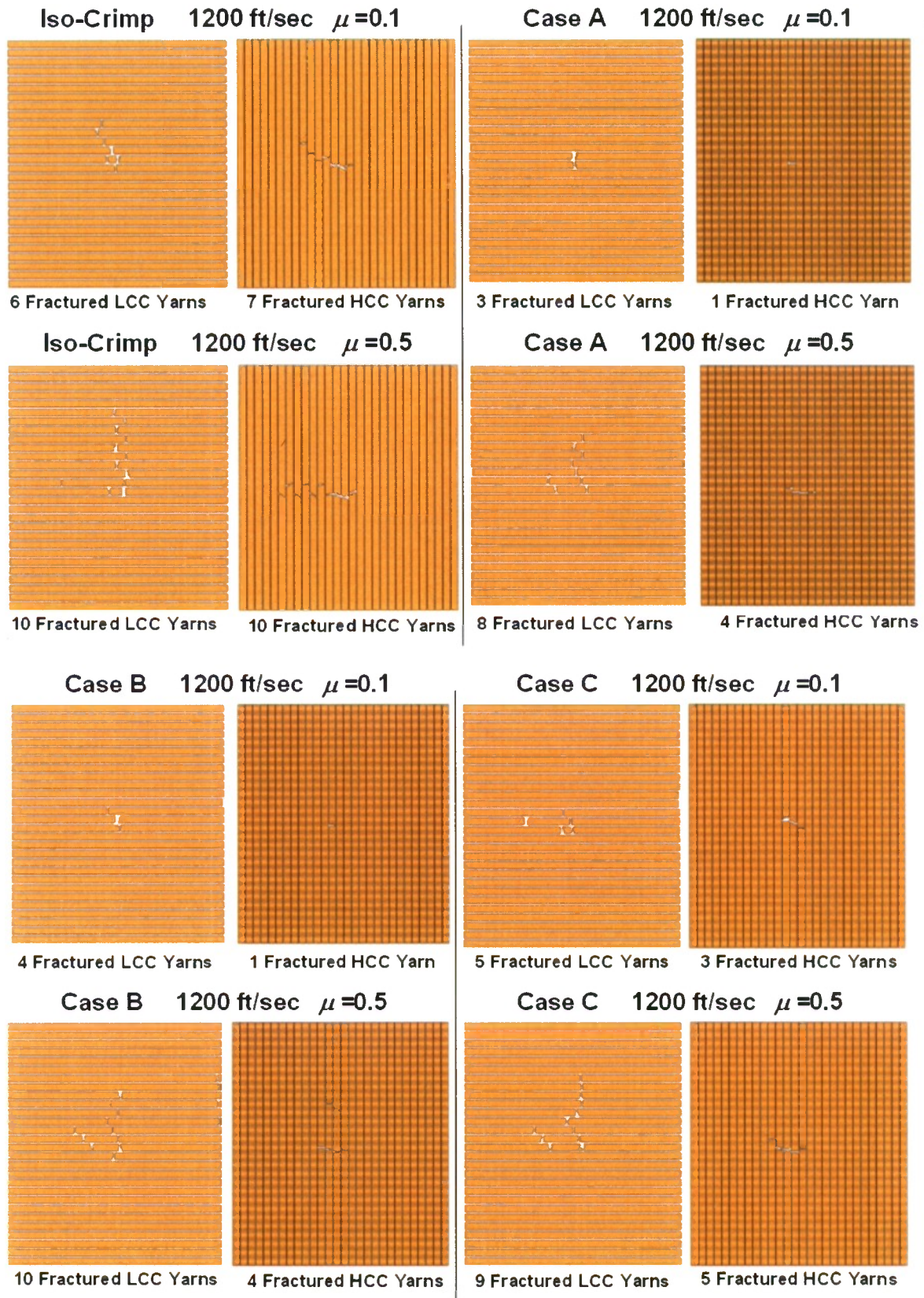


Figure C-3. Yarn Failure Plots for Oblique Impacts with $V_o = 1200$ ft/sec

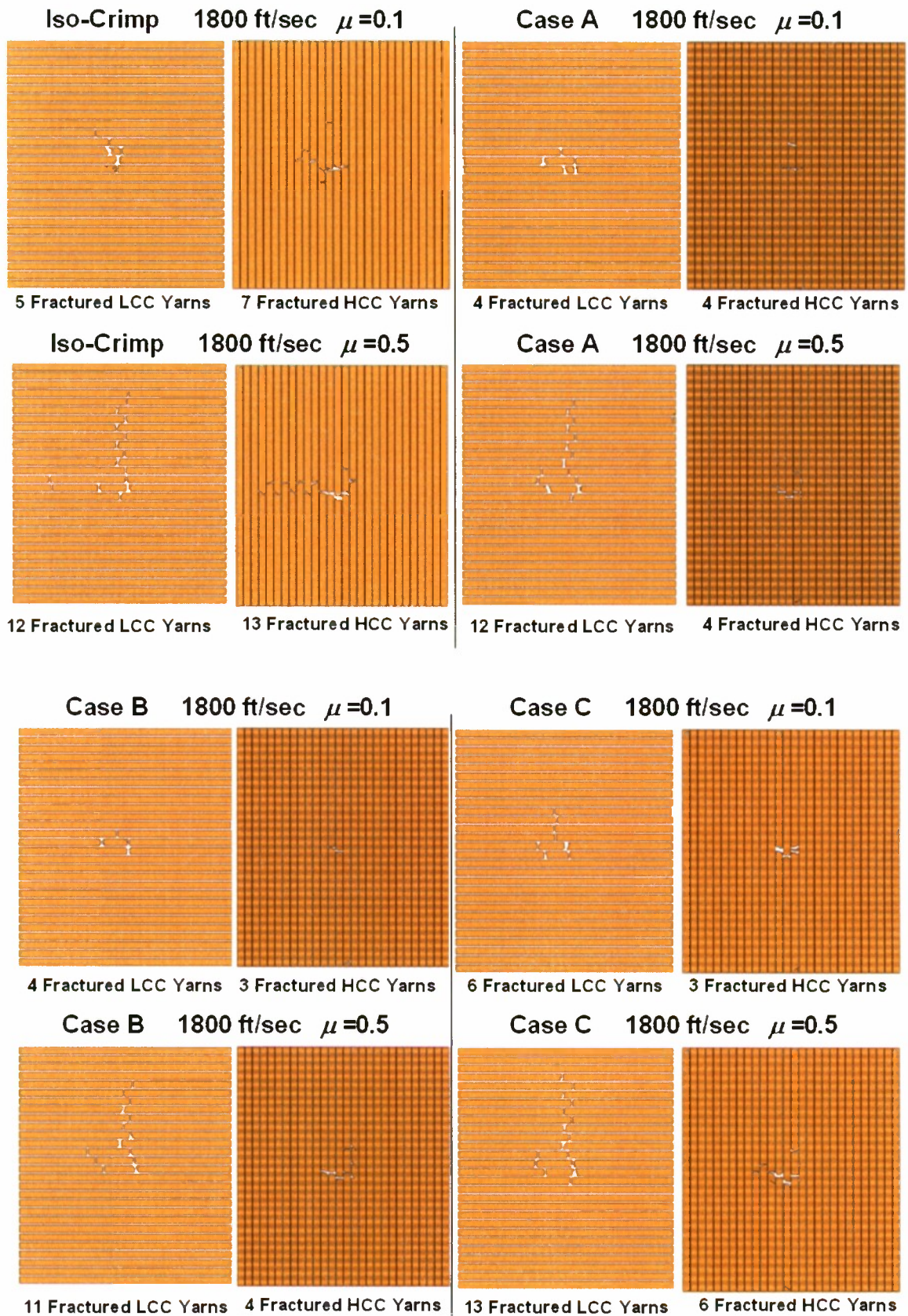


Figure C-4. Yarn Failure Plots for Oblique Impacts with $V_o = 1800$ ft/sec

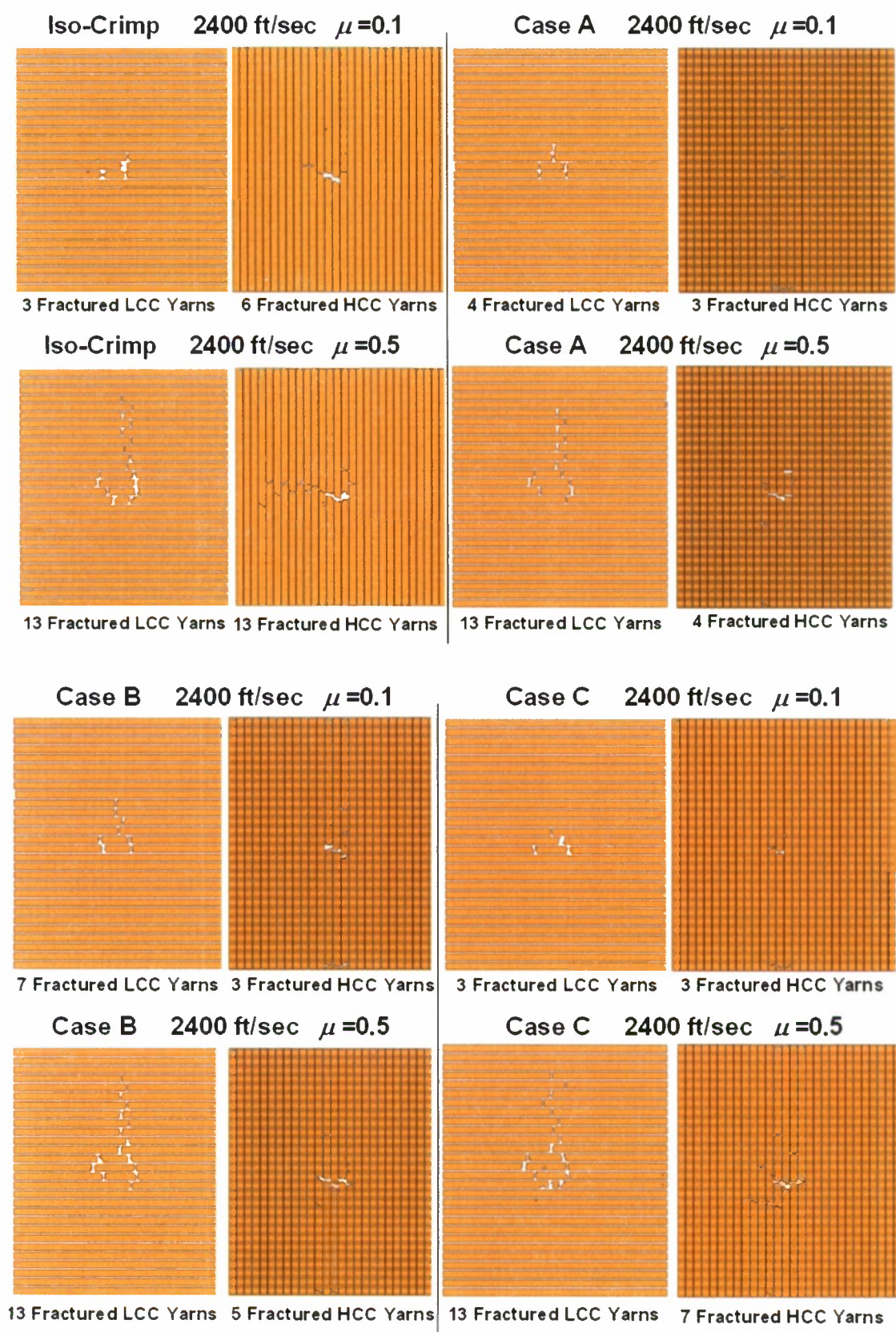


Figure C-5. Yarn Failure Plots for Oblique Impacts with $V_o = 2400$ ft/sec

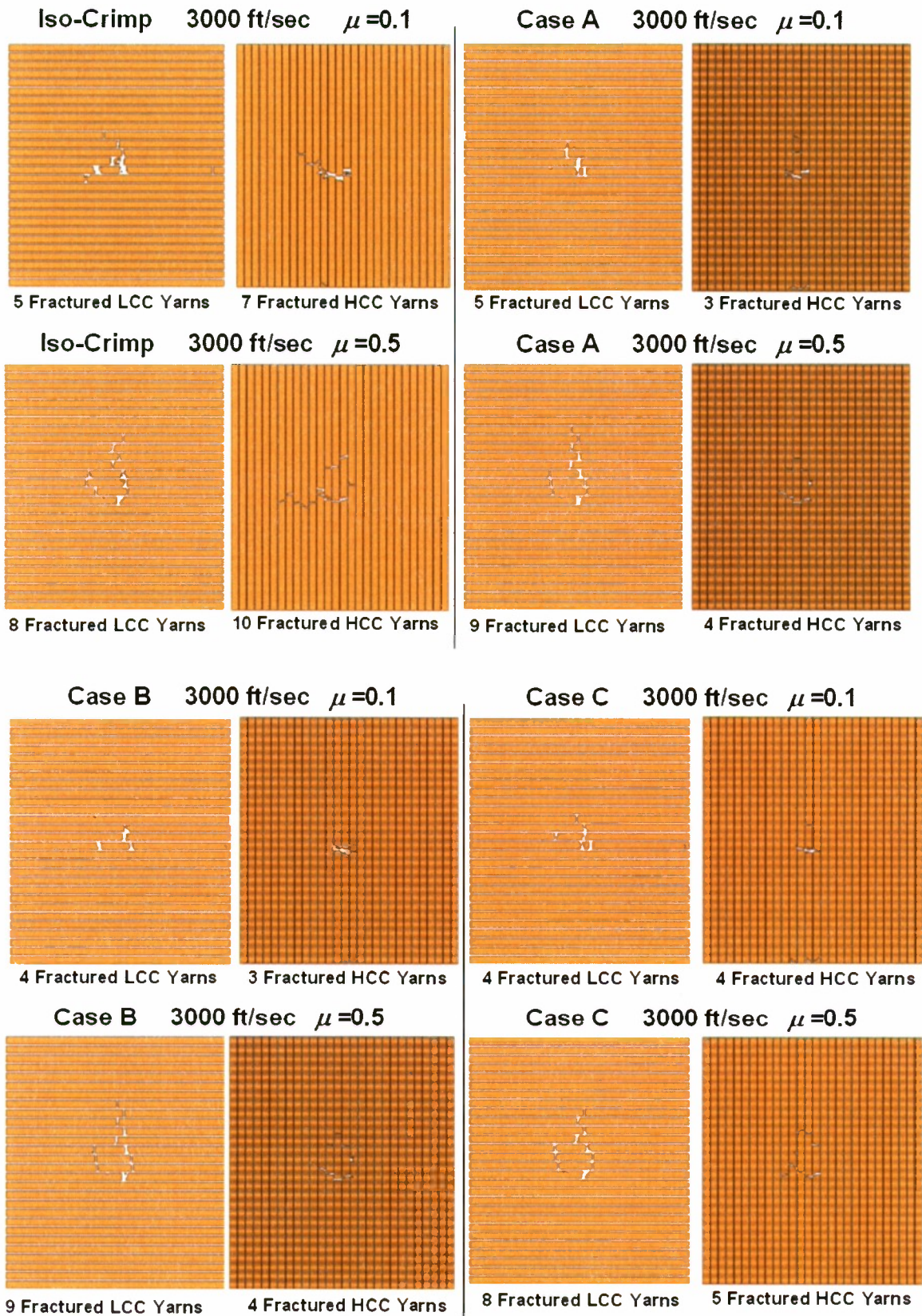


Figure C-6. Yarn Failure Plots for Oblique Impacts with $V_o = 3000$ ft/sec

APPENDIX D
TIME-HISTORY PLOTS OF FSP AND FABRIC ENERGIES FOR OBLIQUE IMPACTS

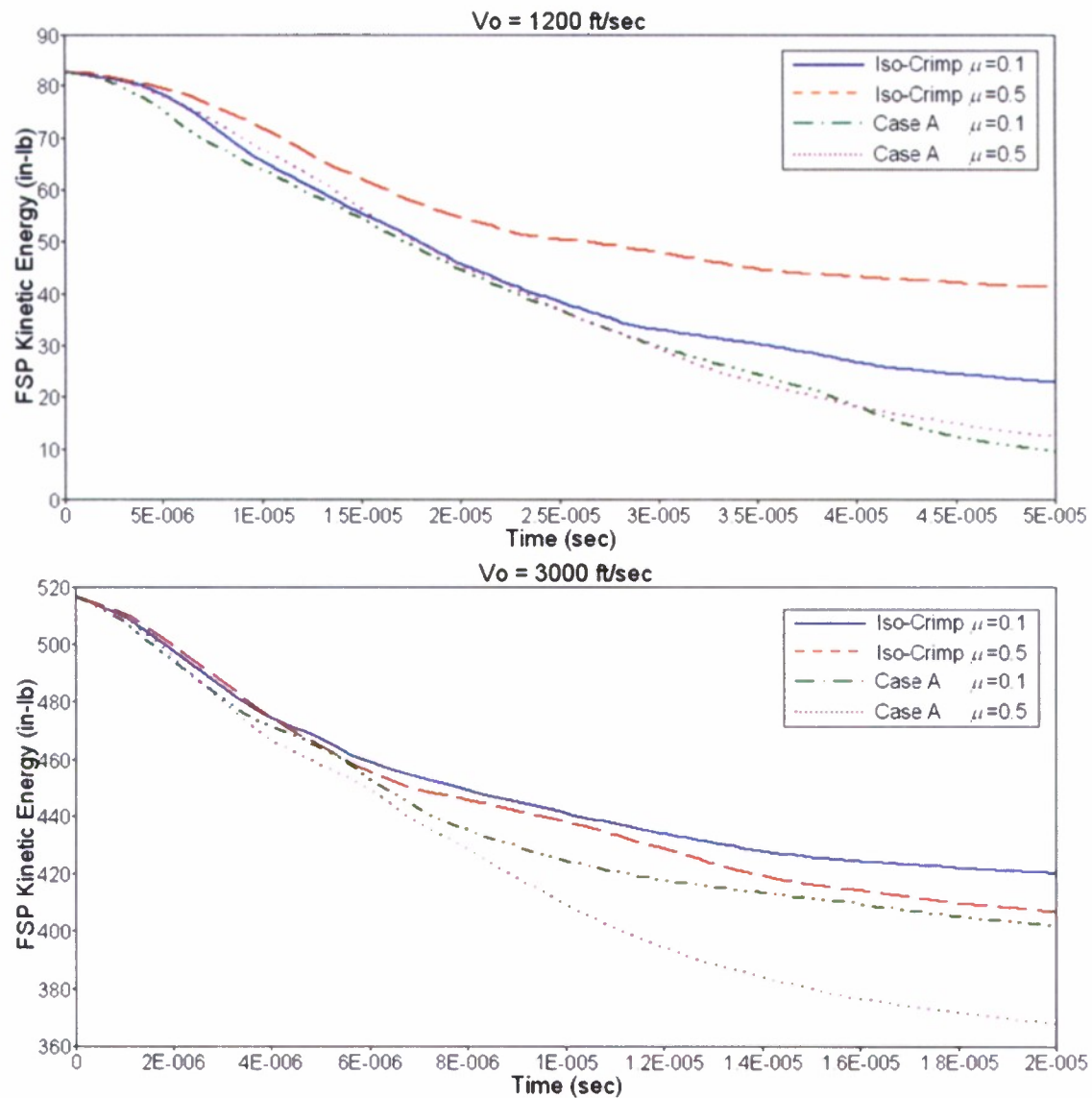


Figure D-1. Time-History Plots of FSP Kinetic Energies for Oblique Impacts

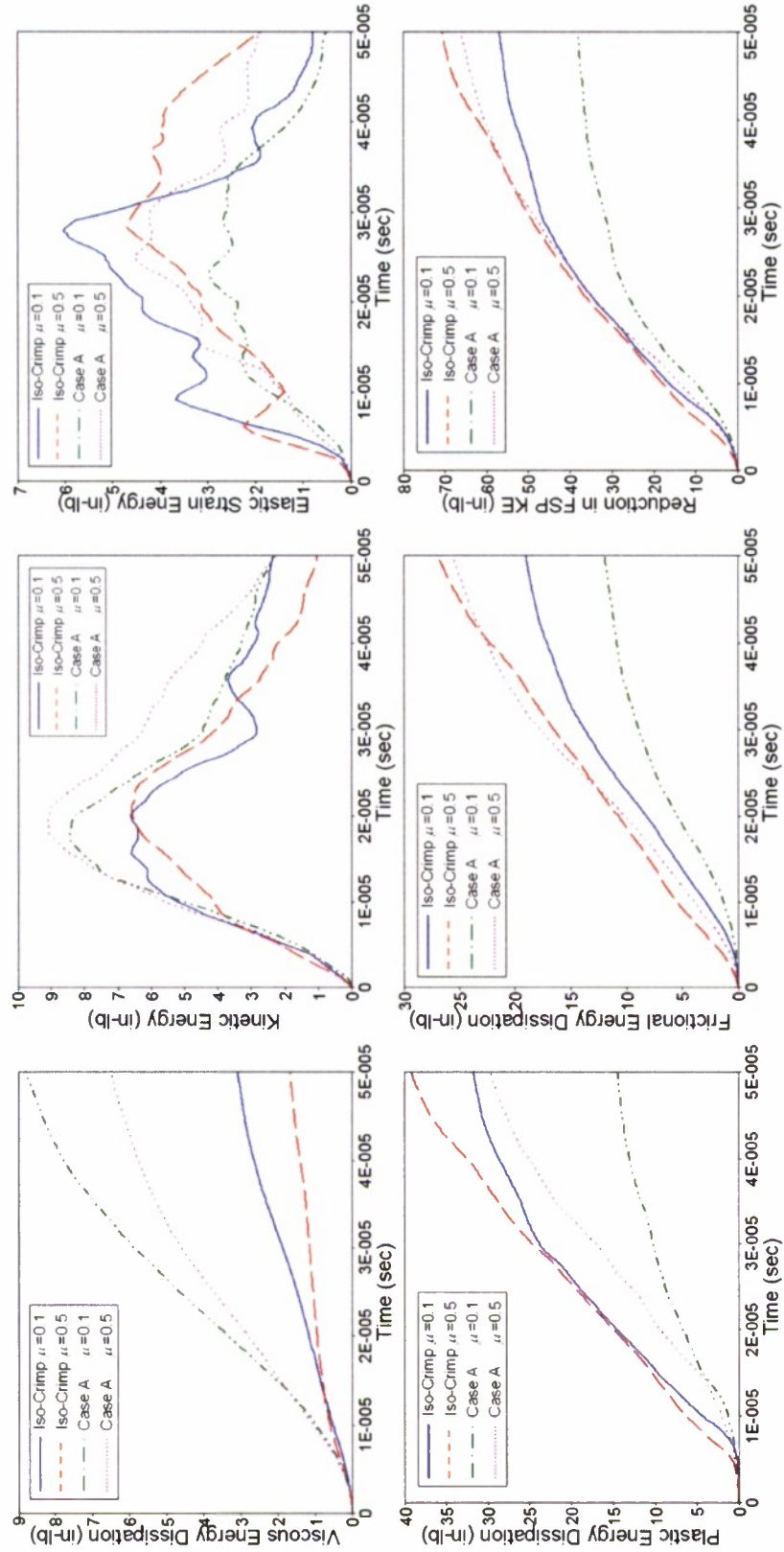


Figure D-2. Time-History Plots of Fabric Energies, Oblique Impact with $V_o = 1200$ ft/sec

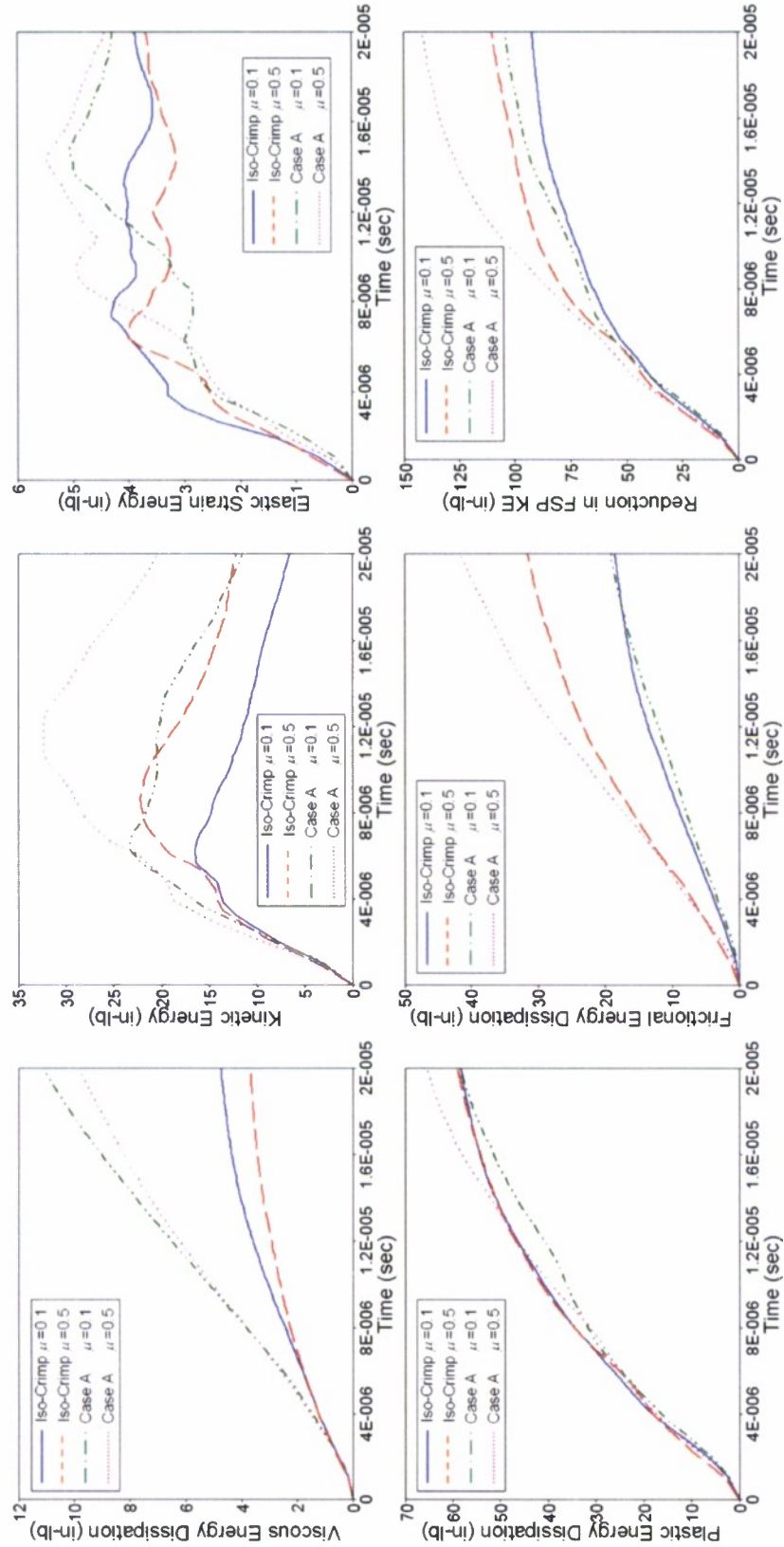


Figure D-3. Time-History Plots of Fabric Energies, Oblique Impact with $V_o = 3000$ ft/sec

INITIAL DISTRIBUTION LIST

Addressee	No. of Copies
U.S. Army Research Laboratory, Aberdeen Proving Ground, MD (AMSRD-ARL-WM-MD (B. Cheeseman (5), R. Dooley, C. Yan, B. Scott, D. Granville), RDRL-WMM-D (V. Champagne, Jr.), RDRL-WMP-F (A. Frydman), RDRL-WMM-A (M. Maher))	12
U.S. Army Aberdeen Test Center, Aberdeen Proving Ground, MD (TEDT-AT-WFT (F. Carlen))	1
U.S. Army Natick Soldier Research, Development, and Engineering Center, Natick, MA (M. Jee, F. Kostka, J. Hampel, C. Quigley, K. Horak, P. Cunniff, J. Ward, J. Mackiewicz, D. Lee, T. Godfrey, J. Milette, R. Benny, G. Thibault)	13
U.S. Army Research Office (RDRL-RO-EN (B. LaMattina, D. Stepp, W. Mullins))	3
Navy Clothing and Textile Research Facility, Natick, MA (B. Avellini, L. Caulfield, T. Hart, C. Heath)	4
Naval Surface Warfare Center, Panama City, FL (Code CX05 (F. Garcia))	1
Naval Surface Warfare Center, Carderock Division, W. Bethesda, MD (Code 65 (R. Crane, E. Rasmussen))	2
Naval Surface Warfare Center, Dahlgren Division, Dahlgren, VA (Code G25 (W. Mock))	1
Office of Naval Research (ONR-DOI (L. Schuette), ONR-331 (R. Barsoum), ONR-334 (Y. Rajapakse))	3
Weapons and Protective Systems COE, Applied Research Laboratory/ Pennsylvania State University	1
Savannah River Site (J. Wong, C. Robinson)	2
Warwick Mills, New Ipswich, NH (C. Howland)	5
Defense Technical Information Center	2
Center for Naval Analyses	1